Surface Gated Quantum Dots in Shallow GaAs-AlGaAs Heterostructures

by Zoltán Borsosföldi

Thesis submitted to the University of Glasgow's Department of Physics and Astronomy for the degree of Doctor of Philosophy, April 1998

To my family, friends and Artúr

Acknowledgements

I would like to thank first of all my supervisor Dr. Andrew Long who made it possible for me to carry out this research, for all his help with the experiments, analysing the measurement data and making the numerous corrections in this thesis. I also would like to thank John Davies and Ivan Larkin for their theoretical work and advice during my research. Thanks to Steve Beaumont for providing the stimulating research environment and to Elef Skuras for introducing me to the secrets of shallow heterostructures and for being my cheerful lunch companion. I am also very grateful to the members of the MBE group who grew all the material on which our devices were made. Special thanks to the fabrication support team Steve Thoms, Douglas McIntyre and Helen McLelland, Susan Ferguson, David Gourlay whose help nowadays is even more valued and appreciated. Very special thanks should go to all my friends for providing an excellent company and brilliant entertainment. Thanks to Roberto for all the good advice and food and Pasquale for his spirit and dance classes.

Contents

Chapter 1 Introduction **1**

1.1 Surface Gated Quantum Dots 1
1.2 Aim of Work 2
1.3 Chapter Summary 2

Chapter 2 Theory of Electron Transport in Heterostructures **5**

2.1 Introduction 5
2.2 GaAs-AlGaAs Heterostuctures 5
2.3 Modulation Doped GaAs -AlGaAs Heterostructure 6
2.4 Two Dimensional Electron Gas (2DEG) 9
2.5 Surface Gated GaAs-AlGaAs Heterostructure 11
2.6 Electron Transport in a Two Dimensional Electron Gas 13
2.6.1 Diffusive Transport Regime 14
2.6.2 Quasi-ballistic regime 14
2.6.3 Ballistic Regime 15
2.7 Adiabatic Electron Transport 16
2.7.1 Quantum Point Contacts 16
2.8 Electron Transport in a Magnetic Field 19
2.8.1 Two Dimensional Electron Gas in a Magnetic Field 19
2.8.2 Electron Transport in Narrow Channels in a Magnetic Field 24
2.8.3 Transmission of Edge Channels by QPCs 26
2.8.4 Electron transport in Series QPCs in a Magnetic Field 28
References 31

Chapter 3 Device Fabrication **33**

3.1 Introduction 33
3.2 Principles of Optical Lithography 35
3.2.1 Process of Optical Lithography 35
3.2.1.1 Sample Cleaning 37
3.2.1.2 Photoresist Coating 37
3.2.1.3 Exposure of the Photoresist 38
3.2.1.4 Resist Development 38
3.2.1.5 Metallisation and Lift-off 38
3.2.1.6 Wet Etch 39
3.2.2 Electron Beam Lithography 39
3.3 Sample fabrication 40
3.3.1 Deoxidisation and Ohmic Contacts 41
3.3.2 Isolation 42
3.3.3 Fabrication of Nanostructures 43
3.3.4 Wiring Level 44
3.3.5 Sample Inspection 46
3.3.6 Sample Bonding 47
3.4 Electron Beam Lithography 47
3.4.1 Electron Beam Writing 48
3.4.1.1 Proximity Effect 48
3.4.1.2 Exposure Test 48
3.4.1.3 Registration 49
References 50

Chapter 4 Experimental Techniques **51**

4.1 Introduction 51
4.2 Cryogenic Equipment 51
4.2.1 Dilution Refrigerator Insert 52
4.2.2 Variable Temperature Insert 52
4.3 Sample Handling and Mounting 54

4.4 AC Lock-in Measurement Technique 56
References 61

Chapter 5 Charging Effects in Quantum Dots 62

5.1 Introduction 62
5.1.1 Theory of Single Electron Charging Effects 63
5.2 Optimisation of Quantum Dots 69
5.2.1 Pinned Surface Approximation 70
5.2.2 Frozen Surface Approximation 72
5.3 Depletion Length in Surface Gated Quantum Dots 74
5.4 Measurements 78
5.4.1 350 nm Quantum Dot Z19A 78
5.4.2 250 nm Quantum Dot Z20A 79
5.4.3 150 nm Quantum Dot Z2B 81
5.4.4 150 nm Quantum Dot Z212B 81
5.4.5 120 nm Quantum Dot Series Z27 82
5.4.6 Double Gated 200 nm Quantum Dots 84
5.5 Electrostatic Potential and Number of Electrons in Surface Gated Quantum Dots 85
5.6 Discussion 86
5.7 Conclusions 88
References 90

Chapter 6 Temperature Dependence Measurements in Quantum Dots 92

6.1 Introduction 92
6.2 Theory of Temperature Dependence 93
6.2.1 Line Shape of Coulomb Blockade Oscillations at and above 1.2 K 95
6.3 Measurements 96
6.3.1 350 nm Quantum Dot Z19A 98

6.3.2 250 nm Quantum Dot Z20A 98
6.3.3 150 nm Quantum Dot Z2B 100
6.3.4 150 nm Quantum Dot Z212B 102
6.3.5 120 nm Quantum Dot Z27B 105
6.4 Conclusions 105
References 111

Chapter 7 DC Source-Drain Bias Measurements 113

7.1 Introduction 113
7.2 Theory of The Coulomb Blockade Theory 114
7.3 Measurements 119
7.3.1 150 nm Quantum Dot Z212B 119
7.3.2 150 nm Quantum Dot SALSA 124
7.4 Conclusions 128
References 130

Chapter 8 Spectroscopy of Quantum Dots with Few Electrons 132

8.1 Introduction 132
8.2 Electron Spectroscopy in Quantum Dots with Few Electrons 133
8.3 Measurements 136
8.4 Quantum Dots with Few Electrons in a Magnetic Field 141
8.5 Measurements 143
8.5.1 150 nm Quantum Dot Z212A in a Magnetic Field 143
8.5.2 150 nm Quantum Dot SALSA in a Magnetic Field 145
8.6 Conclusions 148
References 150

Chapter 9 Conclusions 152

9.1 Introduction 152
9.2 Surface Gated Quantum Dots at and above 1.2 K 152

Appendix **Developments in the field since the work described in this thesis was completed** **155**

List of Figures

2.1 Schematic energy diagram of a modulation doped GaAs-AlGaAs heterostructure illustrating the formation of quantised energy levels in the triangular potential well formed at the heterojunction. 7

2.2 Graph depicting the quasi-two dimensional density of states which results from confinement at the interface of a suitably designed GaAs-AlGaAs heterostructure. 9

2.3 Conduction band edge in a slab doped GaAs-AlGaAs heterostructure with a surface potential V_0 and a Fermi energy E_F. The two dimensional electron gas is formed at a distance c+d+s from the surface of the structure and in this illustration shows one bound sub-band E_0 . The conduction band offset between the GaAs and AlGaAs conduction bands is ΔE_c and the deep donor pinning energy is E_{dd}. 10

2.4 Illustration of electron trajectories in the diffusive (l<<L,W), quasi-ballistic (W<l<L) and ballistic (l>>L,W) regimes with specular scattering at the boundary of the conductor. 15

2.5 Subband energy versus longitudinal wave vector k_y assuming a parabolic confinement potential. The 1D subbands are separated by $\hbar\omega_0$. The net current results from the uncompensated occupied electron states in the interval between μ_1 and μ_2, where μ_1 and μ_2 are the chemical potentials of the wide 2DEG reservoirs. 17

2.6 Occupation of Landau levels in a magnetic field with its associated filling factor. The movement of the occupied Landau

levels with respect to the Fermi energy is also shown[1]. 22

2.7 Potential energy and lowest eigenstate in a magnetic field for an electron with wavevector k in a hard walled wire of width 0.1 μm in GaAs[1]. 26

3.1 (a) Layer structure of a modulation-doped shallow GaAs-AlGaAs heterostructure with the indication of the 2DEG (The boundary between the spacer and conduction layers is indicated with a solid line). (b) and (c) schematic layout and cross-section of the fabricated device in Hall-bar geometry. 34

3.2 Schematic illustration of a photolithographic process: (a) irradiation of the photoresist through the mask, (b) undercut resist profile after development, (c) sample after metal evaporation, (d) metal layer on the sample after lift-off, (e) resist profile before chemical etch, (f) sample after chemical etch, (g) etched sample after washing off the photoresist. 36

3.3 Illustration of the data pattern for the four layers used for device fabrication : (a) Pattern for ohmic contacts, (b) Isolation, (c) Gate pattern defining a four-gated quantum dot, (d) Wiring layer, connecting the Schottky gates to the gate voltage pads, (e) Microdevice in Hall-geometry comprising four layers. The four data patterns (a),(b),(c) and (d) are not to scale, for example (c), data pattern for surface gates fills the gaps in the middle of the wiring level pattern as shown in (e). 41

3.4 Pattern data showing the gated region of the sample, comprising four data layers. (b) Schematic drawing depicting the gate pattern for the centre of a four gated quantum dot. The four gates are indicated by G1, G2, G3 and G4. 45

3.5 A scanning electron micrograph showing, (a) the gated region of a sample, (b) a typical 150 nm quantum dot. The light region is the surface of the semiconductor heterostructure and the darker regions are the four Schottky gates. The distance of 150 nm on the micrograph is indicated by the length of the dotted line in the lower right hand corner. 46

4.1 Schematic diagram of an Oxford Instruments Variable Temperature Insert. 53

4.2 Scanning electron micrograph of a surface gated quantum dot damaged by electrostatic discharge effect. The dark areas are the tips of the Schottky gates separated from the surface of the semiconductor. 55

4.3 Schematic diagram of the measuring system. The cryostat with the sample is located in the screened room to minimise RF noise. The voltage preamplifiers are placed close to the cryostat head in order to reduce the pick-up noise. 57

4.4 Schematic diagram showing the improved low frequency conductance measurement set up with a current preamplifier working with a noise level of 20 fA. 58

5.1 (a) General schematic plan view of a surface gated quantum dot measured during the course of the project. The Schottky gates are indicated by G1, G2, G3 and G4. (b) Potential landscape of the quantum dot in the 2DEG created by the gates G1, G2, G3 and G4. μ_S and μ_D are the chemical potentials of the 2DEG reservoirs (source and drain respectively). φ_N is the electrostatic potential with N electrons in the quantum dot. E_N is the energy

level of the Nth electron in the dot, relative to the bottom of the conduction band. (c) Equivalent circuit of (b), using two voltage sources. 65

5.2 Two characteristic situations for different G2 voltages. (a) Coulomb blockade of electron tunnelling ($\mu_d(N)<\mu_D<\mu_S<<\mu_d(N+1)$). (b) Electron tunnelling at the N $\rightarrow$ N+1 transition ($\mu_S<\mu_d(N+1)<\mu_D$). V indicates the excitation voltage across the sample ($eV<<\mu_d(N+1)-\mu_d(N)$). 67

5.3 Comparison of the conductance G (a), and the number of electrons N_{dot} (b) in the quantum dot. Between the Coulomb oscillations N_{dot} remains constant, which corresponds to the Coulomb blockade (see Figure 5.2a). At the maximum of the oscillations, N_{dot} oscillates by one electron, and $e\varphi$ oscillates by e^2/C. In this case, the Coulomb blockade is removed, and single electron transport through the quantum dot becomes possible. 68

5.4 (a) Geometry of the semi-infinite gate occupying x<0 on the surface of the heterostructure which defines the plane z=0. The 2DEG lies in the plane z=d with the region x>b occupied. (b) Conformal transformation to the ξ plane. The edge of the 2DEG maps to ξ=-1, and the edge of the gate maps to $\xi=\beta$. 71

5.5 Single particle energy level spacing inside the quantum dots as a function of effective dot radius for different 2DEG depths, calculated using the frozen surface model. 75

5.6 Geometry of the metal gate on the surface of a heterostructure. The 2DEG lies in the plane z=d, partially occupying it. 76

5.7 (a) Geometry of quantum dot Z19A formed with four metal gates

G1, G2, G3, G4. (b) Conductance oscillations as a function of the plunger gate voltage at 1.2 K with G1=-0.82 V, G3=-0.73 V and G4=-0.82 V on the gates. 79

5.8 Conductance oscillations in quantum dot Z20A as a function of plunger gate voltage at 1.2 K with G1=-0.71 V, G3=-0.65 V and G4=-0.71 V on the surrounding gates. 80

5.9 Conductance oscillations in quantum dot Z2B as a function of plunger gate bias at 1.2 K and gate bias conditions G1=-0.53 V, G3=-0.53 V and G4=-0.535 V. Note the change of shape of oscillations at more negative gate voltages. 80

5.10 Conductance oscillations in Quantum Dot Z27A as a function of the plunger gate voltage at 1.2 K and with G1=-0.46 V, G3=-0.45 V and G4=-0.48 V on the gates. Note the change in the period of oscillations at increasingly more negative gate voltages. 83

5.11 Conductance oscillations in Z27B as a function of the plunger gate voltage at 1.2 K with gate bias condition G1=-0.37 V, G3=-0.37 V and G4=-0.37 V. 83

5.12 Schematic diagram depicting double gated (a) single, (b) double and (c) quadruple quantum dots. The distance between each the gate pair defining the single, double and quadruple quantum dots is 90 μm. 84

5.13 Micrograph of the 150 nm quantum dot. (b) the bare electrostatic potential contours for a quantum dot in the same configuration with a bias of -0.5 V (top) and -0.7 V (bottom) on the plunger gate, and -0.5 V on all other gates. Note the change of the shape

of the electrostatic potential contours. 85

6.1 *Plot of GT versus* $\frac{E_0}{kT}$. 97

6.2 Conductance oscillations in the 350 nm quantum dot at 1.2 and 4 K. The oscillations are thermally broadened and disappear just above 4 K. 97

6.3 Temperature dependence measurement in quantum dot Z20A. The conductance oscillations disappear at around 4 K as a result of thermal smearing. There are some oscillations still visible at 5 K between -0.76 and -0.8 V. 99

6.4 Coulomb blockade oscillations in the 150 nm quantum dot Z2B. The period of oscillations changes at more negative gate voltages. 99

6.5 Conductance oscillations in the 150 nm quantum dot at 5.6 K, 6.8 K and 7.7 K. The oscillations smears out above 7.7 K. 101

6.6 Plot of ln(GT) as a function of reversed temperature 1/T for the three consecutive minimas M1, M2 and M3 (see Figure 6.4). The gradient of the fitted lines gives the energy level separation in the quantum dot at a particular conductance minimum. 101

6.7 Coulomb oscillations in quantum dot Z212B as a function of gate voltage (all gates interconnected) at different temperatures. 103

6.8 Temperature dependence of Coulomb oscillations in dot Z212B at 3.2 K, 4 K, 6 K and 7.1 K. 103

6.9 Graph of ln(GT) as a function of 1/T for the three conductance minimas M1–M3 in Figure 6.8. 104

6.10 Conductance oscillations in the 100 nm quantum dot Z27B. 104

6.11 Graph of ln(GT) versus 1/T in the 100 nm quantum dot Z27B. 106

6.12 Coulomb blockade oscillations for dots of nominal diameter 350 nm, 250 nm, 150 nm and 100 nm at a temperature of 1.2 K. The plunger gate voltage is varied, with all the other gates held at a fixed voltage. 109

7.1 Schematic capacitor circuit of a single quantum dot indicating the capacitances of the dot to the source, drain and the gates (C_S, C_D, and C_g respectively). The electrostatic potential inside the dot is ϕ, and two voltage sources are used to vary the voltage both on the gates and between the source and drain. The tunnelling conductances onto the dot are assumed to have a small effect on the bias. 115

7.2 The stability diagram of a quantum dot system, when the dot is capacitatively coupled to the source, drain and the surrounding gates. The quantum dot conducts only outside the rhombic-shaped regions indicated by CB (Coulomb Blockade). Inside the regions the number of electrons in the dot is fixed, electron transport through the dot is blockaded. In the rhomboids indicated by SET (Single Electron Tunnelling) the electrons pass through the dot one by one. 117

7.3 Conductance oscillations under different DC source-drain bias. 120

7.4 Coulomb oscillation peaks persist at 6 mV DC source-drain bias. 120

7.5 Quantum dot Z212B in 0 – -3 mV DC source-drain bias voltage range. 122

7.6 Oscillation peaks in the -6 – -8 mV DC bias voltage range. Note the shift of curves towards more negative gate voltage with increasing DC source-drain bias. 122

7.7 State 3 of quantum dot Z212B. Note the change in the amplitude and period of the oscillations. 123

7.8 Plot of conductance maximas as a function of gate voltage at different DC source-drain bias. 123

7.9 DC source-drain characteristics in quantum dot SALSA in State 1. (The lines on the graph are for indication only.) 125

7.10 DC characteristics of dot SALSA in State 2. 125

7.11 DC source-drain characteristics of quantum dot SALSA in State 3. 127

8.1 Conductance of quantum dot SALSA as a function of G2 voltage, measured at 1.3 K. The parameters are the voltages applied to the other three gates G1, G3 and G4. 137

8.2 The positions of the conductance peaks in dot SALSA as a function of DC source-drain bias, measured at 1.3 K. 137

8.3 Plot of E_{nl} versus the magnetic field for increasing electron number in the quantum dot at $\hbar\omega_0$=3 meV. 142

8.4 Quantum dot Z212A in a magnetic field at 0 and 0.5 T. 144

8.5 150 nm quantum dot Z212A at 0.5, 1 and 1.5 T. The three superimposed oscillation peaks are clearly visible on both main oscillation peaks. 144

8.6 Coulomb blockade oscillations in quantum dot Z212A, measured between 2 and 3 T. 146

8.7 Quantum dot SALSA in a magnetic field. 146

8.8 Quantum dot SALSA in high magnetic fields. Note the separation of the superimposed conductance peaks into two main peaks. 147

List of Tables

5.1 Single particle level spacing values and expressions obtained using both pinned and frozen surface approximations. 74

5.2 Number of electrons N in the quantum dot for different V_g/V_T ratio. The electron depth is 28 nm, sheet electron density is 5 10^{15} $1/m^2$, b is the depletion length and a is the radius of the electron pool in nanometres. 77

5.3 Comparison of single particle spacing for surface gated quantum dots of different lithographic diameter, assuming 50 nm depletion region. 87

5.4 Conductance modulation depending on the lithographic diameter of the quantum dot. 87

6.1 Energy gaps in three quantum dots with the corresponding estimated smearing temperatures. 107

8.1 Parameters of 150 nm quantum dots Z212A and SALSA. 138

Abstract

In this thesis we demonstrate that surface gated quantum dots working in the high temperature regime (between 1.2 K and 7.7 K), can be reproducibly fabricated using the combination of state of the art electron beam lithography and shallow GaAs-AlGaAs heterostructures. Surface gated quantum dots with 4 electrodes and with nominal dot sizes between 100-350 nm were fabricated and characterised.

We present the theory of electron transport in heterostructures with emphasis being put on electron transport in shallow GaAs-AlGaAs heterostructures where the two dimensional electron gas (2DEG) is 28 nm below the surface of the semiconductor. The theory of electron transport in point contacts (PCs) and in quantum dots is discussed in detail. We present the quantum dot design considerations for achieving device operation in the high temperature regime, design details, sample fabrication and sample handling procedures.

The experimental setup for measuring our surface gated quantum dots and data acquisition technique is presented. Temperature dependence measurements between 1.2 K-9.6 K are presented for quantum dots with different nominal sizes. We discuss an improved measurement setup designed for electron transport measurements in quantum dots in the low conductance regime.

We show in this work that theoretical calculations and detailed modelling can assist in the design of quantum dots for operation in the high temperature regime. We describe the optimisation of our quantum dots, which led to a fabrication and measurement of very small dots containing only a few electrons. At the time when our research work was carried out, the surface gated quantum dots detailed in this work showed the highest operating temperature reported in literature for devices of this type. The benefits of quantum dots operating at high temperatures are discussed.

We show the existence of electron-electron interaction effects in these quantum dots at 1.2 K normally observed in surface gated quantum dots in the millikelvin temperature range. The effect of a magnetic field applied

perpendicularly to the plane of our quantum dot in the few electron regime is reported and discussed.

We show that surface gated quantum dots containing only a few electrons optimised for high temperature performance can be used for electron spectroscopy measurements and can yield interesting effects.

We discuss the intrinsic drawbacks and difficulties associated with the operation of small surface gated quantum dots fabricated on shallow GaAs-AlGaAs heterostructures. The effects of the semiconductor surface and material imperfections on our quantum dot performance is also shown.

Finally we discuss the prospect for using shallow GaAs-AlGaAs heterostructures in quantum dot devices and some possible future research directions in the field of surface gated quantum dots.

Chapter 1

Introduction

1.1 Surface Gated Quantum Dots

A semiconductor quantum dot is a small structure in which a two-dimensional electron gas, realized in a semiconductor heterostructure, is laterally confined to form a disk-shaped, zero-dimensional electron system. As a result of reduced dimensionality, quantum confinement and novel transport behaviour can be observed in these systems. Electronic transport studies through a quasi-zero-dimensional electron system show interesting effects. If the thermal energy k_BT is small compared to the electrostatic energy required to add one additional electron to the zero-dimensional electron system, conductance oscillations as a function of the electro-chemical potential of the island are observed. These oscillations are usually called Coulomb blockade (CB) oscillations.

Much interest has developed in a number of applications of the Coulomb blockade phenomenon, in metrology, detection, and in making single electron devices for future nanoscale integrated circuits. Although Coulomb blockade has been observed at temperatures up to 300 K and beyond in systems such as granular films and scanning probe tips, realization of useful device structures using these technologies is difficult. Structures such as metal-insulator-metal tunnel junction arrays, or laterally patterned quantum dots are fully controllable but require much lower temperatures for operation, limiting their utility. Tunnel junction structures generally show charging effects at millikelvin temperatures, and although an increase

in temperature to 4 K may be possible, this will require junction sizes 30 nm square or less, placing demanding requirements on the lithography. Surface gated semiconductor quantum dots which are easier to fabricate than ultrasmall tunnel junctions have so far only shown charging effects at temperatures below 4 K.

1.2 Aim of work

The main aim of this thesis was to demonstrate that our surface gated quantum dots fabricated using state of the art electron beam lithography and shallow heterostructure technology can operate at and above 4 K. To achieve the highest temperature operation of the surface gated quantum dots, their dimensions were gradually reduced. This led to the demonstration of electron-electron interaction effects in the smallest quantum dots. The exploration of these effects in the few electron regime is also an important aim of this work.

1.3 Chapter summary

Chapter 2 describes the terminology and theory of electron transport in heterostructures. The characteristic physical properties of shallow 2DEGs are detailed and different transport regimes are described. Electron transport in heterostructures in a magnetic field is discussed and the effects and main features of the QPC (Quantum Point Contact) as a building block for quantum dots are described. The discussion is extended to electron transport in series QPCs which serves as an introduction to surface gated quantum dots.

Chapter 3 describes the design and fabrication of surface gated quantum dots. The methods and main principles of optical and electron beam lithography are described. The complete sequence of fabrication of ultrasmall surface gated semiconductor devices and surface gated quantum dots is presented. The fabrication

of all the layers is described, with emphasis being laid on the surface gate level. The processes of sample inspection and sample bonding are also described.

Chapter 4 presents the measurement method used to characterize the surface gated quantum dots. The cryogenic equipment used for measurements below and above 1.2 K are described. The working principles of a dilution refrigerator insert and the variable temperature insert are detailed. Special emphasis is put on the description of sample handling and mounting of the highly sensitive quantum dots. The lock-in measurement technique and the data acquisition method are also presented. Different modes of measurement are described, and improvements made to the measuring techniques during the course of the project are also discussed.

Chapter 5 deals with the theory of charging effects in quantum dots and the process of device optimisation for operation in the highest achievable temperature regime. The pinned surface and frozen surface approximations for the behaviour of a heterostructure in depletion are described. The depletion length in the 2DEG under the surface gate is calculated, and experiment and modelling is compared. Coulomb blockade measurements in a range of quantum dots are presented. The modelling of electrostatic potential and the number of electrons in our quantum dots is described.

Chapter 6 details the temperature measurements carried out on our quantum dots. The theory of temperature dependence is presented and the line shape dependence of Coulomb oscillations is described. The effect of the physical dimensions and shape of the dot on the single particle energy level separation is described. The temperature dependence measurements in the range of surface gated quantum dots, including the comparison of experimental and calculated smearing temperatures, are discussed.

Chapter 7 describes the DC source-drain measurements which is used to determine critical quantum dot parameters. The theory of the Coulomb blockade boundary is introduced. The "Coulomb diamonds" for each of the measured quantum dots are presented. This chapter describes the effect of the tunnel barriers and the surface gates on the single-electron transport through the quantum dot.

Chapter 8 deals with spectroscopy measurements in quantum dots with few electrons. The theory of electron spectroscopy in quantum dots is presented and the structure of Coulomb blockade oscillations in the few electron regime is explained. The theory of electron spectroscopy in quantum dots is extended to the magnetic fields, and is used to explain the intriguing results.

Finally Chapter 9 summarizes our work and presents the main achievements of this thesis. The negative points of this work are also discussed and possible future research direction is laid.

Chapter 2

Theory of Electron Transport in Heterostructures

2.1. Introduction

In this chapter the theory of electron transport in a silicon doped GaAs AlGaAs heterostructures will be discussed. The formation of a two dimensional electron gas (2DEG) at the GaAs-AlGaAs interface is reviewed. Electron transport in this region in one-dimensional structures resulting from electrostatic confinement is described. The working principles of surface gated quantum devices such as quantum point contacts (QPCs) and double junction systems forming quantum dots (QDs) are reviewed. Finally, electron transport in both two and one dimension, in the presence of a magnetic field perpendicular to the electron transport plane is described.

2.2. GaAs-AlGaAs Heterostructures

The collection of layers of more than one kind of semiconductor material is called a heterostructure. The active regions of devices are typically at or close to the heterointerfaces, where the materials are joined to one another[1]. The interfaces which make up a heterostructure are called heterojunctions. The semiconductors which make up the heterojunction will have different band gaps and this causes discontinuities in the conduction and valence band edges. These band discontinuities can establish a potential well for carriers on the side of a smaller-gap material. Thus in the case of GaAs-AlGaAs heterostructure the potential well for electrons is formed at the interface due to the conduction band

offset between the two semiconductors. The electrons are confined in a direction normal to the interface, but free to move along it. To achieve high electron mobility in the active region, heterostructures must have interfaces of particularly high quality: the structures of the two materials must match onto one another, and the interface must not be contaminated with impurities or suffer from other defects. To meet these criteria, sophisticated processes like molecular-beam epitaxy (MBE)[2] and metal-organo-chemical vapour deposition (MOCVD) are used.

2.3. Modulation doped GaAs-AlGaAs Heterostructure

The modulation doped GaAs-AlGaAs heterostructures, grown by MBE, have long been the subject of experimental investigation. In these structures the AlGaAs material is doped, and the requirement to maintain a constant chemical potential throughout the structure, leads to the ionisation of the impurities in the AlGaAs and transfer of electrons across the interface. This charge transfer puts conducting electrons in a high-purity, high-mobility GaAs without directly introducing mobility-limiting donor impurities[3]. As shown in the band-bending diagram[4] of Figure 2.1, the electrons are confined to the GaAs-AlGaAs interface by a potential well, formed by the repulsive barrier due to the conduction band offset (ΔE_c) of about 0.3 eV between the two semiconductors, and by the attractive electrostatic potential due to the positively charged ionised donors in the n-doped AlGaAs layer. In order to reduce scattering from these ionised donors, the doped layer is separated from the interface by an undoped AlGaAs spacer layer.

If carrier confinement is strong enough, bound states can be formed which have low enough energies to be filled in equally. In case of an isotropic semiconductor that has energy bands in three dimensions which can be approximated by parabolic wells, we arrive at the dispersion relationship given in Equation 2.1 for the allowed carrier energies $E_n(k)$ in the well. E_n are the

confinement levels, m^* is the effective mass of an electron in GaAs and k_x and k_y are the wave vectors associated with electron transport in the x and y planes.

$$E_n(k) = E_n + \frac{\hbar^2 k_x^2}{2m^*} + \frac{\hbar^2 k_y^2}{2m^*} \tag{2.1}$$

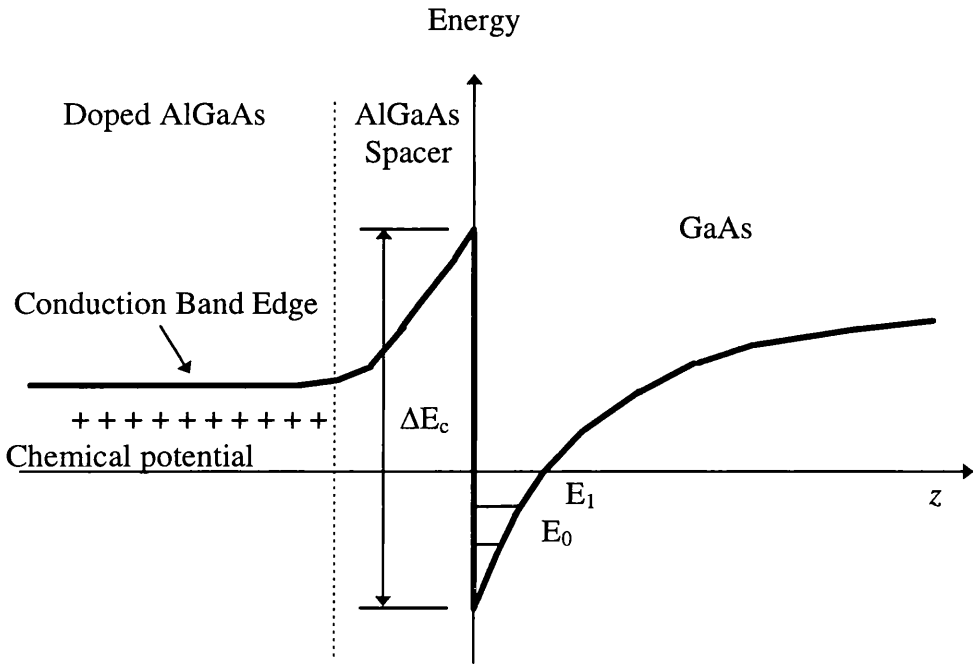

Figure 2.1: *Schematic energy diagram of a modulation doped GaAs-AlGaAs heterostructure illustrating the formation of quantised energy levels in the triangular potential well formed at the heterojunction.*

Hence, E_n forms the bottom of a band of allowed energy states associated with motion parallel to the interface. Each group of energy states is known as a subband. The formation of subband structure has surprising implications for the density of states in the potential well. Consider the number of states in two dimensional k-space $n(k)\delta k$ that lie in the interval $k \rightarrow k+\delta k$

$$n(k)\delta k = D(k)2\pi k\delta k \tag{2.2}$$

where $D(k)=1/(2\pi)^2$ is the density of states per spin in two dimensions. If $D(E)$ is the density of states in the corresponding energy interval $E \rightarrow E+\delta E$, then the total number of states in this energy interval will be given by

$$D(E)\delta E = n(k)\delta k = \frac{1}{(2\pi)^2} 2\pi k \delta k$$

Hence

$$D(E) = g_s g_v \left[\frac{2\pi}{k} \frac{dE_n(k)}{dk} \right]^{-1}_E$$

where g_s is the spin degeneracy of the electron and $g_v=1$ is the valley degeneracy of the conduction band edge in GaAs. Using Equation 2.2 to substitute for E

$$D(E) = \frac{g_s g_v m^*}{\pi\hbar^2} \qquad \text{for } E>E_0 \qquad (2.3a)$$

and

$$D(E)=0 \qquad \text{for } E<E_0 \qquad (2.3b)$$

It is apparent from Equation 2.3a and b that the density of states is a constant in any subband, and zero below the subband edge[5]. As the energy increases, more of the subbands become populated and the density of states increases in units of $m^*/\pi\hbar^2$, see Figure 2.2.

At zero temperature , all states are filled up to the Fermi energy E_F (this is a good approximation at finite temperature if the thermal energy $k_BT<<E_F$). If the doping level in the AlGaAs is properly chosen, it is possible to reduce the Fermi energy to such a level that only the first subband is occupied. This subband constitutes a two dimensional electron gas (2DEG). The main importance of this type of 2DEG is that ionised impurity scattering is reduced due to the spatial separation of the conduction electrons in the undoped GaAs from the donors in

the AlGaAs. Additional reduction in ionised impurity scattering can be achieved by including a region of undoped AlGaAs between the donors and the confined electrons. As a result of these effects, high mobility electron gas is formed in the GaAs at the spacer AlGaAs, GaAs heterojunction.

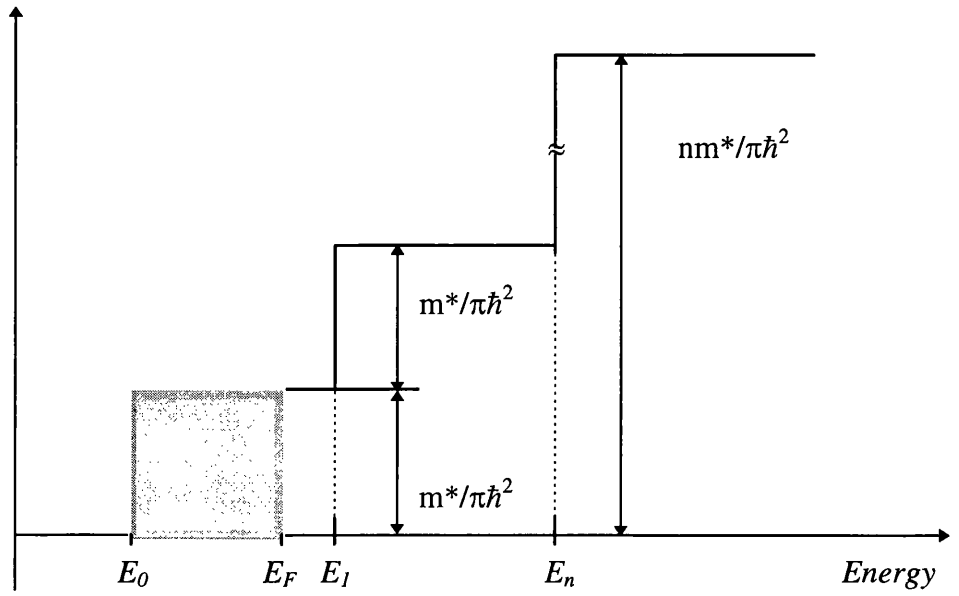

Figure 2.2: *Graph depicting the quasi-two dimensional density of states which results from confinement at the interface of a suitably designed GaAs-AlGaAs heterostructure.*

2.4. Two Dimensional Electron Gas (2DEG)

A 2DEG in a AlGaAs heterostructure is usually characterised by the mobility and carrier concentration of the confined electrons. The carrier concentration ideally depends only on the spacer width, the pinning energy of the chemical potential by deep donor states and the conduction band offset, see Figure 2.3. In order to accurately understand these dependencies, it is necessary to calculate the energy levels in the 2DEG. This is done by solving Poisson's equation to find the confining potential, while simultaneously taking into account the effects on this potential of populating the potential well. If the effect of the

electron population on the energy levels in the well is ignored, then too high a value for the position of the energy levels is deduced. For accurate results a self-consistent solution of Poisson's equation and Schrödinger's equation is required, taking into account all energy related effects for the electronic charge distribution in the 2DEG. Having said this, much can be learned simply approximating the confinement as a triangular potential well and solving Poisson's equation in order to find the magnitude of the confining potential[6]. The problem then reduces to simply finding the eigenstates of this potential well and integrating the charge

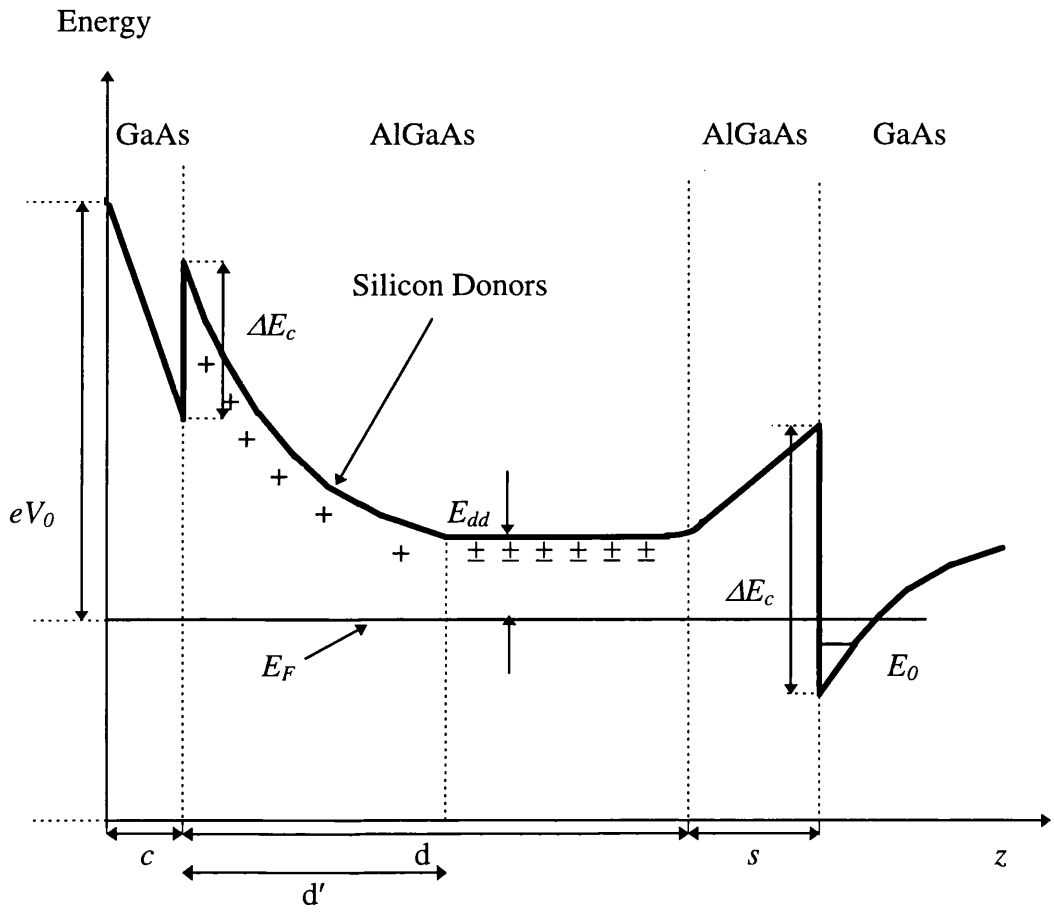

Figure 2.3: *Conduction band edge in a slab doped GaAs-AlGaAs heterostructure with a surface potential V_0 and a Fermi energy E_F. The two dimensional electron gas is formed at a distance c+d+s from the surface of the structure and in this illustration shows one bound sub-band E_0. The conduction band offset between the GaAs and AlGaAs conduction bands is ΔE_c and the deep donor pinning energy is E_{dd}.*

throughout the structure. Assuming that the Fermi energy in the central region of the donor layer is pinned on the deep donor states[7] at an average energy E_{dd} below the conduction band and that tunnelling out of the 2DEG can be neglected at low temperatures then the carrier concentration n_{2D} in a 2DEG of effective thickness a is given by Equation 2.4.

$$n_{2D} = \frac{(\Delta E_c - E_{dd})\varepsilon_0}{\left(\frac{s}{\varepsilon_a} + \frac{a}{\varepsilon_g}\right)e^2} \tag{2.4}$$

where ε_a (ε_g) in Equation 2.4 is the relative permittivity of AlGaAs (GaAs) respectively.

Therefore, as a result of the pinning of the chemical potential by the deep donor centres, the 2DEG charge density is determined entirely by simple energy parameters and the geometry of the layers, not by the total number or the density of donors.

In addition, it can readily be shown that the conduction band edge E_C can be expressed as a function of the electric field at the interface of the 2DEG with the GaAs-AlGaAs (defined as z=0), donor concentration N_d, cap thickness c, and a geometric parameter d' which defines the spatial extent of the depletion region, see Equation 2.5.

$$E_c(0) = -eF_a\left(\frac{a\varepsilon_a}{\varepsilon_g} + s\right) + \frac{N_d e^2}{\varepsilon_0}\left(\frac{d'^2}{\varepsilon_a} + \frac{d'c}{\varepsilon_g}\right) \tag{2.5}$$

2.5. Surface Gated GaAs-AlGaAs Heterostructure

After a heterostructure has been designed and grown with a certain carrier concentration, it is often desired to vary this concentration[7]. This is usually achieved by patterning and depositing Schottky contacts onto the surface of the heterostructure and applying an external electric field using a voltage source. As a

result, the confined carriers in the 2DEG beneath the surface gates will experience a repulsive force and at a high enough negative voltage will be expelled from beneath the gates. In order to understand how the depletion of the donors takes place, it is necessary to understand the role played by *DX* centres in the dopant region. There are two cases to be considered. The first is that for high temperatures, where the *DX* centres are active, i.e. they can be depleted. As negative bias is applied to the gate, d' increases until it becomes equal to d, when all the donor centres are depleted. Further application of negative bias removes the charge from the channel, giving zero field there. This is at this point, when the gate voltage V_g equals the threshold voltage V_T Hence assuming that the surface states are in equilibrium with the gate electrode, then the conduction band edge at the surface of the heterostructure is given by Equation 2.6, where V_0 is the potential of the free GaAs surface.

$$E_c(0) = e(V_0 - V_g) = e(V_0 - V_T) \tag{2.6}$$

Hence substituting into Equation 2.5 for E_c *(0)* with $d=d'$ and F_a set to zero gives

$$e(V_0 - V_T) = \frac{N_d e^2}{\varepsilon_0}\left(\frac{d^2}{2\varepsilon_a} + \frac{dc}{\varepsilon_g}\right) \tag{2.7}$$

This equation enables the threshold voltage, V_T in the active state to be computed.

The second case applies at low temperatures, when the electrons are trapped in the *DX* centres. These centres become frozen and cannot be depleted by the application of a voltage bias. However, the DX centres can be ionised at low temperature by illuminating the structure with radiation which supplies an energy greater than the maximum height of the energy barrier. In the case of frozen *DX* centres there is an extra contribution to the surface potential due to their electric field F'_a. Hence the conduction band edge at the surface of the heterostructure for frozen *DX* centres is given by

$$E_c^f(0) = \frac{N_d e^2}{\varepsilon_0}\left(\frac{d'^2}{2\varepsilon_a} + \frac{d'c}{\varepsilon_g}\right) + eF'_a\left(d + \frac{c\varepsilon_a}{\varepsilon_g}\right) \tag{2.8}$$

Solving Poisson's equation to find F'_a, Equation 2.8 can be simplified to give an expression for the bias at which the channel is fully depleted in terms of the geometry of the heterostructure and the zero bias carrier concentration in the 2DEG, see Equation 2.9.

$$V_T^f = -\frac{e}{\varepsilon_0} n_{2D}\left(\frac{c}{\varepsilon_g} + \frac{d}{\varepsilon_a} + \frac{s}{\varepsilon_a} + \frac{a}{\varepsilon_g}\right) \tag{2.9}$$

The threshold voltage in this frozen approximation depends strongly on fixed constants and geometry. This effectively puts a limit on the minimum threshold voltage that can be designed into a heterostructure for a given doping density.

2.6. Electron transport in a Two Dimensional Electron Gas

With the application of an electric field in the plane of the 2DEG, an electron acquires a drift velocity $\underline{v}=-e\underline{E}\Delta t/m$ in the time Δt since the last impurity collision. The average of Δt is the scattering time τ, so the average drift velocity $\underline{v}_{drift}$ is given by

$$\underline{v}_{drift} = -\mu_e \underline{E} \qquad \mu_e = e\tau/m \tag{2.10}$$

The electron mobility μ_e together with the sheet density n_s determine the conductivity σ in the relation $-en_s\underline{v}_{drift} = \sigma\underline{E}$. The result is the Drude conductivity, which can be written in several equivalent forms:

$$\sigma = en_s\mu_e = \frac{e^2 n_s \tau}{m} = g_s g_v \frac{e^2}{h}\frac{k_f l}{2} \tag{2.11}$$

In the last equality we have used the identity $n_s=g_s g_v k_F^2/4\pi$ and have defined the mean free path $l=v_F\tau$. The dimensionless quantity $k_F l$ is much greater than unity in metallic systems, so the conductivity is large compared with the quantum unit $e^2/h \approx 38\ \mu S$.

Experimentally it is the conductance G that is measured and this is related to the conductivity of a sample of width W and length L through Equation 2.12:

$$G = \frac{W}{L}\sigma = \frac{W}{L} e\mu_e n_{2D} = \frac{e^2}{h}\frac{W}{L}\frac{k_F l}{2} \tag{2.12}$$

Equation 2.12 describes the elastic scattering of electrons at the Fermi surface with wave vectors k_F and can now be used to define three different transport regimes: diffusive, quasi-ballistic and ballistic, depending on the relative size of the mean free path compared to the sample dimensions, see Figure 2.4.

2.6.1 Diffusive Transport Regime

In the diffusive transport regime, where $L,W>>l$, quantum interference effects can produce deviations from the predictions of classical transport theory. These interference effects result from phase differences acquired by an electron wave in travelling between two points in the sample along different possible trajectories[8].

2.6.2 Quasi-ballistic Regime

Modern technology permits the fabrication of structures in which $W<l<L$. In this quasi-ballistic regime the conductance is determined by a combination of specular boundary effects and impurity related elastic scattering events.

2.6.3 Ballistic Regime

In the ballistic limit , where $L,W<<l$, Equation 2.12 does not hold as there are no scattering centres in the sample. In this regime the conductivity, as defined in Equation 2.8, has no meaning and the conductance is determined solely by sample geometry[9] and specular scattering from the sample boundaries[10].

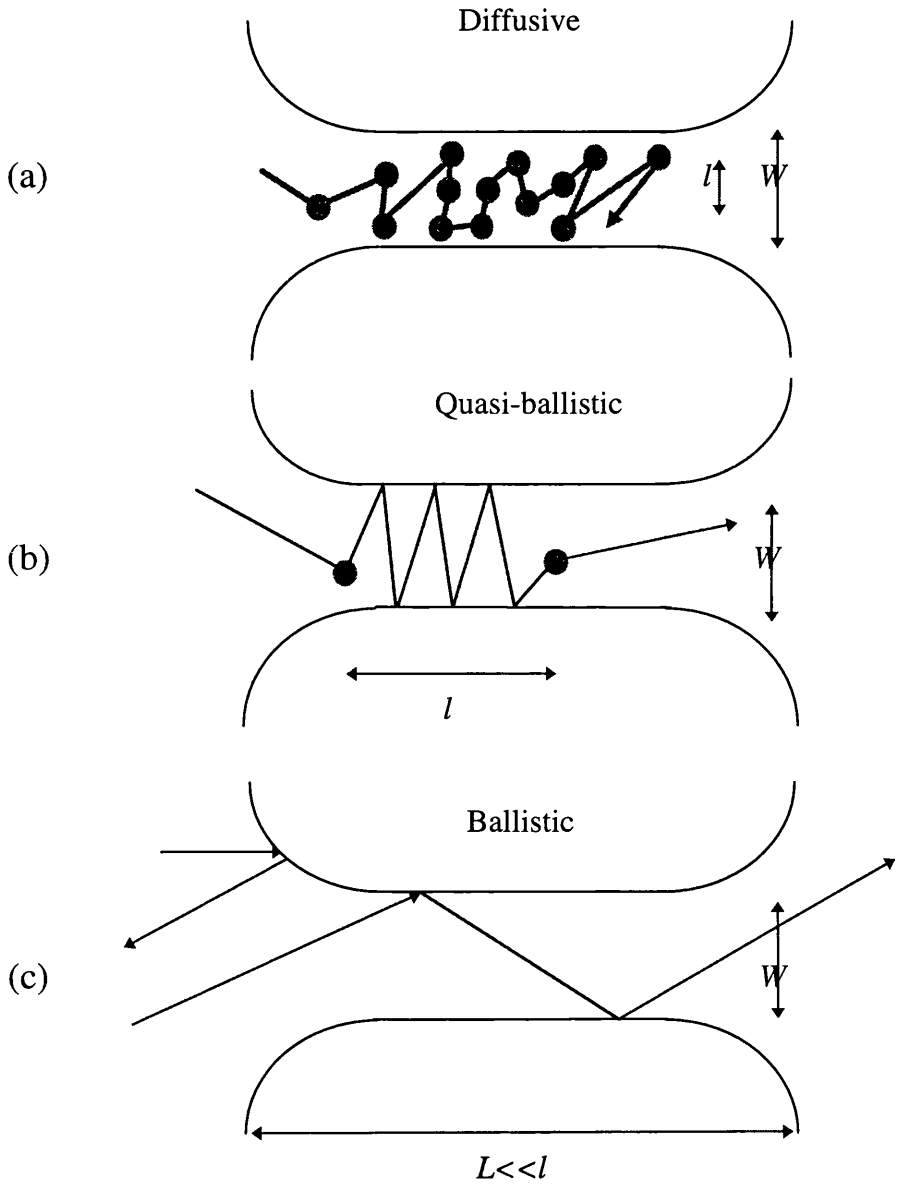

Figure 2.4: *Illustration of electron trajectories in the (a) diffusive ($l<<L,W$), (b) quasi-ballistic ($W<l<L$) and (c) ballistic ($l>>L,W$) regimes with specular scattering at the boundary of the conductor.*

2.7. Adiabatic Electron Transport

In this section electron transport in reduced dimensions in surface gated GaAs-AlGaAs heterojunctions will be discussed. Transport throughout two tunnel barriers in series will also be discussed. Finally, the theory for single electron transport in surface gated QPCs is presented.

2.7.1 Quantum Point Contacts

Quantum point contacts (QPCs) are the most elementary tool for the study of ballistic and adiabatic electron transport and the building elements of a split-gate quantum dot[11]. These are short and narrow constrictions in a 2DEG, with a width of the order of the Fermi wavelength. The most dramatic phenomenon observed in QPCs was the observation of quantized plateaux at multiples of $2e^2/h$ in the conductance of the QPCs, measured as a function of the gate voltage.

We now show the conductance quantization from transport through 1D subbands. Quasi-one dimensional transport in the ballistic regime is determined by the Hamiltonian :

$$H = \frac{p_x^2}{2m^*} + \frac{p_y^2}{2m^*} + eV(x) \tag{2.13}$$

where m^*=0.067 m_0 is the effective mass in GaAs. The narrowest point in the QPC completely determines the transport properties. If the confinement is commensurate with the Fermi wavelength of the electrons in the 2DEG and assuming a parabolic confinement potential, the resulting Schrödinger equation can be written in the form of that for a harmonic oscillator having energy eigenvalues :

$$E_n(k) = \left(n - \frac{1}{2}\right)\hbar\omega_0 + \frac{\hbar^2 k^2}{2m^*} \qquad n=1,2,... \tag{2.14}$$

which contains a free-electron kinetic energy dispersion in the longitudinal y-direction. In the x-direction the energy states, indexed by n=1,2,..., are quantized and separated in energy by $\hbar\omega_0$. Equation 2.14 describes 1D subbands, because the electron motion is free in one direction only. Figure 2.5 shows the 1D subband dispersion versus longitudinal wavevector k_y. The right-going electrons originate from the left 2DEG reservoir, which populates at zero temperature all the states up to its electro- chemical potential μ_1. The left-going electron states are occupied up to μ_2, the electro-chemical potential of the right 2DEG reservoir.

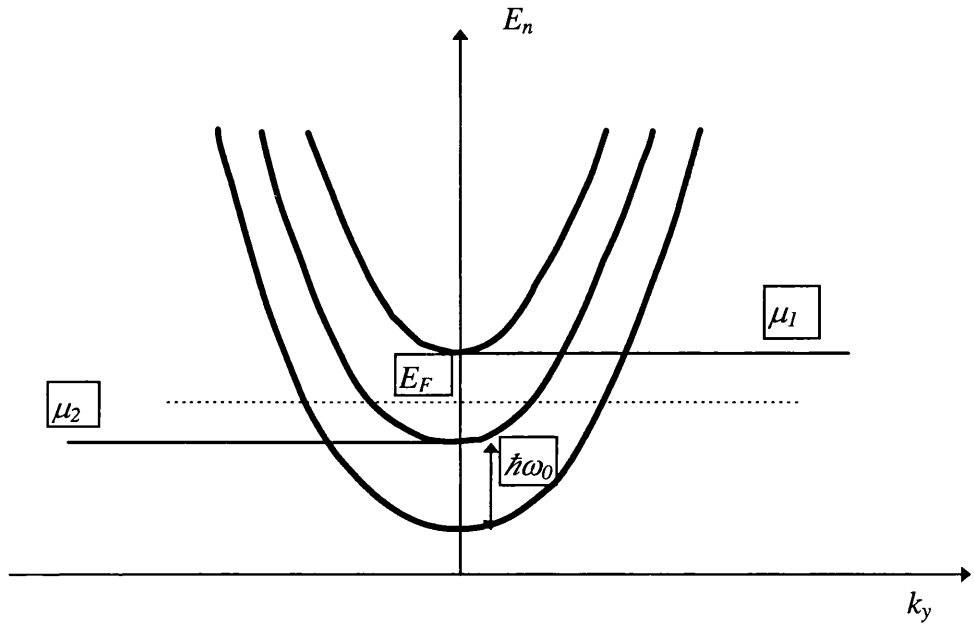

Figure 2.5: *Subband energy versus longitudinal wave vector k_y assuming a parabolic confinement potential. The 1D subbands are separated by $\hbar\omega_0$. The net current results from the uncompensated occupied electron states in the interval between μ_1 and μ_2, where μ_1 and μ_2 are the chemical potentials of the wide 2DEG reservoirs.*

A voltage difference $V=(\mu_1-\mu_2)/e$ between the two reservoirs results in a net current I, which is carried by the electron states in the energy interval between μ_1 and μ_2. The Fermi energy E_F is defined as $E_F=\mu_1=\mu_2$ when V=0. The net current at zero temperature can be written :

$$I = \sum_{n=1}^{N} \frac{2e}{h} \int_{-\infty}^{+\infty} eV \left(-\frac{\partial f(E,\mu)}{\partial E} \right) T_n(E)\, dE \tag{2.15}$$

where μ is the equilibrium potential and $f(E,\mu)$ is the Fermi function. Equation 2.15 includes the transmission probability of the n-th subband $T_n(E)$ to describe possible scattering events. N denotes the number of occupied subbands, the largest number for which $E_N(k_y = 0) < E_F$. For small voltages ($eV << E_F$), one can take $T_n(E) = T_n(E_F)$. Substituting in Equation 2.15 one finds the conductance $G = I/V = eI/(\mu_1 - \mu_2)$:

$$G = \frac{2e^2}{h} \sum_{n=1}^{N} T_n(E_F) \tag{2.16}$$

If no backscattering takes place, so $\sum_{n=1}^{N} T_n(E_F) = N$, Equation 2.16 reduces to :

$$G = \frac{2e^2}{h} N \tag{2.17}$$

demonstrating that each occupied subband contributes $2e^2/h$ to the conductance. The subbands are often referred to as 1D current channels to emphasise that each channel carries the same amount of current. The quotient e^2/h is often described as the quantum unit of conductance, with magnitude 38.7 μS=(25.8 kΩ)$^{-1}$.

Numerical calculations have shown that Equation 2.17 gives an accurate description of the conductance of a QPC with the assumptions that impurity scattering is absent and that the potential variations are smooth.

2.8 Electron transport in a Magnetic Field

In this section a discussion is presented of the dynamics of electron motion in a 2DEG, with a magnetic field applied perpendicular to the transport plane. The effect of the magnetic field on electrons confined in quasi-one dimensional channels is also considered. The main properties of edge channels and their selective transmission by QPCs is also discussed.

2.8.1 Two Dimensional Electron Gas in a Magnetic Field

In a magnetic field, perpendicular to the 2DEG in the z-direction and represented in the Landau gauge with $\underline{A}=(0,Bx,0)$, the Schrödinger equation for an electron is given by[13]

$$\left\{\frac{1}{2m^*}\left[-\hbar^2\frac{\partial^2}{\partial x^2}+\left(-i\hbar\frac{\partial}{\partial y}+eBx\right)^2-\hbar^2\frac{\partial^2}{\partial z^2}\right]+V(z)\right\}\varphi(r)=E\varphi(r) \quad (2.18)$$

where $V(z)$ is the potential confining the electrons in the 2DEG. Expanding the inner bracket gives

$$\left[-\frac{\hbar^2}{2m^*}\nabla^2-\frac{ie\hbar Bx}{m^*}\frac{\partial}{\partial y}+\frac{(eBx)^2}{2m^*}+V(z)\right]\psi(r)=E\psi(r) \quad (2.19)$$

This equation shows that two terms have arisen from the magnetic field: a parabolic magnetic potential which tends to confine the wavefunctions, and a first derivative which couples x and y and is slightly reminiscent of the Lorenz force. The method of separation of variables is used to solve Equation 2.19 in terms of functions $\phi(x,y)$ and $\phi(z)$. The resulting wavefunction is then given as the product $\phi(x,y)\phi(z)$ and the total energy will be given by $E(x,y,z)=E(x,y)+E(z)$. The vector potential does not depend on y which indicates that the wavefunction should be a

product of a plane wave along y with some unknown function along x, see Equation 2.20.

$$\phi(x,y) = u(x)e^{iky} \tag{2.20}$$

On substituting Equation 2.20 into the Schrödinger equation (2.18), the plane wave term cancels from both sides, and leaves an equation in x only

$$\left[-\frac{\hbar^2}{2m^*}\frac{\partial^2}{\partial x^2} + \frac{1}{2}m\omega_c^2\left(x + \frac{\hbar k}{eB}\right)^2\right]u(x) = \varepsilon_n u(x) \tag{2.21}$$

where ω_c is the cyclotron frequency $|eB/m^*|$ as in the classical case and ε_n are the energy eigenvalues associated with the eigenfunctions $u(x)$. Equation 2.21 is just a linear harmonic oscillator but with the vertex of the parabolic potential displaced to $-(\hbar k)/(eB)$. This equation can now be solved for the energies and wavefunctions for motion in the x-y plane, see Equations 2.22 and 2.23

$$\varepsilon_{n,k} = \left(n - \frac{1}{2}\right)\hbar\omega_c \qquad n = 1,2,3,... \tag{2.22}$$

$$\phi_{n,k}(x,y) = H_{n-1}\left(\frac{x - x_k}{l_B}\right)exp\left[-\frac{(x - x_k)^2}{2l_B^2}\right]e^{iky} \tag{2.23}$$

where $l_B = \sqrt{(\hbar/|eB|)}$ is the magnetic length and H_{n-1} are Hermite polynomials.
It can be seen from Equation 2.22 that the density of states in any two dimensional sub-band becomes a series of δ-functions referred to as Landau levels, each of which is labelled by the quantum numbers n and degenerate in wave number k.

Suppose that the system is a rectangle in the Landau gauge, of dimensions (L_x, L_y). Periodic boundary conditions along y give the usual condition[1]

$$k_y = (2\pi / L_y)j \qquad j=1,2,3,... \tag{2.24}$$

The boundary condition in the x-direction comes about because the wavefunctions are centered on x_k. Requiring x_k to be within the sample, $0<x_k<L_x$, means

$$0 < -\frac{\hbar k}{eB} < L_x \tag{2.25}$$

Thus the allowed number of states in each Landau level per unit area is given by

$$n_B = \frac{eB}{h} \tag{2.26}$$

Equation 2.26 can be rewritten by including both spins and introducing the cyclotron energy

$$2n_B = \frac{m^*}{\pi\hbar^2}\hbar\omega_c \tag{2.27}$$

Thus each Landau level (counting both spins) contains the states that originally filled the constant two-dimensional density of states over a range of $\hbar\omega_c$, the cyclotron energy, see Equation 2.3.

The number of occupied Landau levels or filling factor ν at a given field is the ratio of the total number of electrons to the number of allowed states per Landau level per unit area, see Equation 2.28

$$\nu = \frac{n_{2D}}{n_B} = \frac{h}{eB}n_{2D} \tag{2.28}$$

counting each spin separately.

In general the filling factor ν is not an integer, and at zero temperature there will be n full Landau levels where n is the integer below ν, and the top level will be partially filled. As the magnetic field increases, the energy spacing of the Landau levels increases and the density of states per Landau level increases. This

means that fewer electrons will occupy the highest level and the top level becomes empty when $\nu=n$, at a field

$$B_n = \frac{hn_{2D}}{en} \tag{2.29}$$

After this n falls by 1 and the next Landau level begins to empty. If the magnetic field lies in such a range that $n<\nu<(n+1)$ or $B_{(n+1)}<B<B_n$ there will be n completely filled Landau levels but level $n+1$ is only partly filled in which the Fermi energy resides. At the point where the $n+1$ level empties, the longitudinal resistivity falls to zero as the Fermi energy resides between Landau levels, see Figure 2.6.

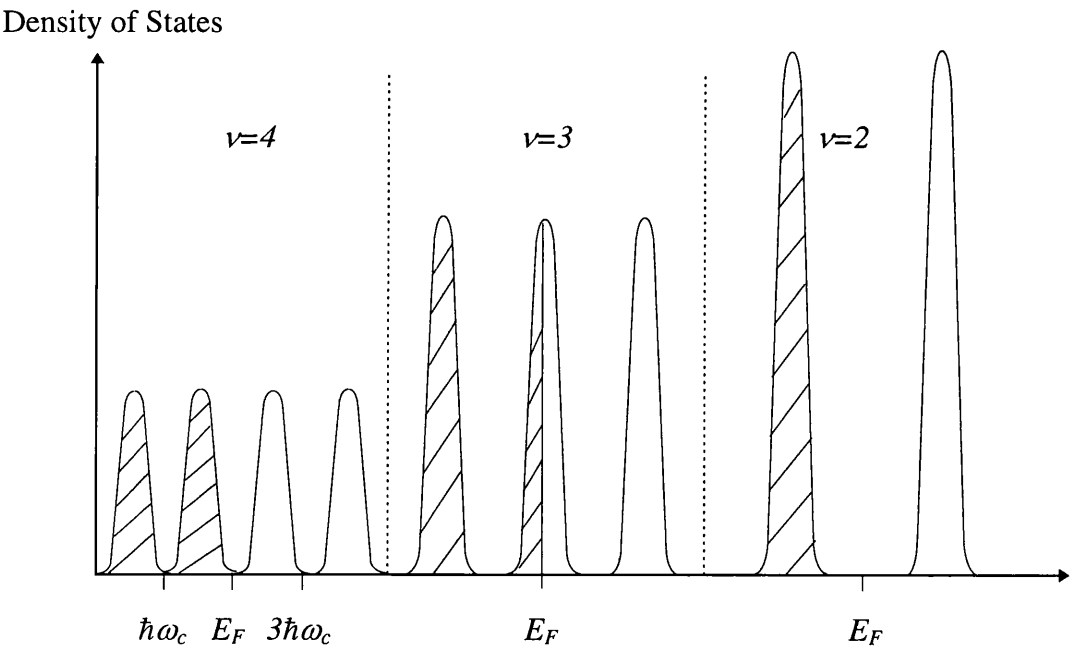

Figure 2.6: *Occupation of Landau levels in a magnetic field with its associated filling factor. The movement of the occupied Landau levels with respect to the Fermi energy is also shown*[1].

Figure 2.6 shows that the density of states at the Fermi energy changes as a function of B when spin splitting is negligible. It drops to zero when ν is integral and has maxima when ν is roughly half-way between integers. This is reflected in many quantities that depend on this density of states. The oscillations

of longitudinal resistivity with magnetic field are called the Shubnikov-de Haas effect, which can be explained using the two-dimensional resistivity tensor[5]

$$\rho = \rho_0 \begin{pmatrix} 1 & -\omega_c\tau \\ \omega_c\tau & 1 \end{pmatrix} \tag{2.30}$$

where ρ_0 is the zero field resistivity given by

$$\rho_0 = \frac{m^*}{n_{2D}e^2\tau} \tag{2.31}$$

and the scattering time τ is inversely proportional to the density of states $\rho(E_F)$ in the simple Born approximation

$$\tau^{-1} = \left(\frac{\pi}{\hbar}\right)\rho(E_F)c_i u^2 \tag{2.32}$$

where c is the areal density of impurities, and the impurity potential is modelled by a two-dimensional delta function of strength u. From these equations it can be seen that the diagonal element of the resistivity tensor is directly proportional to the density of states at the Fermi energy. Thus oscillations in the density of states at the Fermi level due to the Landau level quantization are therefore observable as an oscillatory longitudinal magnetoresistivity.

The resulting Shubnikov-De Haas oscillations are periodic in $1/B$, with spacing $\Delta(1/B)$ given by

$$\Delta\left(\frac{1}{B}\right) = \frac{e}{hn_{2D}} * 2 \tag{2.33}$$

providing a means to determine the electron density from a magnetoresistance measurement by applying Equation 2.29 at two consecutive minima, n and $n+1$, and then subtracting to eliminate n, or alternatively by plotting $1/B$ versus integer values.

2.8.2 Electron transport in Narrow Channels in a Magnetic Field

Let us apply a magnetic field to a 2DEG confined in a narrow channel with a confining potential $V(x)$. The Schrödinger equation for electrons with wavefunction $\psi(r)$ will be[1]

$$\left[-\frac{\hbar^2}{2m^*}\nabla^2 - \frac{ie\hbar Bx}{m^*}\frac{\partial}{\partial y} + \frac{(eBx)^2}{2m^*} + V(x) + V(z)\right]\psi(r) = E\psi(r) \qquad (2.34)$$

Separating Equation 2.34 to extract the x-y dependence gives

$$\left[-\frac{\hbar^2}{2m^*}\left(\frac{\partial^2}{\partial x^2} + \frac{\partial^2}{\partial y^2}\right) - \frac{ie\hbar Bx}{m^*}\frac{\partial}{\partial y} + \frac{(eBx)^2}{2m^*} + V(x)\right]\psi(x,y) = E_{xy}\psi(x,y)$$

This equation can be solved with the function

$$\phi(x,y) = u(x)e^{iky} \qquad (2.35)$$

resulting in

$$\left[-\frac{\hbar^2}{2m^*}\frac{d^2}{dx^2} + \frac{1}{2}m^*\omega_c^2\left(x + \frac{\hbar k}{eB}\right)^2 + V(x)\right]u(x) = \varepsilon_n u(x) \qquad (2.36)$$

where $\omega_c = eB/m^*$ is the cyclotron frequency. The case of a parabolic confining potential when

$$V(x) = \frac{1}{2}m^*\omega_0^2 x^2 \qquad (2.37)$$

can be solved exactly because the magnetic potential is also parabolic. The energy eigenvalues

$$\varepsilon_n = \left(n - \frac{1}{2}\right)\hbar\omega_B + \frac{\hbar^2 k^2}{2m_B} \tag{2.38}$$

where

$$\omega_B = \left(\omega_0^2 + \omega_c^2\right)^{\frac{1}{2}} \quad \text{and} \quad m_B = m\left(\frac{\omega_B}{\omega_c}\right)^2 \tag{2.39}$$

The first term in Equation 2.38 is a potential energy term associated with confinement in discrete energy levels, whereas the second term accounts for the kinetic energy of the carriers with wave vectors *k*.

It is interesting to investigate the dependence of the eigenstates in an infinitely deep square well where $V(x)=0$ for $|x|=a/2$ and $V(x)=\infty$ elsewhere, see Figure 2.7.

For zero magnetic field the energies are

$$\varepsilon_n(0) = \left(\frac{\hbar^2}{2m}\right)\left(\frac{n\pi}{a}\right)^2 + \frac{\hbar^2 k^2}{2m} \tag{2.40}$$

and when $k=0$ the magnetic potential is a parabola centered on the origin which jumps to infinity when it approaches the hard walls. A weak magnetic field raises the energy of the state and slightly distorts the wavefunction; the walls still provide the main confinement. Increasing the field, increases the magnetic potential until it provides the more effective confinement. The energy of the electrons is now confined in Landau levels which lie below the Fermi energy and thus carry no current. If the wave vector is increased, the vertex of the magnetic parabola shifts and can actually lie outside the wire. At high values of *k*, the electrons are confined at the edge of the channel in a narrow potential well created between the magnetic potential and $V(x)$. At sufficiently high values of *k*, the eigenstates lie above the Fermi energy and hence any propagation will occur at the sample edge. These states squeezed against the side by the Lorenz force, with higher energies than those in the middle of the wire, are the edge states. An

important aspect to edge transport is that states on opposite edges travel in opposite directions, which suppresses the scattering between them.

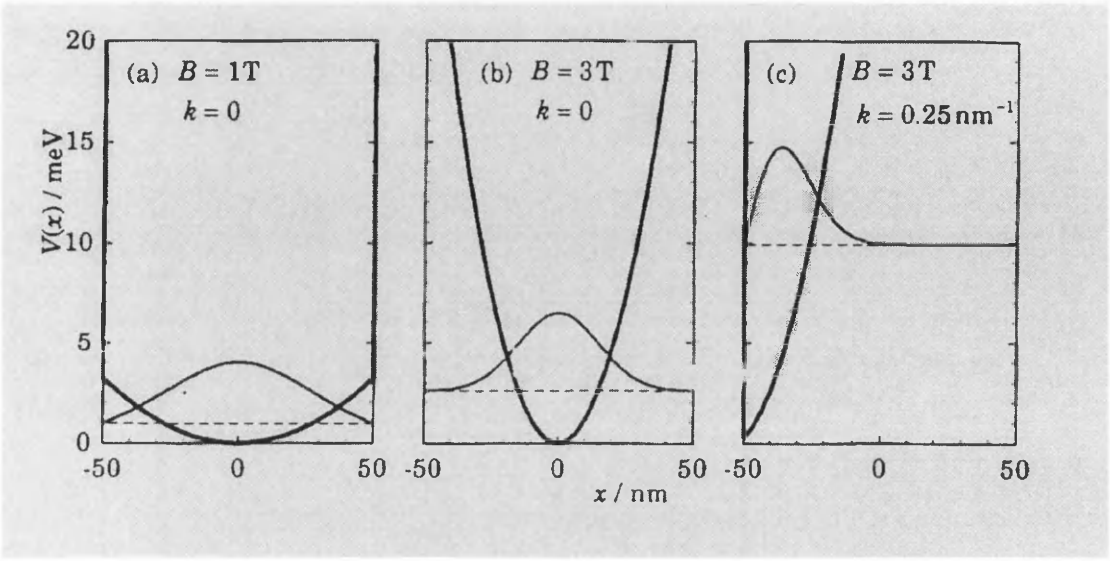

Figure 2.7: *Potential energy and lowest eigenstate in a magnetic field for an electron with wavevector k in a hard walled wire of width 0.1 μm in GaAs*[1].

2.8.3 Transmission of Edge Channels by QPCs

In the previous section edge channels were seen to originate from Landau levels, which in the bulk lie below the Fermi level but rise in energy on approaching the sample boundary. The point of intersection of the *n*th Landau level with the Fermi level forms the edge states belonging to the *n*th edge channel. The number N of edge channels at E_F is equal to the number of bulk Landau levels below E_F.

It has experimentally been shown that forward scattering between different edge channels at the sample boundary is low[14]. It means that the transport in edge channels is adiabatic, i.e. the quantum number n is conserved. Thus the edge channels can be regarded as independent one-dimensional current channels[15].

The relevant electron states for transport are only those at the Fermi energy E_F. The energy of an electron at the Fermi level in a strong magnetic field contains a part

$$\left(n-\frac{1}{2}\right)\hbar\omega_c \tag{2.41}$$

due to the quantized cyclotron motion and a part

$$\pm\frac{1}{2}g\mu_B \tag{2.42}$$

from spin splitting (depending on the spin direction).
The remainder is the energy E_G due to the electrostatic potential.

$$E_G = E_F - \left(n-\frac{1}{2}\right)\hbar\omega_c \pm \frac{1}{2}g\mu_B B \tag{2.43}$$

E_G is known as the guiding centre energy[16]. Equation 2.43 indicates that edge channels with different Landau level index n or opposite spin direction, all located at the sample boundary, follow different equipotential lines.

Using their tuneable barrier height E_B, QPCs can be used as selective edge channel transmitters. Edge channels for which $E_G<E_B$ will be reflected by a QPC and those with $E_G>E_B$ will be transmitted through the QPC. Because only the transmitted edge channels contribute towards the conductance, the two terminal conductance G of a single QPC is given by

$$G = \frac{e^2}{h}(N+T) \tag{2.44}$$

where N is a number of fully transmitted channels and T is the partial transmittance of the upper edge channel. It must be noted that the edge channel with the smallest index n has the largest guiding centre energy according to Equation 2.43.

As the barrier height E_B of the QPC changes with the gate voltage and the guiding centre energy E_G changes with the magnetic field, the number of transmitted edge channels can be changed by varying the magnetic field or the gate voltage. Experimental results show[15] that Equation 2.44 holds very well, indicating that QPCs fully transmit the lower indexed edge channels and partially transmit the upper channel without scattering between the available edge channels.

2.8.4 Electron Transport in Series QPCs in a Magnetic Field

Consider the case when two QPCs are connected in series with a dot-shaped cavity between them. In zero magnetic field the electrons will scatter randomly in the cavity establishing an isotropic velocity distribution. In this regime the series resistance is the Ohmic addition of the individual QPC resistances[17].

In high magnetic field when the electrons are confined to edge channels the above situation changes radically[18]. The electron transport is adiabatic if there is no scattering between the different edge channels. The QPC with the highest potential barrier, thus with the lowest number of transmitted channels will form the characteristic resistance for the system. The series conductance G_D is completely determined by the QPC which transmits the least number of subbands, and which consequently has the largest resistance.

$$G_D = min(G_A, G_B) \;) \tag{2.45}$$

where G_A and G_B are given by Equation 2.44 for the QPCs A and B respectively. If both QPCs transmit the same number of channels N and the upper edge channel is only partially transmitted, the conductance of the quantum dot G_D is

$$G_D = \frac{e^2}{h}(N + T_2) \tag{2.46}$$

T_2, the partial transmission of the upper edge channel through the two QPCs in series can be calculated from the individual transmission probabilities T_A and T_B of both QPCs. The incoming electron will be transmitted through both QPCs with probability $T_A\ T_B$. After making one loop around the dot, the probability for the electron to be transmitted is $T_A\ R_B\ R_A\ T_B$, where $R=1-T$. After the second loop the transmission probability will be

$$T_A\left(R_B R_A\right)^2 T_B \tag{2.47}$$

The total transmission probability will be

$$T_2 = T_A T_B\left[1+R_A R_B+\left(R_A R_B\right)^2+...\right]=\frac{T_A T_B}{1-R_A R_B} \tag{2.48}$$

Equation 2.48 gives the classical transmission probability of a single channel through two barriers.

After deriving classical transmission probability for a double barrier structure, let us give a simple quantum mechanical derivation[19]. Consider an incoming electron with a wavefunction Ψ_{in} from the partially transmitted edge channel on the left hand side. The right and left-moving waves Ψ_R and Ψ_L in the dot are mutually connected through:

$$\Psi_R = \sqrt{T_A}\Psi_{in}+\sqrt{R_A}\Psi_L \qquad \text{and} \qquad \Psi_L = \sqrt{R_B}\Psi_R\, exp(i\Theta) \tag{2.49}$$

when both are evaluated at QPC A. Θ is the acquired phase after making one revolution around the dot. If Ψ_{out} is the outcoming wavefunction at the right where

$$\Psi_{out} = \sqrt{T_B}\Psi_R \tag{2.50}$$

the transmission probability $T_2 = \left|\Psi_{out}\right|^2 / \left|\Psi_{in}\right|^2$ is given by

$$T_2 = \frac{T_A T_B}{1 - 2\sqrt{(R_A R_B)}\cos\Theta + R_A R_B} \tag{2.51}$$

The interesting quantum mechanical aspect of Equation 2.51 is that the transmission probability of two barriers in series can be larger than the transmission probabilities of the individual barriers. This is known as resonant transmission and is most apparent for equal barrier transmissions T_A=T_B when the maxima in T_2 are equal to one.

In the quantum dot the phase Θ is determined by the enclosed flux:

$$\Theta = 2\pi BA / \phi_0 \tag{2.52}$$

where A denotes the are enclosed by the edge loop and ϕ_0=h/e is the flux quantum.

Resonant transmission occurs whenever the Fermi energy E_F of the reservoirs coincides with a zero dimensional state. This regime is most apparent when the quantum dot is weakly coupled to the reservoirs. Then the eigenstates of the dot are nearly undisturbed so that resonant transmission through the discrete zero-dimensional states will give rise to sharp peaks in the conductance with a maximal amplitude of e^2/h.

References

1. J H Davies, Nanoelectronics Lectures (unpublished).

2. Y Cho and J R Arther, Prog. Solid State Chemistry Vol. 10, edited by G Somerjai and J McCaldin, Pergamon, New York, 157 (1975).

3. C Weisbuch and B Vinter, Quantum Semiconductor Structures, Academic Press, London, 39 (1991).

4. H L Stromer, R Dingle, A C Gossard, W Wiegmann, M D Sturge, Solid State Communications, 29, 705 (1979).

5. C W Beenakker and H van Houten, Solid State Physics 44, edited by H Ehrenreich and D Turnbull, Academic Press, London, 17 (1991).

6. F Stern, Appl. Phys. Lett. 43, 974 (1983).

7. A R Long, J H Davies, M Kinsler, S Vallis, M C Holland, Semicond. Sci. Technol. 8, 1581 (1993).

8. S Chakravarty, A Schmid, Physics Reports 140, 193 (1986).

9. H van Houten, C W J Beenakker, Semiconductors and Semimetals 35, edited by M Reed, Academic Press, New York, 19 (1990).

10. H van Houten, B J van Wees, J E Mooij, C W Beenakker, J G Williamson, C T Foxon, Europhys. Lett. 5, 721 (1988).

11. L I Glazman, G B Lesovick, D E Khmelnitskii, R I Shekhter, JETP Lett. 48, 238 (1988).

12. *Single Charge Tunnelling*, edited by H Grabert, J M Martinis and M H Devoret, Plenum, New York, (1991).

13.L D Landau, E M Lifshitz, Quantum Mechanics Vol. 3, Pergamon Press, (1977).

14.B J van Wees, E M Willems, L Kouwenhoven, C J Harmans, J G Williamson, C T Foxon, J J Harris, Phys. Rev. B 39, 8066 (1989).

15. B J van Wees, E M Willems, C J Harmans, C W Beenakker, H van Houten, J G Williamson, C T Foxon, J J Harris, Phys. Rev.Lett. 62, 1181 (1989).

16. *The Quantum Hall Effect*, edited by R E Prange and S M Girvin, Springer-Verlag, New York, (1987).

17. C W Beenakker and H van Houten, Phys. Rev. B 39, 10445 (1989).

18. L P Kouwenhoven, B J van Wees, W Kool, C J Harmans, A A Staring, C T Foxon, Phys. Rev B 40, 8083 (1989).

19. U Shivan, Y Imry, C Hartzstein, Phys. Rev. B 39, 1242 (1989).

Chapter 3

Device Fabrication

3.1. Introduction

In order to study the physical properties of gated heterostructures it is necessary to fabricate a device containing the two dimensional electron gas (2DEG) into which carriers can be injected and different parameters such as resistance, capacitance and depletion voltage can be measured[1]. These devices are therefore fabricated on a modulation doped GaAs-AlGaAs heterostructures in which the 2DEG is trapped 28 nm below the surface of the semiconductor. In our experiments this shallow 2DEG structure was used with an aim to increase the temperature regime in which our devices operated. We used a Hall-bar geometry to define the device which is in effect a simplified high electron mobility field effect transistor with multiple Schottky gates. The device was designed using Wavemaker, a CAD software package, and contained 4 levels. The first level is the ohmic contact level which enables us to make contact to the 2DEG. The second level is the isolation level, when the device is isolated from the rest of the semiconductor and a conducting channel is defined in the 2DEG. The third level is the gate level which defines the pattern of the Schottky gates on top of the device. The fourth layer is the wiring level which defines the pattern for connecting the gate voltage pads to the gates. After the devices have been fabricated using the combination of optical and electron-beam lithography, wet etch and metal deposition techniques, the substrate is cleaved into dies. The individual devices are attached to a single chip carrier and electrical contacts, so called bonds, are made between the ohmic contact pads of the device and the chip

carrier. In this chapter the above fabrication steps and procedures will be discussed.

(a)

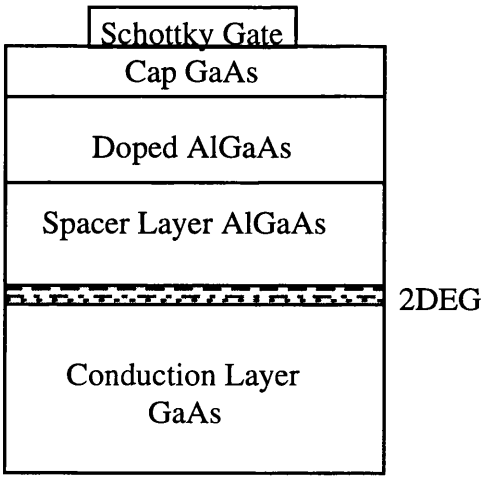

(b)

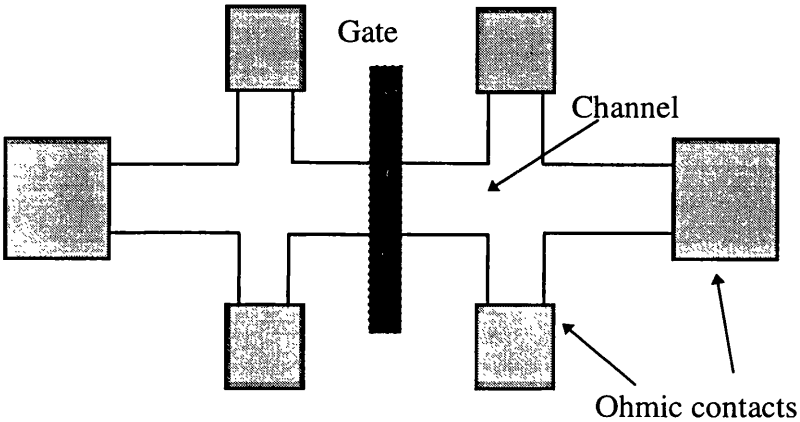

(c)

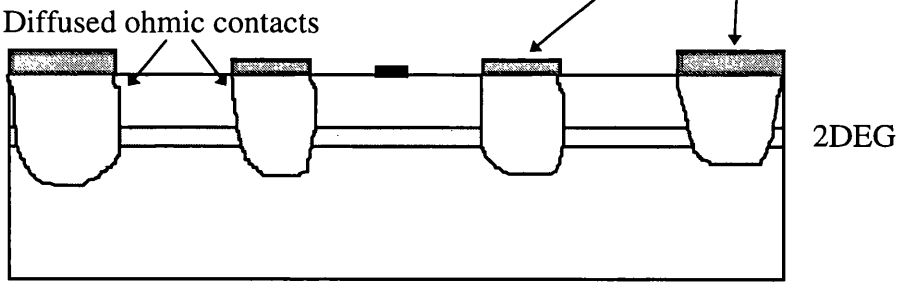

Figure 3.1: *(a) Layer structure of a modulation-doped shallow GaAs-AlGaAs heterostructure with the indication of the 2DEG (The boundary between the spacer and conduction layers is indicated with a solid line). (b) and (c) schematic layout and cross-section of the fabricated device in Hall-bar geometry.*

3.2 Principles of Optical Lithography

Optical lithography is used to define a mask pattern in a sensitive layer called photoresist deposited onto the wafer being processed. The ultimate resolution of the optical lithography system is related to the wavelength of radiation used for patterning the photoresist. For the fabrication of our devices we used a deep ultraviolet source of wavelength around 300 nm, which in principle would have enabled us to define features down to the 0.3-0.5 μm range. For patterning we used a contact lithography system, in which the photoresist-coated GaAs wafer is brought into intimate contact with a mask, which has been patterned and etched appropriately. Light from the source passes through openings in the mask to expose the photoresist. The disadvantages of this type of lithography are that the intimate mask-wafer contact often results in broken wafers and masks. Particles of photoresist can adhere to the mask, and thus frequent cleaning is required. The mask plates used in the optical lithography process were prepared by electron-beam lithography, which can prepare masks with the desired resolution. The fabrication of ohmic, isolation and wiring layers did not require resolution higher than 1 μm, and thus these layers were prepared using optical lithography. As the mask plates usually define an array of 20*20 identical device structures, a parallel device fabrication is possible which enables us to produce large number of devices. The number of faulty devices usually increases at each fabrication step, and thus large number of devices is needed to start off with in order to have a sufficient number of adequate devices left at the end of the process, for measurement.

3.2.1 Process of Optical Lithography

In optical lithography, a light sensitive polymer mixture called a photoresist, which coats the substrate to be patterned, is exposed to radiation. This radiation induces chemical changes in the resist material. The regions of the photoresist exposed to light passing through the transparent areas of the mask

plate becomes more (positive resist) or less (negative resist) soluble than the unexposed resist. The resultant differential solubility then gives rise to image formation when the resist is treated with appropriate developer used as a solvent. The developer dissolves the exposed photoresist and washes it away.

For the fabrication of our devices positive photoresist was used, which provides a higher resolution as the unexposed regions do not swell much in the developer solution. When the irradiated substrate is treated with the developer and the exposed areas of the photoresist are washed away, the patterned areas of the substrate will be exposed.

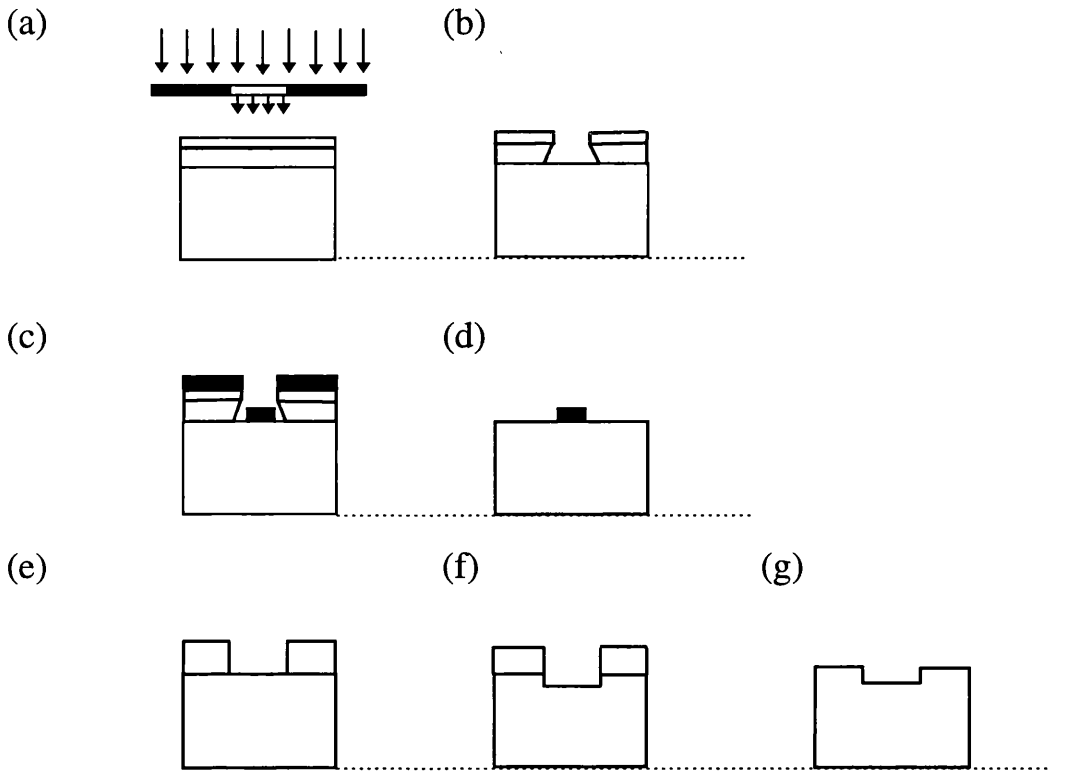

Figure 3.2: *Schematic illustration of a photolithographic process: (a) irradiation of the photoresist through the mask, (b) undercut resist profile after development, (c) sample after metal evaporation, (d) metal layer on the sample after lift-off, (e) resist profile before chemical etch, (f) sample after chemical etch, (g)etched sample after washing off the photoresist.*

Depending on the fabrication step, an oxide layer can be removed from these exposed areas of the substrate, metal layers deposited onto them, or part of the

substrate can be removed using chemical etch, see Figure 3.2. These fabrication steps will be described in the following section.

The devices are fabricated in a class 1000 cleanroom in order to ensure clean sample surfaces. In the following, the fabrication sequence used generally is explained.

3.2.1.1 Sample Cleaning

The supplied wafer is cleaved into quarter wafer pieces using a diamond tipped scriber. The quarter wafers are immersed in acetone and put in an ultrasonic bath for two minutes. To achieve the required cleanliness the quarter wafers are immersed in four different chemicals and ultrasonically agitated for five minutes in each. These chemicals are in order of use as follows:

1. Trichloroethylene

2. Methanol

3. Acetone

4. RO (Reverse Osmosis) water

The wafers are then blow dried with nitrogen gas, and put in an oven to ensure completely dry surfaces. The wafers are now ready for the application of the photoresist.

3.2.1.2 Photoresist Coating

The wafer chip is placed on the vacuum chuck of a spinner and Microposit S1400-31 photoresist is applied using a filtered syringe. The sample is then spun at 4000 rpm for 30 s to achieve a relatively uniform resist layer 1.8 μm thick. The thickness of the resist determines the thickness of the metal layer it is possible to lift-off. The wafers are then placed in an oven and prebaked for 15 minutes at 90° C, then removed from the oven and soaked in chlorobenzene for 10 minutes. The chlorobenzene hardens the upper layer of the photoresist

which becomes more resistant to the developer resulting in an undercut resist profile ensuring easier lift-off, see Figure 3.2 (b). Then the wafer chips are baked for a further 15 minutes at 90° C to remove residual solvents. The chlorobenzene soak is not required if a chemical etch step follows the development process.

3.2.1.3 Exposure of the Photoresist

To transfer the desired pattern from the mask plate to the wafers, each chip is placed onto the vacuum chuck of a System 3 High Performance Mask Aligner and Exposure System. The samples are aligned to the mask plate pattern with an accuracy of a few microns. When the alignment is completed, the samples are brought into physical contact with the mask plate and a final check is performed. The samples are then exposed through the mask plate with ultra violet light for 12 s, see Figure 3.2 (a). When the exposure procedure is completed, the samples are separated from the mask plate using a vacuum system and removed from the vacuum chuck of the mask aligner. The samples are now ready for resist development.

3.2.1.4 Resist Development

The exposed samples are immersed in the solution of one part Microposit S1400-31 developer to one part distilled water for 70 s at room temperature and gently agitated. This ensures that fresh developer continuously reaches the resist. After development the samples are rinsed in distilled water for 5 minutes to remove the remaining solution of the developer and photoresist and then blow dried with nitrogen gas.

3.2.1.5 Metallisation and Lift-off

The developed samples are put into a Plassys Automatic Metal Evaporator in which the metal layers are deposited in a high vacuum environment using electron beam. In this system, a high purity deposition is possible as the heating of the source is localised, and the source material does not react with the hearth[2].

When all the required metal layers have been deposited the samples are removed from the evaporator and immersed in acetone for one hour at 54° C. The warm acetone dissolves the remaining resist and thus removes the metal which is in contact with the photoresist, see Figure 3.2 (c) and (d). This process is known as "lift-off"[3]. After lift-off the metal layer is patterned in the pattern on the mask plate.

3.2.1.6 Wet Etch

Wet etch is used for isolating devices from each other. The etch pattern is transferred to the sample using the first four fabrication steps described above. For the fabrication of our devices we used a chemical etch step after the metallization process, thus achieving two goals: separating the devices and defining the sample geometry. GaAs is etched with an etch composition of acid, peroxide, and distilled water. This etchant works by continuously oxidising the surface and then dissolving the oxide layer. The samples are placed in a beaker containing the etch solution and gently agitated, then removed from the etch after the etching time has elapsed. After the completion of the etching process, the samples are rinsed in RO water for five minutes.

3.2.2 Electron Beam Lithography

Electron beam lithography is used for defining the gate patterns on the sample, as it gives higher resolution then optical lithography, due to the fact that electron wavelength is much smaller then the wavelength of the ultra violet light[4]. Thus the use of electron beam for patterning can result in smaller features. For the fabrication of our devices, we used optical lithography for three fabrication steps as it significantly cut the processing time, and electron beam lithography for gate patterning as only this process required very high resolution[5]. The electron beam fabrication process is very similar to that of optical lithography, but the resists used, baking times and development process are rather different. In electron beam

lithography we used a bi-layer resist to achieve the undercut profile necessary for appropriate lift-off described in the Photoresist Coating section.

3.3 Sample Fabrication

In this section the detailed descriptions of the sample fabrication processes are given, which were needed to create the appropriate samples for different experiments. The sample fabrication process involves four layers, three of which were created using optical lithography steps described in the previous section and one by electron beam lithography. These layers are aligned to each other using metal markers evaporated onto the sample surface during the first fabrication step[6]. The four layers and the complete sample is shown in Figure 3.3

3.3.1 Deoxidisation and Ohmic Contacts

To investigate the properties of heterostructures, contacts are needed through which carriers can be injected into the 2DEG. These contacts should not present a barrier to charge carrier transport in either direction and are made by doping the semiconductor surface[2,3]. The diffusing dopants decrease the width of the depletion region and electrons can tunnel through. Good ohmic contacts can be made with very high dopant concentration and low contact resistance.

The first step for fabricating reliable ohmic contacts is the removal of a thin oxide layer formed on the exposed surface of the GaAs sample. This native oxide layer is usually a few nanometers thick, thus the sample must be deoxidised in a 1:4 ratio of HCL:H_2O solution for 30 s. As shallow GaAs-AlGaAs heterostructures are very sensitive to the deoxidisation etch, since it can etch deep enough to make the electric contact to the 2DEG impossible, only a very light etch in 1:10 ratio of HCL:H_2O solution is performed on the samples prior to ohmic contact deposition.

(a) Pattern for ohmic contacts

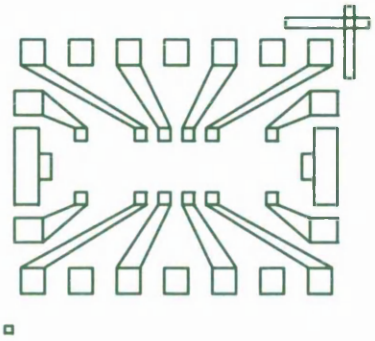

(b) Isolation layer

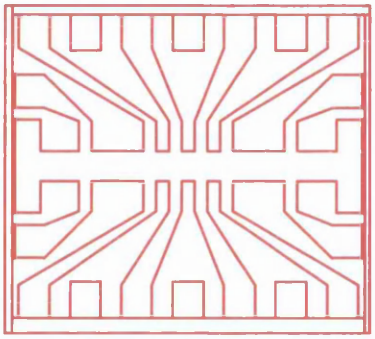

(c) Gate pattern for a quantum dot

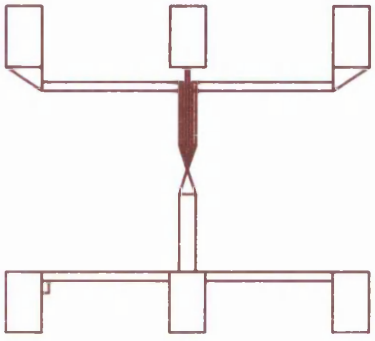

(d) Wiring level pattern

(e) Device comprising four layers

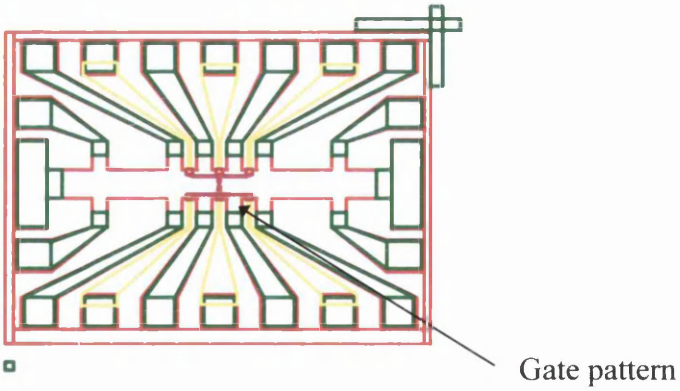

Figure 3.3: *Illustration of the data pattern for the four layers used for device fabrication : (a) Pattern for ohmic contacts, (b) Isolation, (c) Gate pattern defining a four-gated quantum dot, (d) Wiring layer, connecting the Schottky gates to the gate voltage pads, (e) Microdevice in Hall-geometry comprising four layers. The four data patterns (a),(b),(c) and (d) are not to scale, for example (c), data pattern for surface gates fills the gaps in the middle of the wiring level pattern as shown in (e).*

The ohmic contact deposition, which is in fact an artificial doping, is done in high vacuum using a Plassys Automated Deposition System operated at 10 kV which contains and deposits five materials: nickel, germanium, nichrome, gold and titanium. These materials can be deposited in any sequence with a defined thickness accurate to ± 1 nm. The predefined recipe used for creating the ohmic contacts is as follows:

1. Ni 8 nm
2. Ge 120 nm
3. Au 130 nm
4. Ni 80 nm
5. Au 250 nm.

In this recipe the Ni is used as a wetting agent to improve surface adhesion as AuGe tends to ball up; it is essential for the reliability of ohmic contacts. The 120 nm of Ge and the 130 nm of Au are included in order to diffuse into the semiconductor and form the contact. The last 250 nm of Au is used to provide a good connection to external wiring. After evaporation the contacts are annealed for 60 s at 370° C in a rapid thermal annealer flushed with argon gas, to allow the diffusion of the materials into the 2DEG and achieve low ohmic contact resistance. Then the resistance of the ohmic contacts is checked using a HP 4145 probestation. If the resistance value is too high, the samples are reannealed for a further 30 s, which affects the quality of the surface of the ohmic contacts but usually results in low contact resistance[7].

3.3.2 Isolation

The etch composition of H_2O:HCl:NH_4 mixed in a ratio 100:2:0.7 is used to isolate the conducting channel in the 2DEG. Each etch has a particular etch rate depending on the proportion of the ingredients. The above etch composition used for the isolation of our devices had an etch rate of 100 nm/minute and an

etch time of 35 s was usually used. The quality of isolation is then checked using the HP 4145 probestation, when the resistance between the ohmic contacts and the isolated gate voltage pads is measured. If this resistance value does not exceed a few MΩ, indicating inadequate isolation, the sample is immersed in the etch solution for a further 5 s and the isolation is checked again. This process is repeated until the required resistance value is achieved.

3.3.3 Fabrication of Nanostructures

As the fabrication of our nanostructures required very high resolution, electron beam lithography was used with PMMA (poly-methyl methacrylate) resists[6,7]. Two layers of PMMA called BDH (manufactured by BDH Chemicals Ltd) and Elvacite (DuPont Co.) with different average molecular weight (180000 and 360000 respectively) were used to achieve the undercut resist profile illustrated in Figure 3.2 (b). Initially the sample was cleaned as described in the section "Sample Cleaning", then a 2.5 % solution of BDH in chlorobenzene was applied to the sample and spun at 4000 rpm for 60 s. The sample was then baked at 180° C for 1 hour. The second layer of Elvacite in xylene was then applied and the sample was spun again at 8000 rpm for 60 s. After a further bake at 180° C for 1 hour, the sample was ready for exposure. Using two layers of PMMA with specific thicknesses which is determined by the density of PMMA resists and revolution at which the resist is spun ensures an undercut resist profile and reliable lift-off.

After exposure the sample was developed in a solution of 3 parts MIBK (methyl isobutyl ketone) to 1 part IPA (iso propyl alcohol). The usual development time was 35 s but this was reduced for small features when higher than average exposure dose was used. The pattern development procedure was carried out at 24±0.1° C. As the solubilities of the PMMA resists are inversely proportional to their molecular weights, the Elvacite resist gives slower development then the underlying BDH resist layer leading to an undercut resist

profile. After development the sample is rinsed in IPA for 10 s to wash off the developed resist and finally rinsed in RO water for 5 minutes.

The sample was then placed in the Plassys Automated Deposition System and 12 nm of Ti and 15 nm of Au were evaporated onto the surface. The sample was then unloaded and placed in a beaker of warm acetone for 1 hour which resulted in the lift off of the metal in contact with the resist. The lift off could be completed by splashing warm acetone onto the surface of the sample using a pipette, and removing the thin metal layer stuck to the contact pads using a sharp wooden scraper. The sample was then rinsed in cold acetone for one minute and finally in RO water for 3 minutes in order to remove the metal particles from the surface. The pattern data showing the gated region of the device and a schematic drawing depicting a four gated quantum dot is shown in Figure 3.4. A scanning electron micrograph of the gated region of the sample and a 150 nm quantum dot is shown in Figure 3.5.

3.3.4 Wiring Level

The final step in the fabrication process was the formation of the wiring level where the nanostructures were connected to the gate voltage pads, (isolated from the 2DEG). The wiring level was evaporated on top of the conducting channel of the Hall bar, partially covering the gates providing robust connection to them. The thickness of this layer is important, as the step from the etched region of the sample to the top of the channel might exceed 50 nm, and this had to be bridged. The pattern for the wiring level was defined with optical lithography. After development the sample was loaded into the evaporator and 90 nm of Ti and 60 nm of Au was evaporated onto the sample.

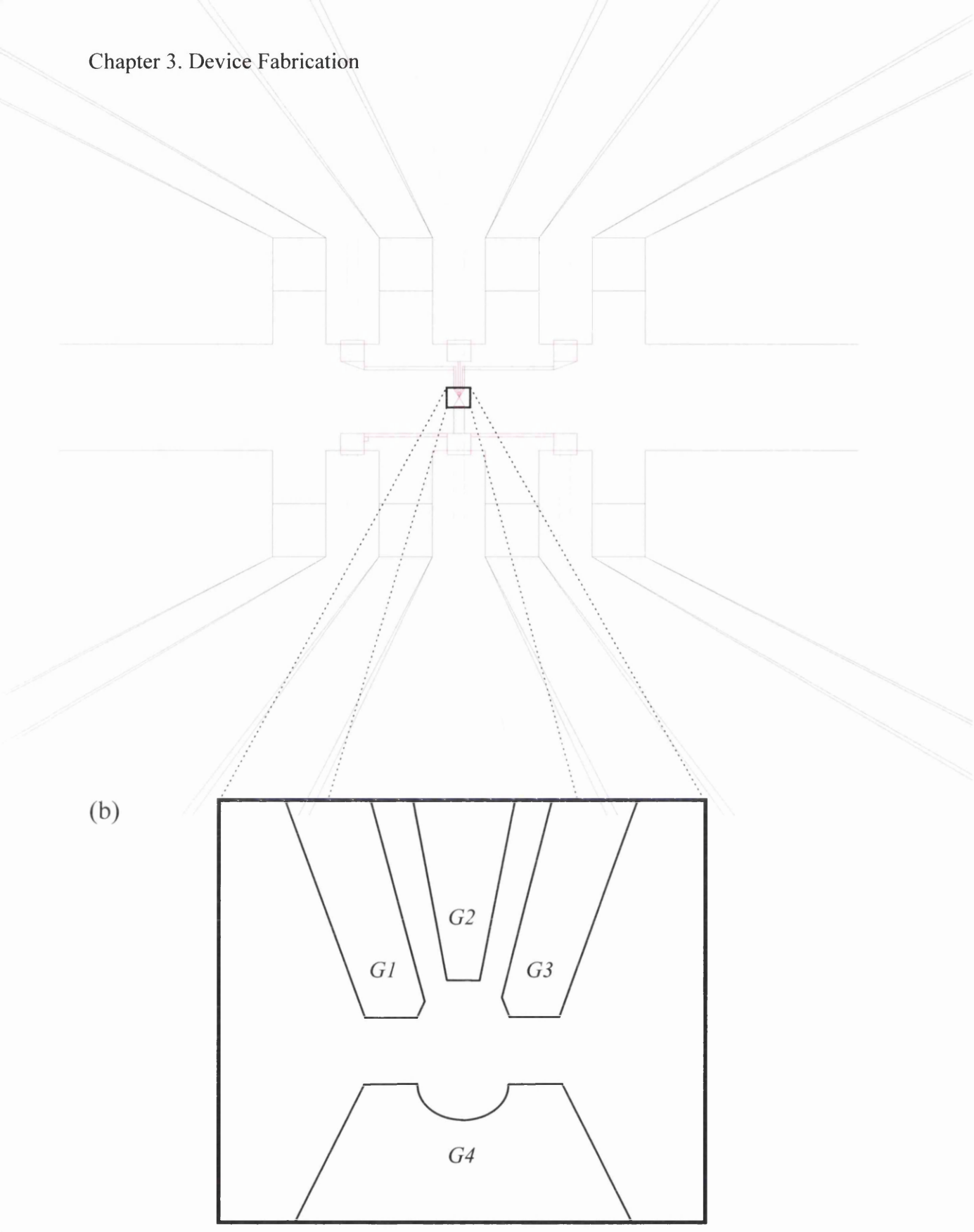

Figure 3.4 *:(a) Pattern data showing the gated region of the sample, comprising four data layers. (b) Schematic drawing depicting the gate pattern for the centre of a four gated quantum dot. The four gates are indicated by G1, G2, G3 and G4.*

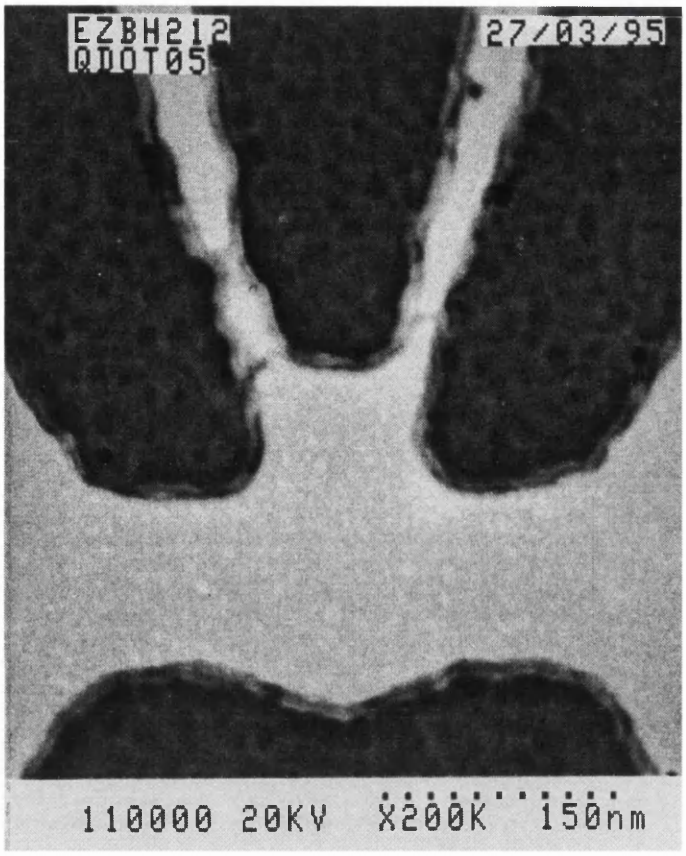

Figure 3.5 : *A scanning electron micrograph showing the gated region of a typical 150 nm quantum dot. The light region is the surface of the semiconductor heterostructure and the darker regions are the four Schottky gates. The distance of 150 nm on the micrograph is indicated by the length of the dotted line in the lower right hand corner.*

The sample were then placed in a beaker with warm acetone, and lift-off carried out, slightly agitating the sample. After washing off the excess metal with cold acetone the sample was rinsed in RO water and blow dried with nitrogen gas.

3.3.5 Sample Inspection

We used a Hitachi S900 scanning electron microscope (SEM) to evaluate the quality of the nanostructures on the fabricated chips. Usually two devices were selected from each wafer and the quality of the whole batch was evaluated from these. The selected devices were mounted in the chamber of a Hitachi S900

SEM and high resolution micrographs were taken from the devices using 20 KeV acceleration voltage. The S900 high resolution micrographs enabled us to select the desired exposure dose for electron beam lithography patterning and to significantly reduce the device preparation and measurement cycle by inspecting the fabricated nanostructures to assess their suitability for further processing.

3.3.6 Sample Bonding

Sample bonding was used to connect the samples to be measured to the environment. Each sample was glued to a chip carrier and connected to it using an ultrasonic deep access wedge bonder. The samples were mounted on a sample holder and connections were made between the gold pads of the chip carrier and the ohmic contact and gate pads of the sample using a 1.5 μm thick gold wire. After the connections were made the samples were stored in a conducting plastic container, ready for measurement.

3.4 Electron Beam Lithography

To define the gate patterns for the fabrication of quantum dots, electron beam lithography was carried out using a Philips Beamwriter EBPG-5 system, with an accelerator voltage of 100 kV. This system uses a vector scan with a Gaussian beam to transfer the patterns onto the substrate. The pattern was generated using the computer aided design software packages Wavemaker and CATS. E-beam lithography was especially suitable for the fabrication of our devices which required frequent modifications.

3.4.1 Electron Beam Writing

The pattern to be exposed on the resist takes the form of CAD data base describing polygons, their locations within dies, and the locations of dies on a wafer. This compact representation is then expanded into a specific database in which the polygons are fractured into figures whose size and type conform to standards. The pattern is written onto the substrate using a focused electron beam with a variable diameter of 12 to 400 nm. For the fabrication of our devices we used an electron beam with a diameter of 12 nm.

The exposure dose has to be carefully chosen for electron beam lithography, as its value must be high enough to change the solubility of the resist to enable the pattern to develop out. To fabricate our quantum devices an exposure dose in a range between 800-1200 $\mu C/cm^2$ was used. If the exposure dose is too high it might result in a proximity effect .

3.4.1.1 Proximity Effect

The proximity effect means that there is a tendency for adjacent features to influence each other's dose distribution. Electrons incident on the sample can be backscattered from the substrate, returning up through the resist at high energy and scattered through wide angles. They can pass upwards through the resist up to several microns from their point of entry and expose adjacent features. The proximity effect can be overcome by using electrons with higher energy. These electrons penetrate deeper into the substrate and as a result of this there are less backscattered electrons in the region of exposure. To find the best exposure dose for a given feature and minimise the proximity effect, exposure tests were carried out during the fabrication process.

3.4.1.2 Exposure Test

When fabricating small features such as quantum devices, it is necessary to find the ideal exposure dose in order to achieve the correct resist solubility for

development and to avoid proximity effects. To find the optimal exposure dose for a specific nanostructure, test patterns known as exposure tests are written. The pattern is written with a particular exposure dose then the dose is changed by a small fraction and the pattern is written again. This process is repeated until a pre-defined exposure dose range is covered. The substrate is then processed and the test patterns are inspected by SEM. When the optimal exposure dose is found the patterns can be transferred to the actual heterostructure with that particular exposure dose. This process is called registration.

3.4.1.3 Registration

When the optimal exposure has been found the pattern can be written on the heterostructure with numerous Hall-bar structures on it. The pattern has to be written in certain locations i.e. on top of each Hall-bar. To achieve this a registration procedure is used. To find the particular locations there is one pre-defined rectangle at each Hall-bar which has to be found by the electron beam writer. These rectangles or markers are used to define a co-ordinate system that allows the machine to move the sample and position the electron beam. The electron beam is positioned and the pattern is written relative to these markers.

References

1. R A Stradling and P C Klipstein, *Growth and Characterisation of Semiconductors*, Adam Hilger, Bristol, 1990.

2. E H Rhoderick and R H Williams, *Metal-Semiconductor Contacts*, Oxford University Press, Oxford, 1988.

3. H K Henisch, *Semiconductor Contacts*, Clarendon Press, Oxford,1984.

4. K A Valiev, *The Physics of Submicron Lithography*, Plenum Press, New York, 1992.

5. W B Glendinning and J N Helbert, *Handbook of VLSI Microlithography*, Noyes Publications, Park Ridge,1991.

6. R Cuscó-Cornet, PhD. Thesis, Glasgow, 1994.

7. C Barton, PhD. Thesis, Glasgow, 1995.

Chapter 4

Experimental Techniques

4.1 Introduction

In this chapter the experimental equipment and the specific measurement techniques used for the investigation of the nanostructures are described. The various cryogenic systems are covered together with the types of measurements that were carried out using these facilities. The improvements made to the pre-existing measurement system for high-impedance measurements are discussed. Finally the handling techniques for small, Schottky gated nanostructures and the damage caused by electrostatic discharge in them are also described.

4.2 Cryogenic Equipment

The experimental study of electron transport in a 2DEG may require low temperatures. An Oxford Instruments He^4 cryostat and superconducting magnet was the basic system for low temperature measurements that were carried out during the course of our project. In this system the superconducting magnet was immersed in a bath of liquid He^4 at 4.2 K and was capable of supplying fields up to 13 T. Higher fields could be achieved by pumping the main bath, thus reducing the temperature of the He^4 to 2.2 K. To attain a magnetic field greater then 11 T the magnet is fitted with inner coil sections of niobium tin. The magnetic field is produced using an Oxford PS120-10 (120 A, 10 V, forward or reverse direction) power supply which was usually computer controlled via an RS232 interface.

A 0.3 T/m sweep rate was used to measure the resistance as a function of magnetic field. The sample is placed in the centre of the magnet, perpendicular to the magnetic field in either the dilution refrigerator or variable temperature insert.

4.2.1 Dilution Refrigerator Insert

For measurements carried out below 1.2 K, an Oxford Instruments Kelvinox He^3/He^4 dilution refrigerator was used. The dilution refrigerator uses the peculiar low-temperature behaviour of the liquid He^3-He^4 mixture[1]. When the mixture of the two isotopes of helium is taken below 0.86 K, it will separate into a He^3-rich, concentrated phase floating on top of a dilute, He^4 rich phase. As the vapour pressure of He^3 is much larger than that of He^4, by pumping on the diluted phase He^3 can be removed from the solution. To maintain the equilibrium concentration, it will be replaced by He^3, crossing the boundary from the concentrated phase. This absorbs the heat of dilution of He^3 at the phase boundary. Thus by removing He^3 from the diluted solution the sample can be kept cool at temperatures below 100 mK. The He^3 removed from the diluted phase is then liquefied and pumped back to the concentrated phase. The minimum temperature achieved with the dilution refrigerator was 40 mK. The temperature is monitored using a calibrated ruthenium-oxide resistor.

4.2.2 Variable Temperature Insert

The variable temperature insert was an Oxford Instruments VTI, which allowed control and measurement of the temperature[2] in the sample space between 1.2 K and 100 K. The liquid helium was supplied to the VTI from the main bath in the cryostat via a pick up tube, see Figure 4.1. The flow of helium was controlled by a needle valve located on the VTI top plate, by creating a pressure difference between the helium in the main bath and the helium return line from

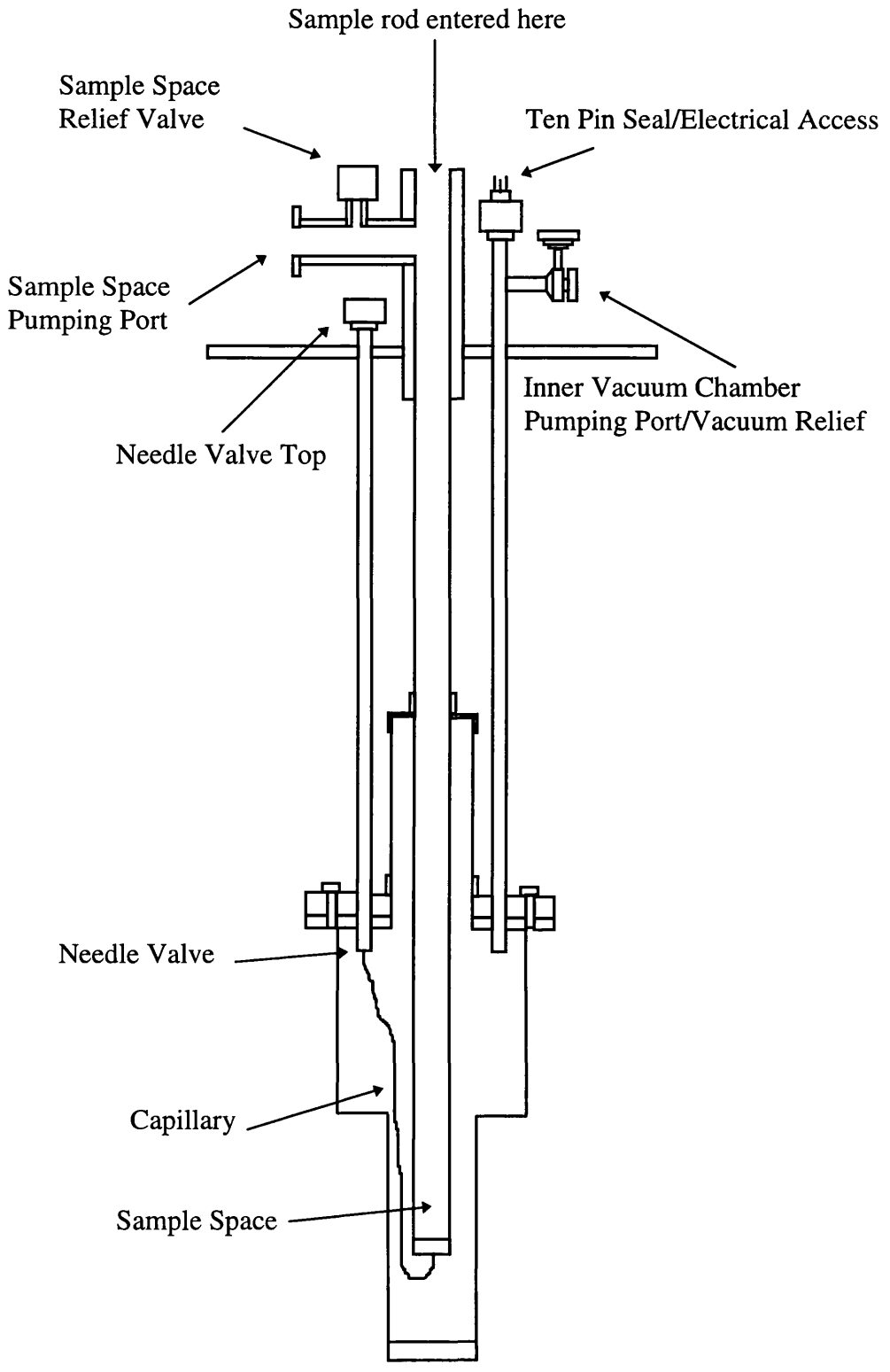

Figure 4.1: *Schematic diagram of an Oxford Instruments Variable Temperature Insert.*

the VTI. The temperature of liquid helium was controlled by passing it through a heat exchanger at the base of the VTI. Temperatures below 4.2 K could be set by reducing the vapour pressure of the helium after it had passed through the needle valve. By changing the pressure in the sample space using a rotary pump connected to the helium return line, temperatures between 1.2 K and 4.2 K could be easily achieved. The lowest temperature of 1.2 K could be set by slightly opening the needle valve and pumping the helium return line. For temperatures above 4.2 K control was achieved by setting the flow rate using the needle valve and by regulating the power to the heat exchanger heater[3]. The temperature of the sample was raised above 4.2 K by evaporating the incoming liquid to form warm helium flowing through the sample space. The sample temperature is measured using a Rh-Fe thermometer which was in thermal contact with the sample.

4.3 Sample Handling and Mounting

The samples are fairly easily damaged during the fabrication and measurement processes and the main hazard is the damage caused by electrostatic discharge[4]. Semiconductor devices with insulating gate electrodes are the most sensitive types to this form of damage. The small distance between the gate electrodes (typically 20-30 nm) in our devices measured in the course of the project made them extremely vulnerable to electrostatic discharge effects[5]. The devices had to be protected after they had been bonded to the chip carrier. The assembly of the device, bonder and bonder operator were connected to a common ground using an earthing cable and wrist strap. The earthing straps had a resistance of 2 MΩ, which was sufficient to conduct static charge safely to earth, but high enough to limit current flow in case of an electrical fault. The bonded device had to be handled using earthing straps and transported in electrostatically conductive plastic box. Even with proper precautions the discharge of possibly several hundred volts of static electricity can occur during the handling of surface gated nanostructures. The effect of electrostatic discharge in a surface gated quantum dot is shown in Figure 4.2.

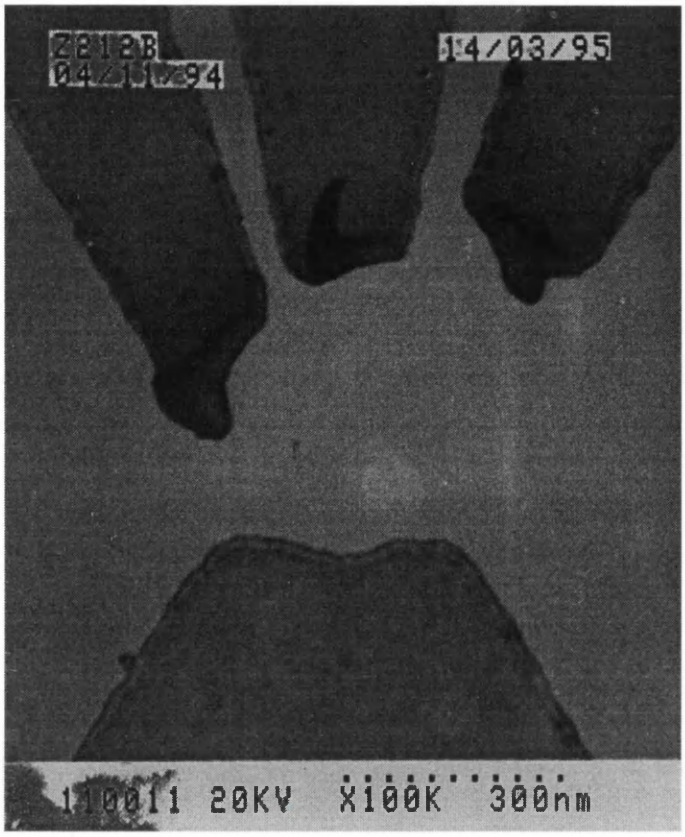

Figure 4.2: *Scanning electron micrograph of a surface gated quantum dot damaged by electrostatic discharge effect. The dark areas are the tips of the Schottky gates separated from the surface of the semiconductor.*

The bonded samples were glued to the base of a standard 18 contact ceramic chip carriers which fitted into a socket located at the bottom end of the fridge insert or the VTI. The measurement leads were connected to the pins in the socket, which are in contact with the gold pads on the bottom of the chip carrier[6]. The contact pads of the device were connected to the ceramic chip carrier with 40 μm gold wire using an ultrasonic deep access wedge bonder. Thermal contact between the sample and the mixing chamber was ensured using a spring loaded copper cylinder which was in contact with the chip carrier when it was mounted into place. To avoid the damage to the sample caused by electrostatic discharge effects, during the sample mounting procedure the assembly of the socket, sample handling tweezers, sample box and personnel were securely connected to a common ground.

A box of switches at the head of the cryostat allows each of the sample leads to be grounded so that when loading or unloading the sample all its contacts can be safely kept earthed.

4.4 AC Lock-In Measurement Technique

The general AC low frequency lock-in measurement set-up is shown in Figure 4.3. A low frequency signal (18 Hz) with a typical amplitude of 100 mV is supplied to a resistor circuit using an external oscillator, which is connected to the reference signal input of two lock-in amplifiers. The resistance circuit is a voltage divider which is set to attenuate the signal by a factor of 1000. A roughly constant signal is supplied to the device through a 10 kΩ resistor in series with the sample. The voltage across the 10 kΩ resistor is amplified using an EG&G voltage preamplifier which is connected to a Princeton 5210 dual phase lock-in amplifier. A lock-in amplifier measures the sample response to a low frequency ac signal in a very narrow bandwidth centered on the frequency of the external oscillator providing the excitation voltage for the measurements. Two lock-in amplifiers are used in order to improve the accuracy of the measurements. The voltage drop across the sample is picked up and amplified using the second EG&G PARC voltage preamplifier the output of which is connected to the second lock-in amplifier which amplifies, filters and synchronously detects the signal using the reference signal with the pre-set reference frequency. The signal in the lock-in amplifier is applied to a phase sensitive detector (PSD), which gives an oscillatory response to frequencies different from the reference frequency. These frequencies are very effectively attenuated by an internal low pass filter. The output of the phase sensitive detector is thus linear in the signal amplitude at the pre-set frequency. Then the resistance of the device can easily be calculated by using the output signals of the two lock-in amplifiers and the pre-set attenuation ratio[7].

To improve further the signal to noise ratio and measure the devices in the high-impedance regime the measurement set up was modified and a current

preamplifier was used (model SR570), providing better phase accuracy in the presence of stray capacitance. The current preamplifier which was connected in place of the series 10 kΩ resistor could measure current close to the virtual null, what enabled us to carry out low noise conductance measurements in the 25-30 MΩ impedance range.

To measure the conductance of the sample as a function of gate voltage we used the experimental set-up described above, with the gate voltages supplied

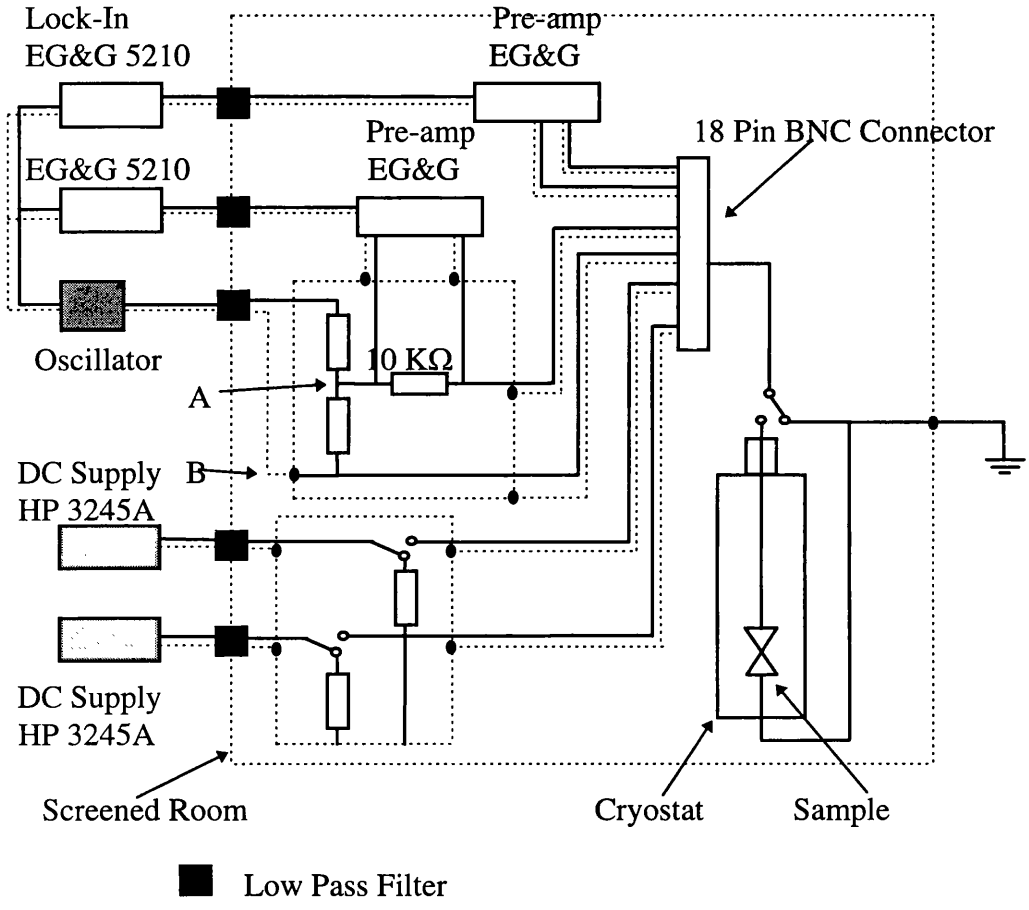

Figure 4.3: *Schematic diagram of the measuring system. The cryostat with the sample is located in the screened room to minimise RF noise. The voltage preamplifiers are placed close to the cryostat head in order to reduce the pick-up noise.*

by a Hewlett Packard 3245A Dual Universal Voltage Source. The experimental equipment was controlled with an IBM PS/2 personal computer via IEEE488 interfaces using a Turbo-Pascal program.

To carry out the measurement the sample was manually connected and an excitation voltage applied. The gate voltages were changed by the computer controlled voltage sources, and after a pre-set delay the values of the lock-in amplifiers were read and then the resistance of the device was calculated. The resistance values as a function of gate voltage was plotted on the screen and simultaneously recorded in the memory of the personal computer.

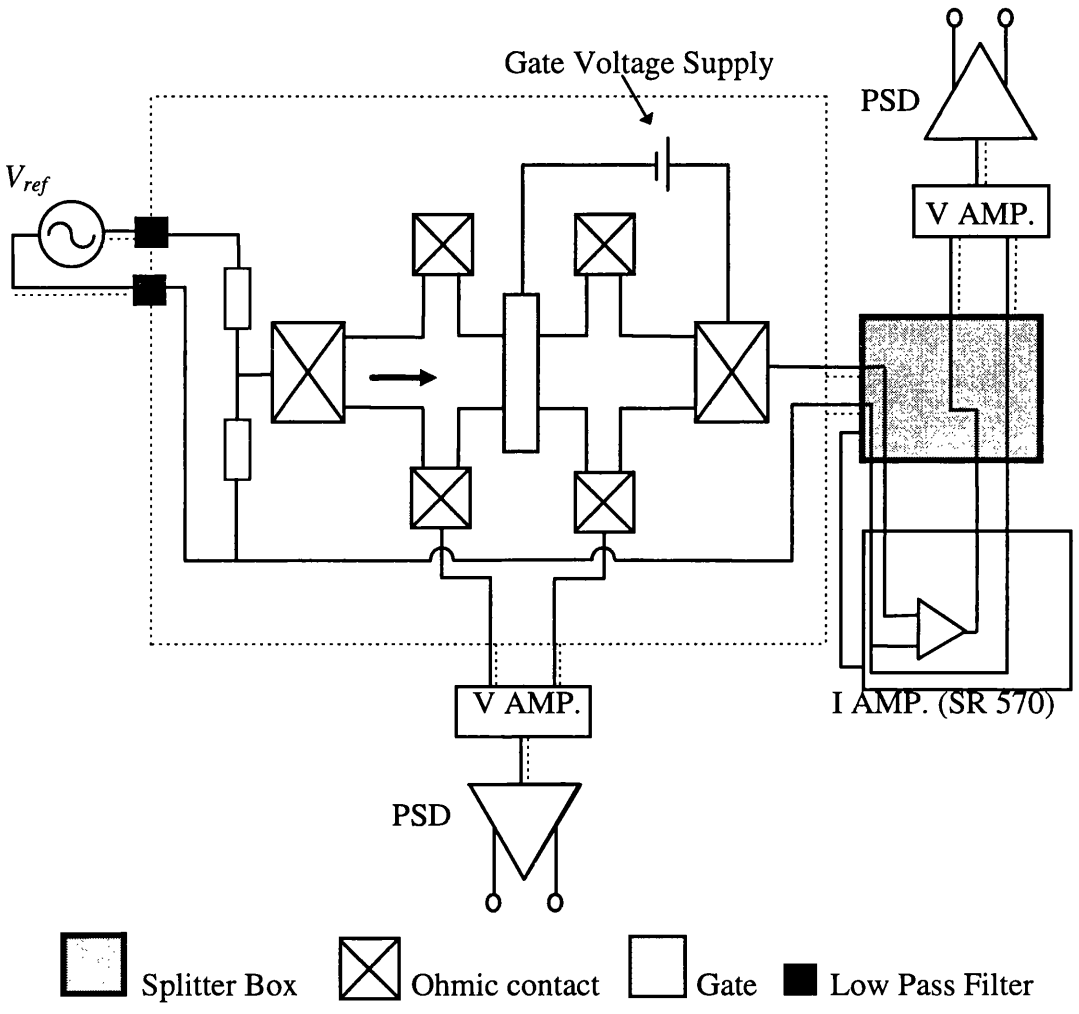

Figure 4.4: *Schematic diagram showing the improved low frequency conductance measurement set up with a current preamplifier working with a noise level of 20 fA.*

The schematic diagram of the measurement configuration used in low frequency conductance measurements is shown in Figure 4.4. This set-up with a current preamplifier in place of a series resistance allowed us to carry out low

noise conductance measurements. The attenuated signal provided by the external oscillator is passed through the sample via the current contacts and amplified by the current preamplifier in series with the sample. The voltage drop across the gated region of the sample is amplified by the EG&G voltage preamplifier. The outputs of both the voltage and current preamplifiers are connected to the two lock-in amplifiers.

In measurements using the upgraded measurement system with the current preamplifier the noise floor was typically around 10^{-4} e^2/h, while using the voltage preamplifier the noise floor was around 10^{-3} e^2/h. The upgraded system proved to be very useful in measurements at a very low sample conductance level, when the amplitude of the conductance oscillations is just above the noise floor.

The measurement configuration shown in Figure 4.4 was used as a standard set-up in the measurements described below.

To carry out a temperature dependence measurement the temperature of the sample was kept constant by fine tuning the flow rate using the needle valve, and adjusting the heating power of a LakeShore temperature controller. This way the temperature of the sample could be controlled with an accuracy of ±0.1 K between 1.2 K and 4 K, and maintained for about 40 minutes which allowed us to perform the required number of gate voltage sweeps at a certain temperature. For measurements above 4 K, longer periods were required for the temperature of the sample to settle.

In the DC source-drain bias measurement a DC excitation voltage is superimposed on the AC excitation voltage provided by the external oscillator. The DC bias is supplied by a third Hewlett Packard 3245A Universal Voltage Source in a range of ±11 V. and applied between the points A and B shown in Figure 4.3, which results in the division of the signal by a factor of 1000. Thus the sample could be biased with a DC signal between ±11 mV. The source-drain bias to the sample could be reversed by interchanging the source and drain contacts in order to check the electrical symmetry of the quantum dots in the DC source-drain measurements.

The experimental system is located inside a screened room as shown in Figure 4.3. The measurement signals are carried by twisted coaxial cables into and out of the screened room, passing through low-pass filters mounted on the

outside wall of the screened room. The signal filtering and the screened room are necessary to minimise the level of unwanted RF signals which can easily result in significant electron heating in the sample.

Mechanical vibrations were reduced by removing the pumps from the screened room, damping the pumping lines connected to the cryostat with lead foam and putting the cryostat on a damping mat.

Special care was taken to electrically isolate the cryostat from its environment and then earth it together with the equipment at a single point. This helped prevent the formation of earth loops in the system.

References

1. D S Betts, *An Introduction to Millikelvin Technology*, Cambridge University Press, Cambridge,1989.

2. A Kent, *Experimental Low-Temperature Physics*, Macmillan Physical Science Series, 1993.

3. R C Richardson and E N Smith, *Frontiers in Physics: Experimental Techniques in Condensed Matter Physics at Low Temperatures*, Addison-Wesley Publishing Company, Inc, 1988.

4. C E Jowett, *Electrostatics in the Electronics Environment*, The Macmillan Press Ltd, 1976.

5. S J Sangwine , *Electronic Components and Technology*, Chapman & Hall, 1994.

6. R Cusco-Cornet, PhD. Thesis, Glasgow, 1994.

7. C Barton, PhD Thesis, Glasgow, 1995

Chapter 5

Charging Effects in Quantum Dots

5.1 Introduction

Single-electron charging effects were first studied in granular films and metal tunnel junctions[1]. Periodic conductance oscillations were first observed in disordered wires[2] which were interpreted in terms of electron confinement between impurity barriers. In later experiments on lateral quantum dots[3] controllable potential barriers were used which allowed the number of electrons in the device to be changed one-by-one. This change in number of electrons in the dot results in periodic oscillations which were explained in terms of charging effects. More recent theoretical work and measurements were carried out on quantum transport in a magnetic field[4,5]. With advancing fabrication technology it became possible to scale down[6] the semiconductor nanostructures to a region where electron-electron interactions have a significant effect on transport properties. These artificially fabricated nanostructures, which contain only few electrons, have proven to be excellent devices to study quantum size effects. Different experiments, analysis and techniques are reviewed in Ref. 7.

In this chapter we present the working principles of lateral split-gate quantum dots which we illustrate with the properties of our own devices. We discuss the charging theory for semiconductor quantum dots and explain the origin of Coulomb-blockade oscillations. We review the optimisation procedure for quantum dots with regard to energy level spacing inside the dot. The model for electrostatic potential and electron distribution in the measured surface gated

quantum dots is discussed. The results of calculations estimating the number of electrons in the smallest surface gated quantum dots are also presented.

5.1.1 Theory of Single Electron Charging Effects[11]

Single electron charging effects[8-10] can strongly affect the transport properties of semiconductor nanostructures weakly coupled to the electron reservoirs by tunnel barriers. The tunnel barriers can be made controllable[11] using metal gates deposited on the surface of the GaAs-AlGaAs heterostructures. To create a double tunnel barrier[12] the metal gates are formed into two QPCs with a cavity between them. Thus a simple but entirely controllable quantum dot can be formed using four Schottky gates (*G1,G2,G3,* and *G4*) on the surface of the substrate, as in Figure 5.1a. By changing the potential on the centre gate electrode, the number of electrons in the electron pool between the tunnel barriers can be changed one by one. This change in electron numbers in the dot seen as conductance oscillations through the quantum dot.

Figure 5.1a shows the schematic layout of a four gate quantum dot, Figure 5.1b schematically shows the potential landscape of the quantum dot, which is created in the 2DEG by the four metal gates. Figure 5.1c shows the equivalent circuit. The electrons will be strongly confined in the dot by the induced potential barriers, if sufficiently large negative voltages are applied to the QPCs. The number of electrons in the quantum dot is an integer and can be changed by an integer number. We can write the electrostatic energy E_{ee} of the dot in the form[11]:

$$E_{ee} = \frac{(-en + Q_0)^2}{2C} \quad \text{where} \quad \begin{aligned} n &= N - N_0 \\ Q_0 &= C_S V_S + C_D V_D + \sum C_g V_g \\ C &= C_S + C_D + \sum C_g \end{aligned} \qquad (5.1)$$

where C_S, C_D and C_g are the capacitances between the source, drain, gates and the electron pool forming the quantum dot. The excess charge in the dot is

$en=e(N-N_0)$, where N is the number of electrons in the quantum dot, and the charge of the electron is taken positive. N_0 is the number of 'residual' electrons in the dot at zero gate voltage and zero bias voltage. When negative voltage is applied to the gates the region beneath them is depleted, which decreases the number of electrons in the pool (thus $N_0 > N$).

(a)

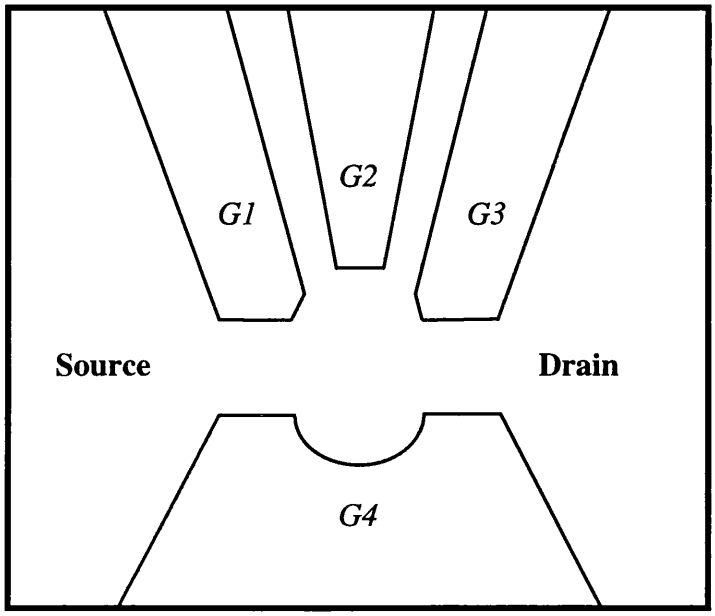

(b)

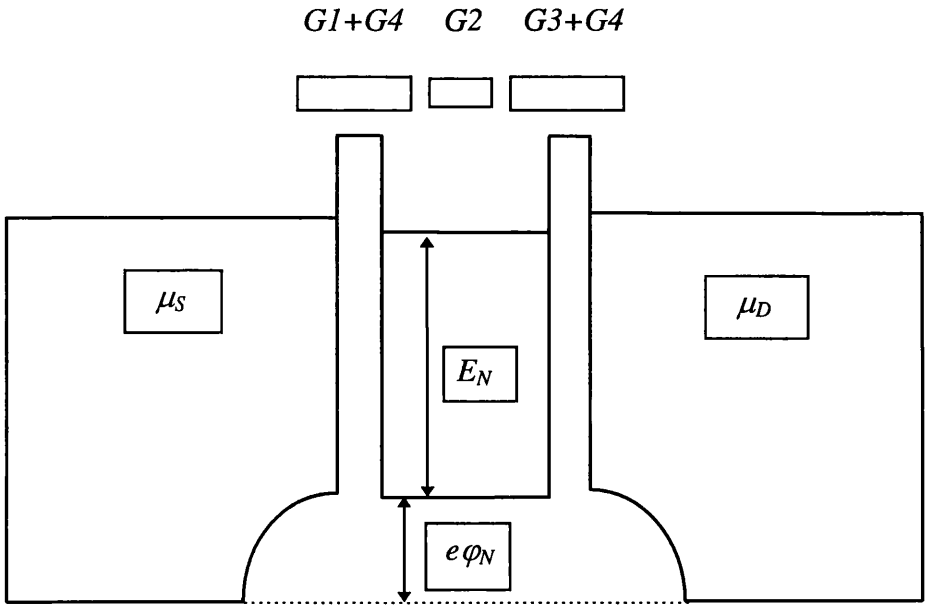

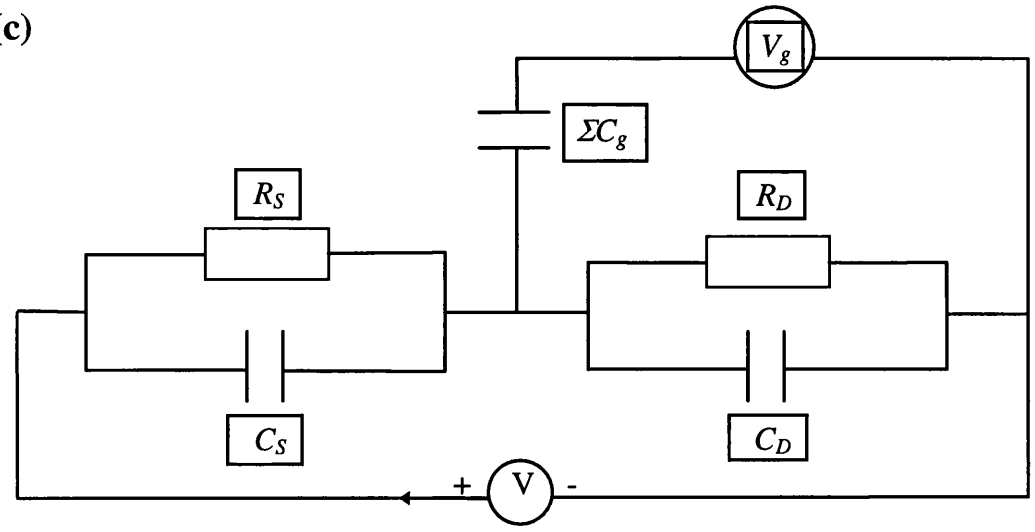

Figure 5.1: *(a) General schematic plan view of a surface gated quantum dot measured during the course of the project. The Schottky gates are indicated by G1, G2, G3 and G4. (b) Potential landscape of the quantum dot in the 2DEG created by the gates G1, G2, G3 and G4.* μ_S *and* μ_D *are the chemical potentials of the 2DEG reservoirs (source and drain respectively).* φ_N *is the electrostatic potential with N electrons in the quantum dot.* E_N *is the energy level of the Nth electron in the dot, relative to the bottom of the conduction band. (c) Equivalent circuit of (b), using two voltage sources.*

Q_0 is the continuous part of the excess charge, which is induced by voltage differences V_S and V_D between the dot and the leads ($eV_S=\mu_S-\mu_d(N)$, $eV_D=\mu_d(N)-\mu_D$, where $\mu_d(N)$ is the electro-chemical potential of the quantum dot), and by the gate voltages. C represents the total capacitance of the dot to ground, which comprises the capacitances C_S and C_D between the dot and the source and drain respectively and the sum of the capacitances ΣC_g between the dot and the gates. For n=1 and Q_0=0 Equation 5.1 gives the charging energy $e^2/2C$ for a single electron. It is more convenient to take $E_C=e^2/C$ as a unit for charging energy.

Generally the conductance of the device is measured with a small bias voltage $V=(\mu_S-\mu_D)/e$ across the dot, as the voltage applied to one of the gates is changed. Therefore we simplify $Q_0=C_gV_g$, where V_g denotes the gate voltage which is varied, and C_g the capacitance between this gate and the dot. The ground state energy for N electrons in the quantum dot is the sum over the single particle

energies E_p relative to the bottom of the conduction band. In this case the electrostatic energy can be written:

$$U(N) = \sum_{p=1}^{N} E_p + \frac{(-en + C_g V_g)^2}{2C} \tag{5.2}$$

From Equation 5.2 we can calculate the electro-chemical potential which is the minimum energy necessary to add the *Nth* electron to the dot

$$\mu_d(N) = U(N) - U(N-1),$$

$$\mu_d(N) = E_N + \frac{(n-1/2)e^2}{C} - e\frac{C_g}{C}V_g \tag{5.3}$$

When the number of electrons is changed by one at constant gate voltage, the change in electro-chemical potential can be written as

$$\mu_d(N+1) - \mu_d(N) = E_{N+1} - E_N + \frac{e^2}{C} \tag{5.4}$$

Equation 5.4 indicates that the electro-chemical potential changes by a finite energy when an electron is added to the dot. $\mu_d(N+1)$-$\mu_d(N)$ is large for large energy splitting between consecutive 0D-states and if the capacitance of the dot is small. This energy can result in blockading for tunnelling of electrons into and out of the dot as depicted in Figure 5.2a, where N electrons are confined in the dot. The *(N+1)th* electron cannot tunnel into the dot, because the resulting electro-chemical potential $\mu_d(N+1)$ would be higher than the electro-chemical potentials of the source and drain. For $\mu_d(N)<\mu_S$, $\mu_D<\mu_d(N+1)$ the electron transport is blocked. This regime is known as the *Coulomb blockade.* Electron transport is only possible by thermal activation or tunnelling via virtual states[13]. The energy gap of Equation 5.4 is found at the Fermi energy, and determines the transport properties and the activation energy. The zero dimensional states below $\mu_d(N)$ are separated by E_N -E_{N-1}.

It is possible to remove the Coulomb blockade by changing the gate voltage so that $\mu_d(N+1)$ is lined up between μ_S and $\mu_D(\mu_S>\mu_d(N+1)>\mu_D)$ as depicted in Figure 5.2b. An electron can tunnel from the source into the dot $(\mu_S>\mu_d(N+1))$. The electro-chemical potential in the dot increases by the amount given by Equation 5.4, which is dominated by the increase in electro static potential $e\varphi_{N-1}-e\varphi_N=e^2/C$. Because $\mu_d(N+1)>\mu_D$, one electron can tunnel out of the dot to the drain. As a result of this, the electro-chemical potential drops to $\mu_d(N)$. Now a new electron can tunnel into the dot and the whole process repeats again. This regime, when current is carried by successive discrete charging and discharging of the quantum dot, is known as single charge tunnelling[7].

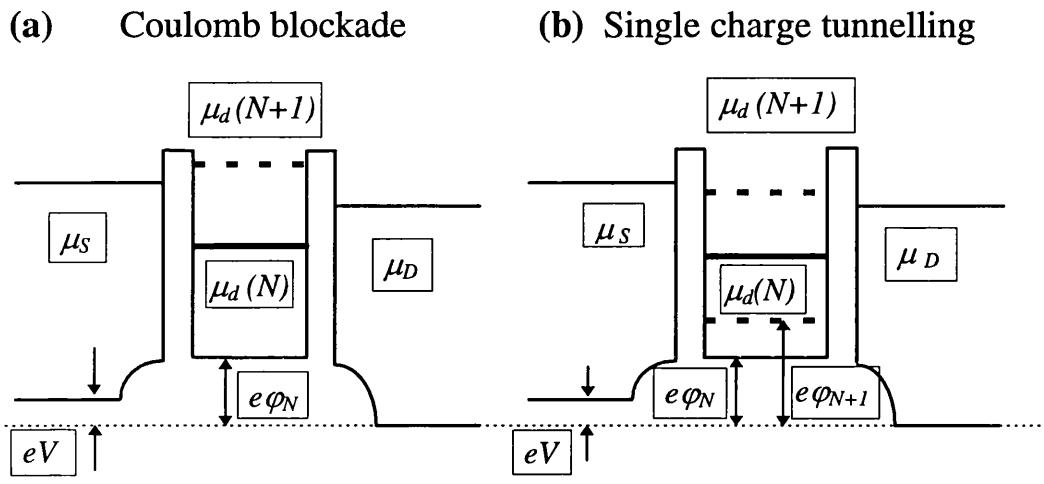

Figure 5.2: *Two characteristic situations for different G2 voltages. (a) Coulomb blockade of electron tunnelling* $(\mu_d(N)<\mu_D<\mu_S<\mu_d(N+1))$. *(b) Electron tunnelling at the* $N \rightarrow N+1$ *transition* $(\mu_S<\mu_d(N+1)<\mu_D)$. *V indicates the excitation voltage across the sample* $(eV<<\mu_d(N+1)-\mu_d(N))$.

As the gate voltage is changed, the conductance through the quantum dot oscillates between zero (Coulomb blockade), and non-zero (no Coulomb blockade) These oscillations are illustrated in Figure 5.3a. In the Coulomb blockade regime, at a conductance minimum, the number of electrons in the dot is fixed. This case is shown in Figure 5.3b. At a conductance maximum, this number oscillates by one electron, and electrostatic potential $e\varphi$ oscillates by e^2/C. In between two conductance maxima, $e\varphi$ changes by $E_{N+1}-E_N+e^2/C$. The

average slope of $e\varphi$ versus V_g reflects the (de)population of the dot without charging effects.

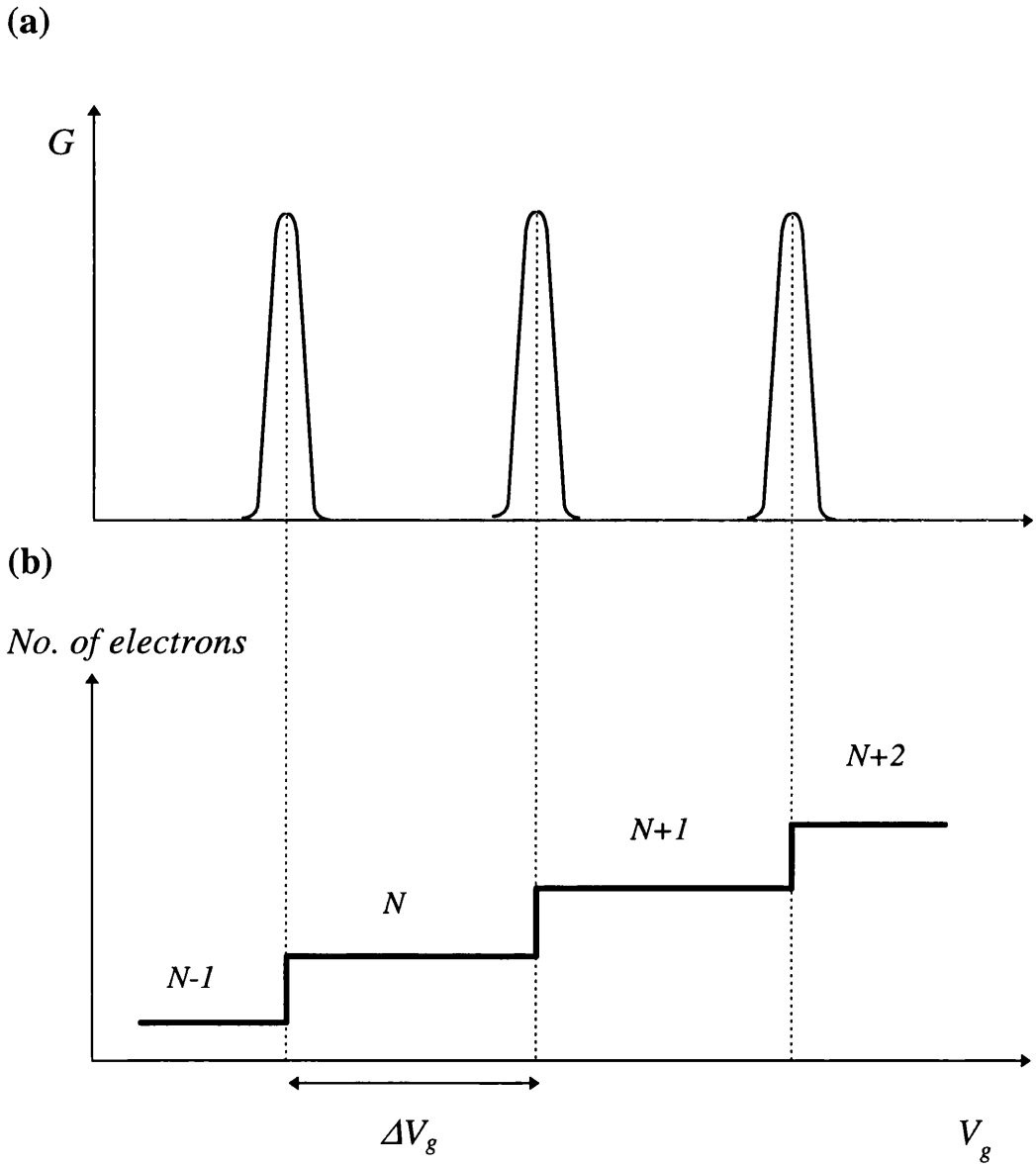

Figure 5.3: *Comparison of the conductance G (a), and the number of electrons N_{dot} (b) in the quantum dot. Between the Coulomb oscillations N_{dot} remains constant, which corresponds to the Coulomb blockade (see Figure 5.2a). At the maximum of the oscillations, N_{dot} oscillates by one electron, and $e\varphi$ oscillates by e^2/C. In this case, the Coulomb blockade is removed, and single electron transport through the quantum dot becomes possible.*

From Equation 5.2 and the condition $\mu_d(N,V_g)=\mu_d(N+1,\ V_g+\Delta V_g\ )$, the period of the Coulomb oscillations in gate voltage ΔV_g corresponding to a change of one electron in the dot can be written:

$$\Delta V_g = \frac{C}{C_g}\left(\frac{E_{N+1}-E_N}{e}\right)+\frac{e}{C_g} \tag{5.5}$$

For vanishing energy splitting of the single particle states E_{N+1}-$E_N \approx 0$, the gate voltage-capacitance relation for a single electron charge is obtained: $\Delta V_g = e/C_g$.

The Coulomb blockade can also be removed by increasing the bias voltage between the reservoirs. The energy interval $eV=\mu_S-\mu_D$ determines the transport through the quantum dot. As long as the energy interval between μ_S and μ_D does not contain a charge state as indicated in Figure 5.2a, the current is zero. Current flow will start when either $\mu_S>\mu_d(N+1)>\mu_D$ or $\mu_S>\mu_d(N)>\mu_D$. In this case, a single charge channel is opened, corresponding to either the $N\rightarrow(N+1)$ or the $(N-1)\rightarrow N$ transition. As the bias voltage is further increased, a second channel will open up when two charge states are contained between μ_S and μ_D, giving rise to a second increase of the current through the quantum dot.

5.2 Optimisation of Quantum Dots

A theory has been developed[14] to assist with the design and fabrication of surface gated quantum dots with a view to maximise the single particle energy level spacing inside the quantum dot. As the magnitude of the level spacing strongly affects the behaviour of a quantum dot, these calculations enable us to optimise the geometry and size of the dots to study single electron charging effects in these nanostructures in the maximum temperature range of operation. To test this theory, measurements were carried out at 1.2 K on surface gated quantum dots with lithographic diameters in the range from 100 nm to 350 nm.

Sub-micron devices usually have large, unmetallised surfaces, which means that surfaces have a great effect on their properties. In these devices gates

are used to pattern the 2DEG, leaving large, exposed surfaces. In the following the explanations and calculations are presented for the pinned and frozen models, describing different surface behaviour.

5.2.1 Pinned Surface Approximation

It is usually assumed, especially for devices at room temperature, that the Fermi energy E_F is pinned at a fixed energy below the conduction band on free surfaces of GaAs. This is an unambiguous assumption in equilibrium, when E_F is constant throughout the device. As soon as negative bias V_g is applied to a gate on the surface, it is no longer clear whether the free surface is pinned to E_F in the 2DEG or to that under the biased gate. However the device would not produce a quantum dot if the free surface was pinned to the gate, as no difference between the surface and the gate would be seen from inside the material. Thus it must be assumed that the free surface remains pinned to E_F in the 2DEG. We take this as the zero potential energy, giving a convenient boundary condition.

As a first approximation, we consider a complete circular gate on a surface of radius S_0, confining a 2DEG underneath. The electrostatic potential at (R,z) can be written

$$\phi(R,z)=\frac{2|z|}{\pi}\int_0^{\infty} S\phi(S,z=0)\left(\frac{1}{z^2+(R-S)^2}\right)\left(\frac{1}{\sqrt{z^2+(R+S)^2}}\right)E\left(\frac{4RS}{z^2+(R+S)^2}\right)dS$$

where S is a radial parameter on the surface and E is a complete elliptic integral of 2nd kind. Considering the case when the electrostatic potential is entirely determined by the voltage on the gate, $\phi=V_g$ for $(S>a)$ which is appropriate for the quantum dot (see Figure 5.4a[15]), the above integral can be expanded and solved:

$$\phi(R,z)=\frac{V_g|z|}{\sqrt{\left(z^2+a^2\right)}}\left[1+\frac{3}{4}\frac{R^2a^2}{\left(z^2+a^2\right)^2}\right] \qquad (5.7)$$

where a is the radius of the circular gate. The potential at the 2DEG can be written

(a)

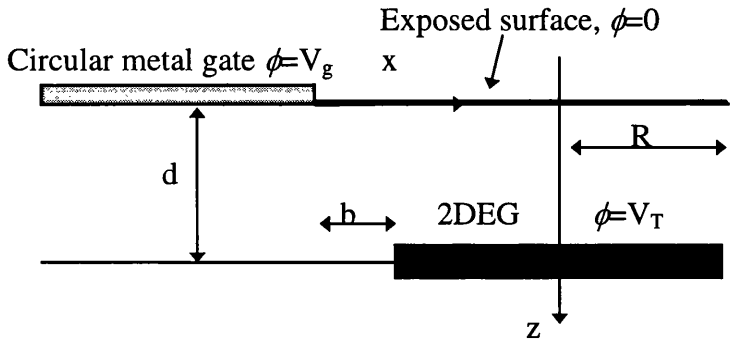

(b)

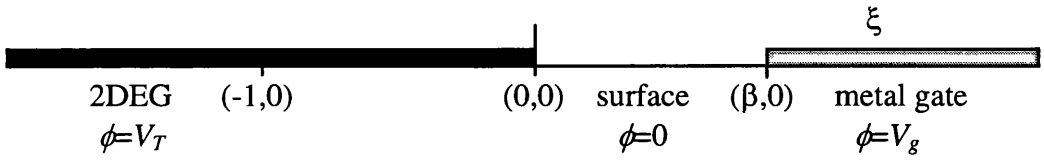

Figure 5.4: *(a) Geometry of the semi-infinite gate occupying x<0 on the surface of the heterostructure which defines the plane z=0. The 2DEG lies in the plane z=d with the region x>b occupied. (b) Conformal transformation to the ξ plane. The edge of the 2DEG maps to ξ=-1, and the edge of the gate maps to ξ=β.*

$$V_C = V_T \frac{\sqrt{(z^2 + a^2)}}{|z|} \tag{5.8}$$

where V_C is the cut-off voltage to completely deplete the 2DEG and V_T is the threshold voltage for a bulk gate. The energy level spacing can be determined from the curvature of the quadratic term in the bare potential. Maximising this it can be found that the biggest single particle level spacing can be achieved when $b=d$, where d is the depth of the 2DEG and b is the depletion width. The energy level spacing in the dot then can be written

$$\Delta E_S = \hbar \sqrt{\left(\frac{e}{m}\right)} \sqrt{\frac{3}{2}} \sqrt{V_T} \left(\frac{a}{a + z^2}\right) \tag{5.9}$$

Taking $b=d$ the maximum energy level spacing is

$$\Delta E_S = \hbar\sqrt{\left(\frac{e}{m}\right)}\sqrt{\frac{3}{8}}\sqrt{\frac{V_T}{d^2}} \tag{5.10}$$

Substituting

$$V_T = \frac{em^* E_F d}{\pi\hbar^2 \varepsilon\varepsilon_0} \tag{5.11}$$

into Equation 5.10 we get the expression for maximum level spacing

$$\max(\Delta E_S) = \sqrt{\frac{3}{2\pi}}\sqrt{\frac{e^2}{\varepsilon\varepsilon_0}}\sqrt{\frac{E_F}{d}}\left[\frac{a/d}{(a/d)^2+1}\right] \tag{5.12}$$

taking the Fermi energy E_F=21 meV and a/d=1 the energy level separation ΔE_S=10 meV using the pinned surface approximation. This value is significantly greater than that obtained in the measurements. The reasons for this difference will be discussed in the next sub-chapter.

5.2.2 Frozen Surface Approximation

If a pinned surface is assumed, charge must move from the 2DEG to the surface in order to keep its potential constant in response to a change in gate voltage V_g. This charge movement is possible at room temperature but seems unlikely at low temperatures (at and below 1 K) at which experiments on nanostructures are usually performed, and the charge on the surface is most likely to be frozen under these conditions. In this case the surface should be treated as a simple dielectric boundary, with a fixed charge density, in response to a change in V_g applied at low temperature. This is the frozen surface. In this case again for a circular gate we are looking for a solution in a form

$$\phi = -\frac{\xi z}{\pi}\left[\tan^{-1}\left(\frac{a}{\sqrt{\xi}}\right) - \frac{a}{\sqrt{\xi}}\right] \tag{5.13}$$

with boundary conditions

$\phi \rightarrow 0$ when $z \rightarrow \infty$ and

$$\frac{\partial \phi}{\partial z} = -\xi \text{ when } z \rightarrow -\infty \tag{5.14}$$

In Equation 5.13 ξ is the electric field and a is the radius of the electron pool, see Figure 5.5b. Solving Equation 5.13, the potential at the 2DEG can be written:

$$V_C = V_T\left[1 - \frac{2}{\pi}\tan^{-1}\left(\frac{a}{d}\right) + \frac{2a}{\pi d}\right] \tag{5.15}$$

From Equations 5.13 and 5.15 the ratio between a and d for maximum single particle level spacing can be calculated, see Equation 5.16:

$$a = \sqrt{3}d \tag{5.16}$$

The single particle level spacing can be written

$$\Delta E_S = \hbar\sqrt{\frac{e}{m}}\sqrt{\frac{2V_T}{\pi}}\frac{a^{\frac{3}{2}}}{\sqrt{d}\left(d^2 + a^2\right)} \tag{5.17}$$

Substituting the expression for V_T into Equation 5.17 the maximum value for single particle level separation can be calculated taking E_F=21 meV and d=35 nm.

$$\max(\Delta E_S) = 7.4\ meV \tag{5.18}$$

This value for the maximum single particle level spacing is lower than that for the pinned surface approximation, and closer to the experimentally obtained values as will be shown in the next chapter. Table 5.1 summarises the relevant values obtained in the above calculations using the pinned and frozen surface approximations.

	Pinned surface	*Frozen surface*
V_C / V_T	$\sqrt{\left(\frac{a}{d}\right)^2 + 1}$	$\left(1 - \frac{2}{\pi} tan^{-1}\left(\frac{a}{d}\right) + \frac{2a}{\pi d}\right)$
Value of a/d for maximum energy level spacing	1	$\sqrt{3}$
Maximum value (meV)	10	7.4

Table 5.1: *Single particle level spacing values and expressions obtained using both pinned and frozen surface approximations.*

Using the above expression for the frozen surface, the energy level spacing inside the quantum dot can be calculated as a function of effective dot radius *a* for different 2DEG depth *d*, see Figure 5.5. The energy level spacing rises sharply as the dot radius increases. The slope of the curve is the steepest in case of the shallow 2DEG (35 nm), reaching its maximum value of 7.4 meV for dot radius a≅60 nm. For dot radius values bigger than 60 nm the energy level spacing decreases fast. As the depth of the 2DEG increases the steepness of curvatures significantly decreases and the value of energy level spacing reaches its value of 3 meV for electron depth of 71 nm. The maximum value of energy level spacing slightly shifts to bigger radius values as the electron depth increases, indicating the optimal dot size for ideal electron confinement in the quantum dot.

5.3 Depletion Length in Surface Gated Quantum Dots

The calculations in the previous sub-chapter for the energy level spacing in quantum dots in the pinned and frozen surface model served us a general guide

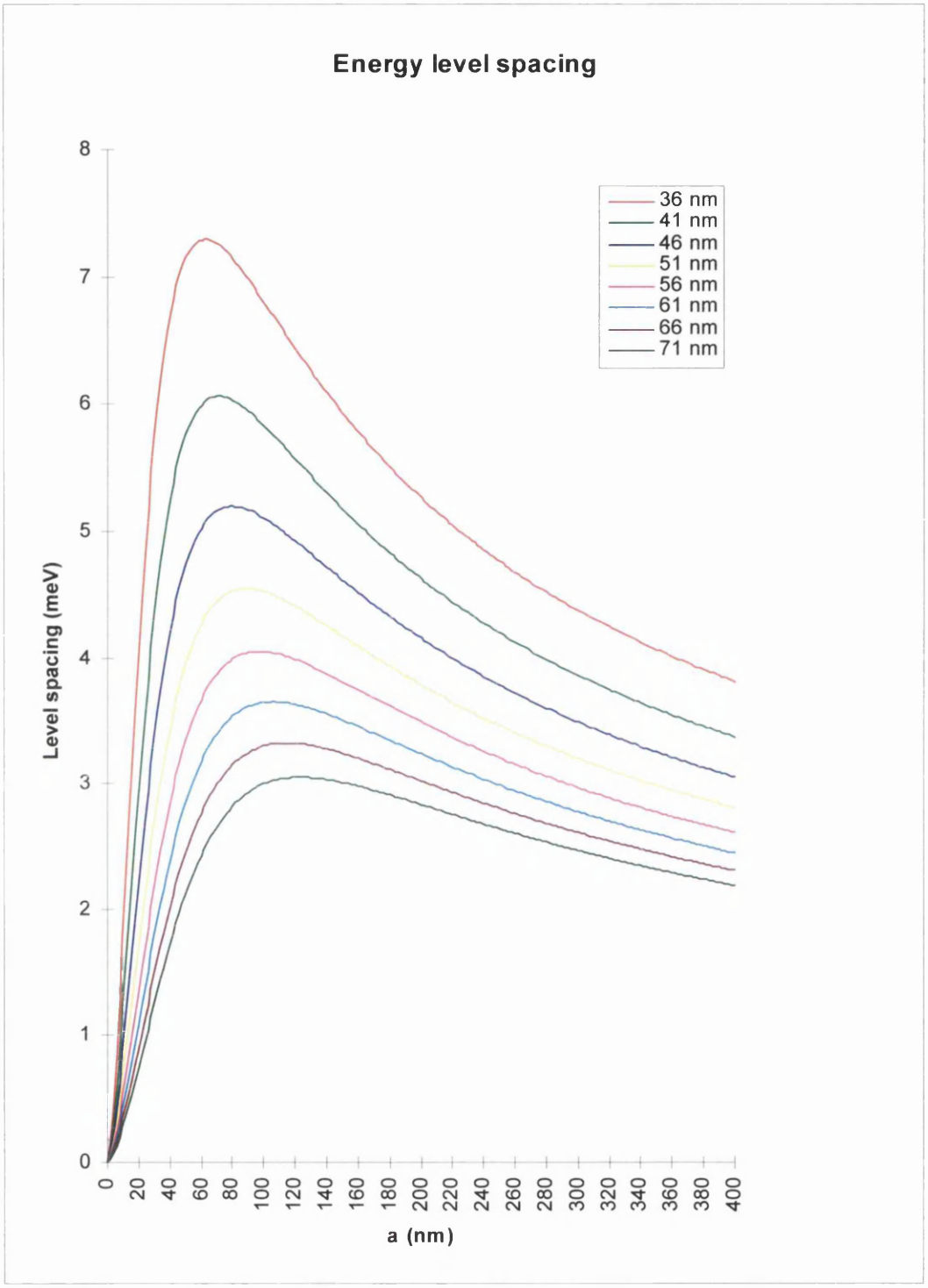

Figure 5.5: *Single particle energy level spacing inside the quantum dots as a function of effective dot radius for different 2DEG depths, calculated using the frozen surface model.*

to fabricate and measure our quantum dots. Both surface models are for bare potential and this gives an upper estimate of the single particle energy level separation in the quantum dot. At the opposite limit, where dots are full the individual electron states are ignored and occupation is treated as a semi-classical problem. As our results have confirmed the level spacing in our measured quantum dots was closer to the result obtained in the frozen surface model. These results were used to design and fabricate our devices to achieve the highest possible energy level spacing.

We now consider approaches to the problem of an occupied quantum dot. In surface gated quantum dots the edge[15] and shape of the electron pool is determined by the geometry of the patterned metal gates[16] forming the dot and the gate voltage applied to them. Variation of the bias on the metal gates controls the distance between the edges of the gates and that of the electron pool inside the dot, see Figure 5.6. It was shown[15] that the density of electrons in the dot increases from zero at the edge to its full value in the centre of the dot. The distance between the edge of the electron pool and the gates will be used in further analysis to determine the effective size of the electron pool inside the quantum dot and thus the Coulomb energies.

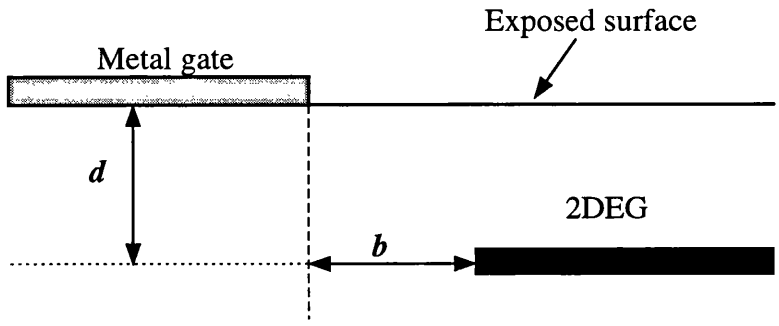

Figure 5.6: *Geometry of the metal gate on the surface of a heterostructure. The 2DEG lies in the plane z=d, partially occupying it.*

The depletion length *b* will be given in the frozen surface model which assumes that the charge on the surface is fixed and cannot move in response to a gate voltage. We assumed that the frozen surface model is realistic for devices measured at low temperature as in the experiments.

The electrostatic problem of finding the edge of a 2DEG in gated heterostructures was solved by conformal mapping[15]. The condition of zero density at the edge of the 2DEG gives

$$\alpha = 2\left(\frac{V_g}{V_T} - 1\right) \tag{5.19}$$

where

$$\alpha + \lambda\nu\alpha + 1 = \frac{\pi\beta}{\delta} \tag{5.20}$$

V_g is the voltage applied to the gate, V_T the threshold voltage needed to apply to the gate to remove the electrons from underneath it, b is the distance between the edge of electron pool and that of the gate in the x-y plane and d is the depth of the 2DEG beneath the surface of the heterostructure. Using Equation 5.19 the distance b can be determined for any gate voltage. The above calculations can be extended to estimate the depletion length in quantum dots, see Table 5.2.

V_g/V_T	d [nm]	b [nm]	a [nm]	N
1.5	28	18	57	51
2	28	33	42	28
2.5	28	45	30	14
3	28	57	18	5

Table 5.2: *Number of electrons N in the quantum dot for different V_g/V_T ratios. The electron depth is 28 nm, sheet electron density is 5 10^{15} $1/m^2$, b is the depletion length and a is the radius of the electron pool in nanometres.*

Experimental results show that the quantum dots are depleted for the gate and threshold voltage ratio of $\frac{V_g}{V_T} = 2 \leftrightarrow 2.5$ which is in good agreement with the

calculated values in Table 5.2. Calculating the $\frac{V_g}{V_T}$ ratio for 28 nm and 36 nm electron depth, the value comes to 2.7 and 2.23, respectively, which is in good agreement with the experimentally obtained value. The above ratios correspond to a quantum dot radius of a=45↔55 nm. We assume the value of 50 nm for the length of the depletion region[15].

5.4 Measurements

5.4.1 350 nm Quantum Dot Z19A

The geometry of the first measured quantum dot Z19A is depicted in Figure 5.7a. The geometry of this device significantly differed from those measured later in the course of the project. The dot had a diameter of 350 nm with point contacts at the entry and exit of the dot of 80-90 nm wide. (Assuming $4 \cdot 10^{15}$ m^{-2} carrier concentration and a 50 nm depletion region, the number of electrons in the dot was around 120). The measurement was performed at 1.2 K by applying constant negative voltages to gates *G1, G3, G4* and sweeping the voltage on the middle plunger gate *G2*. The two QPCs, forming the quantum dot showed very similar conductance plateaux, with the plunger bias slightly affecting their conductance characteristics.

As illustrated in Figure 5.7b, each conductance oscillation corresponds to a change of one electron in the dot. We can derive from the period of oscillations ΔV_P=6±0.3 mV a capacitance between the dot and the plunger gate C_P=$2.7 \cdot 10^{-17}$ F ignoring single particle energy differences.

As the bias on the plunger becomes more negative the period of oscillations slightly increases indicating that the capacitance between the dot and the plunger decreases with diminishing number of electrons in the quantum dot.

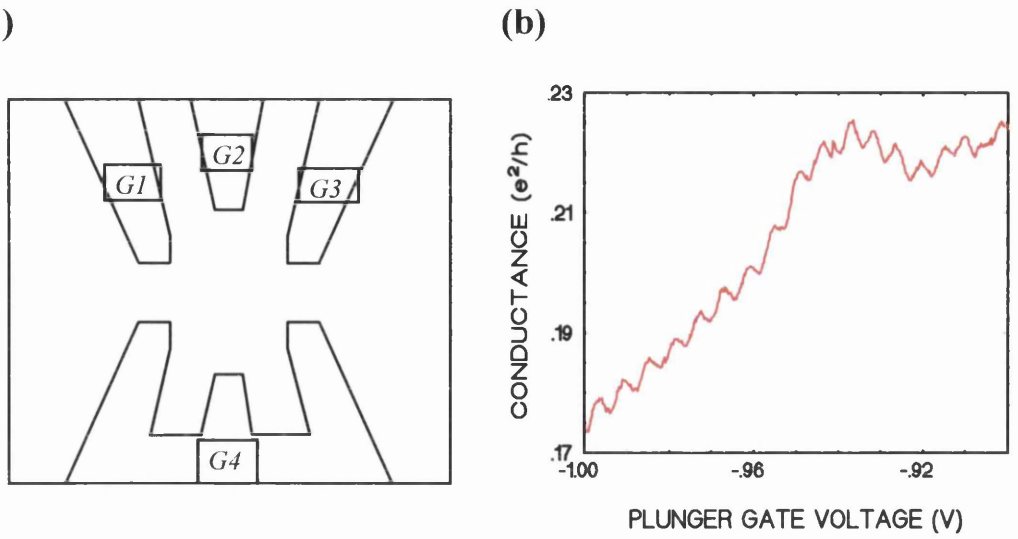

Figure 5.7: *(a) Geometry of quantum dot Z19A formed with four metal gates G1, G2, G3, G4. (b) Conductance oscillations as a function of the plunger gate voltage at 1.2 K with G1=-0.82 V, G3=-0.73 V and G4=-0.82 V on the gates.*

The lower gate *G4* was shaped in order to create similar gate structure with the upper gates *G1*, *G2* and *G3*.

5.4.2 250 nm Quantum Dot Z20A

This dot had similar geometry to Z19A illustrated in Figure 2.5 with a lithographic dot diameter of 250 nm. The two QPCs had significantly different conductance characteristics as a function of the gate voltage at different negative bias on the plunger gate. The period of oscillations was about ΔV_P=12±0.8 mV sweeping the plunger gate what corresponds to C_P=1.3·10^{-17} F capacitance between the plunger gate and the quantum dot. The period and the amplitude of oscillations slightly change as the plunger voltage is more negatively biased. The peak to valley ratio is significantly higher in dot Z20A than that in dot Z19A, see Figure 5.8.

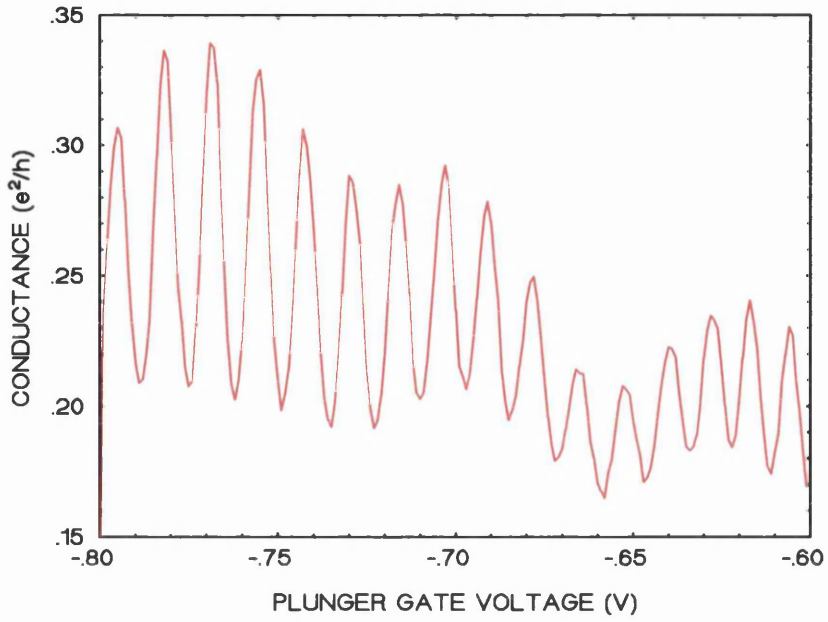

Figure 5.8: *Conductance oscillations in quantum dot Z20A as a function of plunger gate voltage at 1.2 K with G1=-0.71 V, G3=-0.65 V and G4=-0.71 V on the surrounding gates.*

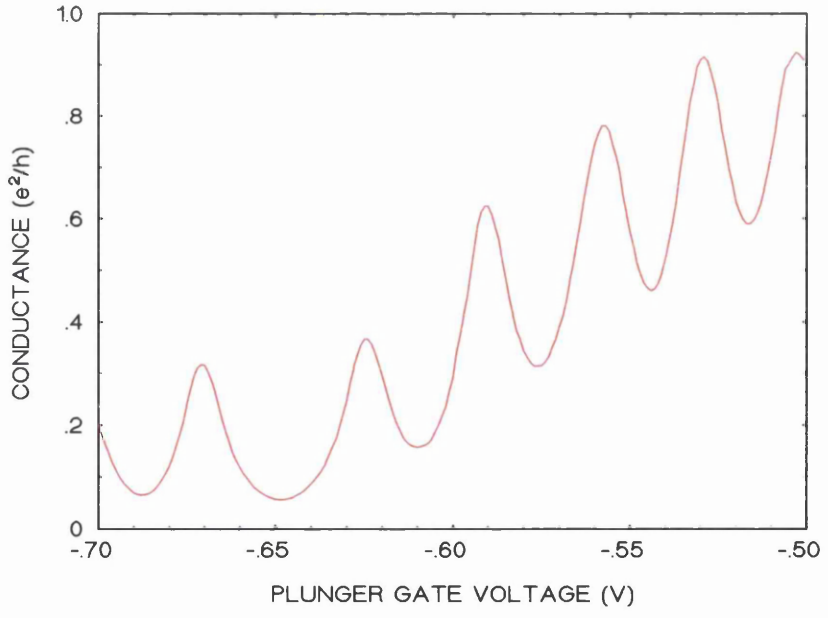

Figure 5.9: *Conductance oscillations in quantum dot Z2B as a function of plunger gate bias at 1.2 K and gate bias conditions G1=-0.53 V, G3=-0.53 V and G4=-0.535 V. Note the change of shape of oscillations at more negative gate voltages.*

5.4.3 150 nm Quantum Dot Z2B

This quantum dot had a more circular shape than those measured earlier, making it easier to model this device. In this measurement it became apparent that the shape and the position of the gates forming the quantum dot strongly affects its characteristics, such as oscillatory behaviour, electron distribution and depletion voltage.

The two QPCs were not characterised in this sample as the dot showed oscillatory behaviour for a wide range of gate biases. The period of oscillations sweeping the plunger gate was equal to 35 mV corresponding to $4.6 \cdot 10^{-18}$ F capacitance between the plunger gate and the quantum dot. The period and the shape of oscillations changed with greater negative bias on the plunger gate, see Figure 5.9. The dot was made smaller by increasing the negative bias on the surrounding gates while sweeping the plunger what resulted in oscillations with 4.5 mV period giving $3.5 \cdot 10^{-17}$ F capacitance between the gates and the dot ignoring energy level differences in the dot. This value was significantly bigger than that for the plunger gate showing the dependence of the capacitance between the dot and the number and area of the gates. The blockade period varied noticeably with gate bias. This suggests that the number of electrons in the dot was small and that the underlying single particle energies had a significant effect on the period.

5.4.4 150 nm Quantum Dot Z212B

This 150 nm quantum dot showed regular oscillatory behaviour over a wide plunger gate voltage range. The two QPCs were characterised at different plunger gate biases and showed very similar characteristics. The period of oscillations when sweeping all gates connected together differed only slightly from that when sweeping the plunger gate, indicating that *G1*, *G2* and *G3* were interconnected in this sample. When all the gates were connected together the oscillations started at -0.3 V and died out at -0.45 V with a period of about 3.1 mV. During the course of the measurement the period of oscillations as a

function of the gate voltage changed rather significantly. The period of oscillations then fell between 6.6 and 20 mV, indicating a radical change in the state of the sample probably due to the change in the local potential environment.

5.4.5 120 nm Quantum Dot Series Z27

The smallest surface gated quantum dots measured during the course of the project were from the series Z27 with a 120 nm nominal diameter. Considering the 50 nm depletion region at the threshold voltage, this is the smallest feasible dot size for quantum transport measurement. As the measurement showed, this dot size was too small to form an electron pool in the middle of the dot, the potential well being apparently too shallow in it. Five 120 nm quantum dots were measured from the same series and all showed similar characteristics.

Quantum dot Z27A showed rather noisy oscillatory behaviour at high negative gate voltages, with low peak to valley ratio. The electron pool inside the dot was made smaller by gradually increasing the bias voltages on gates *G1*, *G3* and *G4*, which increased the depletion region between the gates and the electron pool in the dot. As a result of this, the period of oscillations and the peak to valley ratio increased at more negative voltage on the plunger gate, see Figure 5.10. This indicated that plunger gate strongly affected the transport characteristics of the quantum dot at high negative voltages on the surrounding gates.

Quantum dot Z27B also showed noisy characteristics similar to those of Z27A, but at significantly lower negative voltages on the gates, see Figure 5.11. The period of oscillations and the peak to valley ratio increased again at more negative voltages on the plunger gate. The average oscillation period in the covered plunger voltage range was 14.4 mV compared to 12.2 mV in Z27A. The value of 14.4 mV corresponds to $1.1 \cdot 10^{-17}$ F capacitance between the plunger gate and the dot. The period of conductance oscillations for sweeping gates *G1/G2/G3* connected together in dot Z27A is twice as much as that in dot Z27B (9.4 mV and 4.5 mV respectively), what might be explained by the possible difference in gate

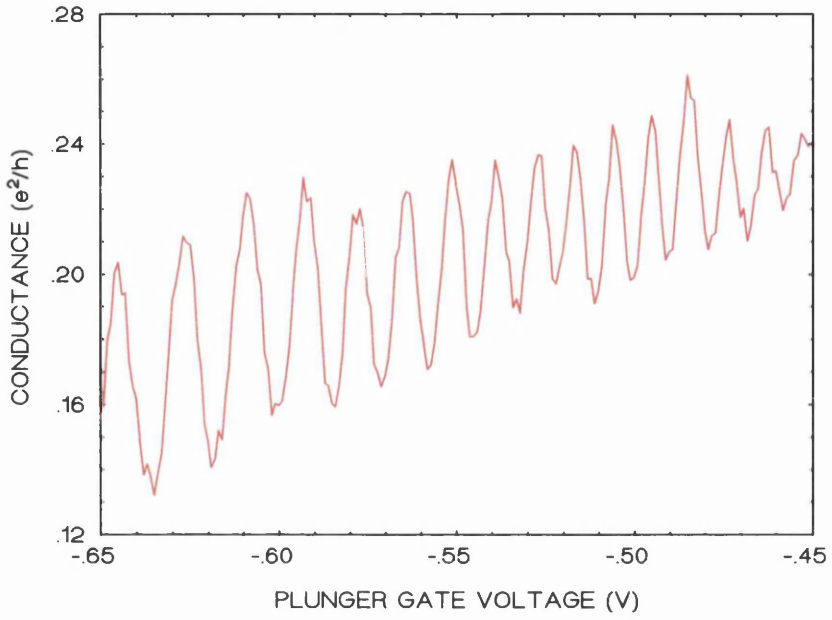

Figure 5.10: *Conductance oscillations in Quantum Dot Z27A as a function of the plunger gate voltage at 1.2 K and with G1=-0.46 V, G3=-0.45 V and G4=-0.48 V on the gates. Note the change in the period of oscillations at increasingly more negative gate voltages.*

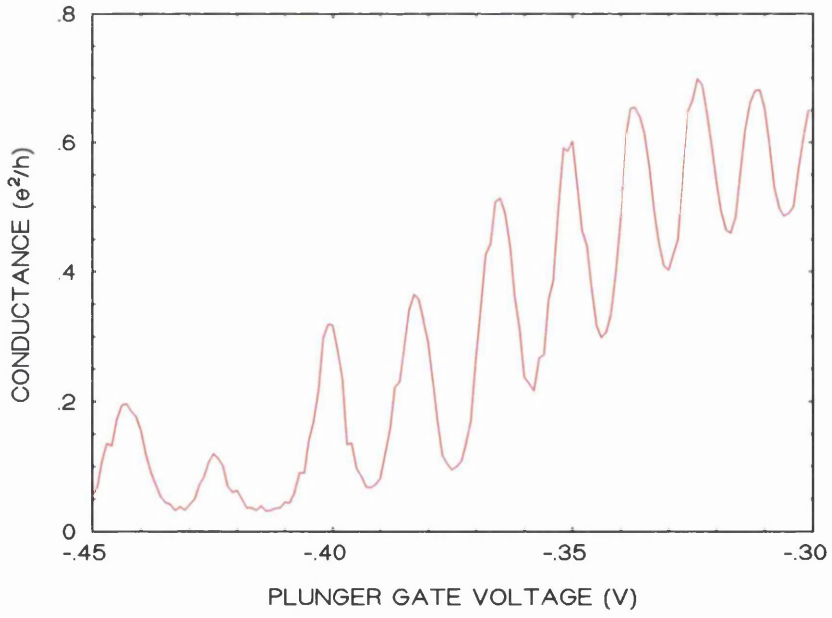

Figure 5.11: *Conductance oscillations in Z27B as a function of the plunger gate voltage at 1.2 K with gate bias condition G1=-0.37 V, G3=-0.37 V and G4=-0.37 V.*

structure. However the origin of this difference has not been unambiguously determined.

5.4.6 Double Gated 200 nm Quantum Dots

Three samples were measured with three double gated quantum dots on each sample containing one single, one double and one quadruple quantum dot, with the same diameter, 200 nm (Figure 5.12). The samples were backgated[17] using the chip carrier as a back gate. The distance between the surface of the sample and the chip carrier was about 440 μm. Probably due to this distance, the change of the backgate voltage on the plane of the chip carrier (0 and -5 V) in a measured gate bias voltage range resulted in a weak conductance modulation of 0.002 e^2/h only. This low conductance modulation value indicated that the idea of using the chip carrier as a back gate could not be successfully realised. The best results were obtained for the single and double quantum dots, on both samples Z216A and Z216B with similar oscillation periods in *G1* and *G2* (22±1.1 mV and 18±1.2 mV respectively). Sweeping *G1* and *G2* connected together resulted in 9 mV period indicating that the capacitance value of the gates connected together to the dot is twice as big as that of either *G1* or *G2*.

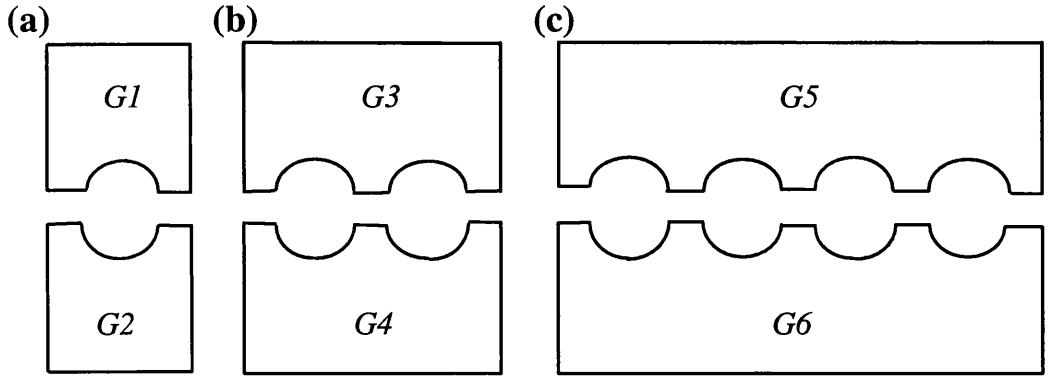

Figure 5.12: *Schematic diagram depicting double gated (a) single, (b) double and (c) quadruple quantum dots. The distance between each the gate pair defining the single, double and quadruple quantum dots is 90 μm.*

Only a few irregular peaks were observed sweeping *G5* and *G6* without a trace of double or quadruple peak structure reported in literature[18].

5.5 Electrostatic Potential and Number of Electrons in Surface Gated Quantum Dots

Some of the measured quantum dots were modelled by Larkin and Davies, using a number of approaches[18]. The bare potential distribution in the plane of the 2DEG of the 150 nm dot in Figure 5.13a was calculated by modelling the gates as semi-infinite polygons, and the result for the case when all the gates have equal potential with respect to a pinned surface potential is shown in Figure 5.13b. This model permits an estimate of the cut-off voltage and also the number of electrons in the dot.

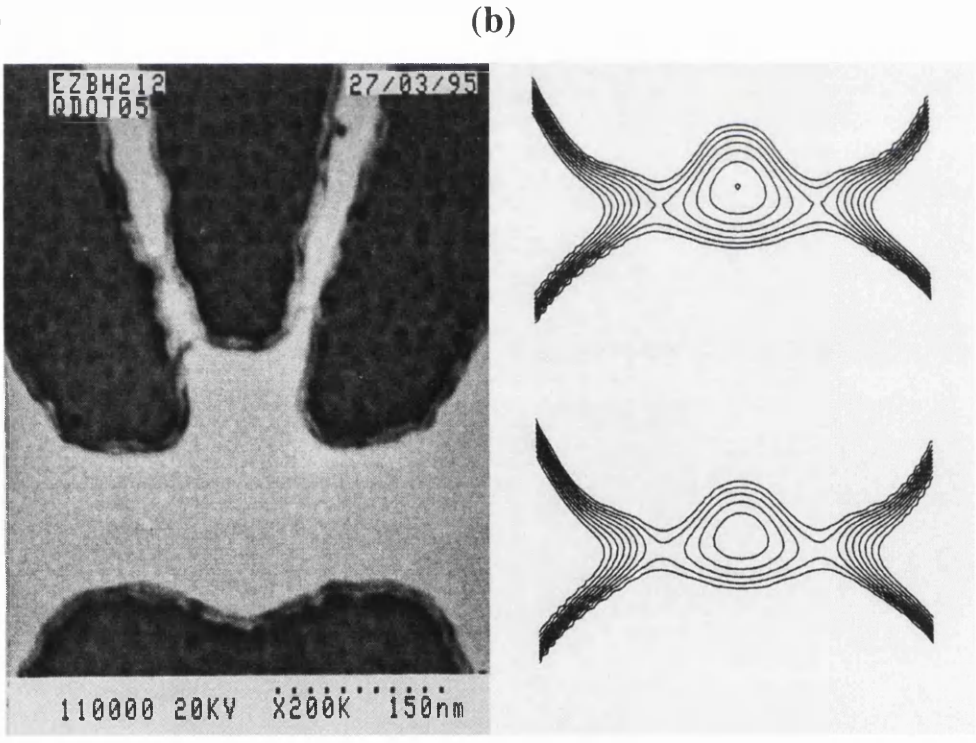

Figure 5.13: *(a) Micrograph of the 150 nm quantum dot. (b) the bare electrostatic potential contours for a quantum dot in the same configuration with a bias of -0.5 V (top) and -0.7 V (bottom) on the plunger gate, and -0.5 V on all other gates. Note the change of the shape of the electrostatic potential contours.*

Self-consistent semiclassical calculations, using a method[20] developed for quantum point contacts, show that there are about 13 electrons on the 150 nm dot Z2B when it just becomes isolated from the 2DEG reservoirs, with all gates connected together. A gate voltage of -1.1 V was needed in the calculation, about twice the experimental value, and the period of blockade oscillations was also too large at 12 meV. This may be the indication that the surface charge is frozen, rather than the Fermi energy pinned to that of the 2DEG as assumed in the calculation; this would also lead to better confinement of the electrons by reducing the screening of the central gate. Although all calculations agree that there is a small number of electrons in the dot, they are very sensitive to the precise dimensions of the gates and to the behaviour of the surface when applied to our devices.

In case of the 350 nm quantum dot Z19A the agreement between theory and experiment was much better, where there was a factor of two discrepancy between the change in number of electrons predicted by the model (22) and that seen in the experiment (38). Here the difference between the pinned and frozen surface models should be less marked because the large dot itself plays the role of an equipotential plane.

5.6 Discussion

Numerous surface gated quantum dots have been measured in the 350-100 nm diameter range, in order to test the theory for single particle energy level spacing in quantum dots. The number of electrons and the corresponding single level spacing are shown in Table 5.3.

Assuming perfect screening, when the potential level in the quantum dot centre is not raised, the average single level spacing can easily be calculated using the relation

$$\Delta E_S \leq 2\frac{E_F}{N} \tag{5.21}$$

Dot lithographic diameter (nm)	*Carrier concentration n [m^{-2}]*	*Number of electrons N in the dot*	*Average single particle level spacing δ[meV]*
350	$4 \cdot 10^{15}$	190	0.2
250	$4.5 \cdot 10^{15}$	80	0.5
200	$4.5 \cdot 10^{15}$	35	1.2
150	$5.6 \cdot 10^{15}$	11	3.8
120	$4.2 \cdot 10^{15}$	3	14

Table 5.3: *Comparison of single particle spacing for surface gated quantum dots of different lithographic diameter, assuming 50 nm depletion region.*

where E_F is the Fermi energy in the dot (21 meV) and N is the number of electrons in the dot. The number of electrons is calculated from the carrier concentration considering a 50 nm depletion region. It is apparent from Table 5.3 that the average single particle level spacing increases as the number of electrons in the dot decreases. Thus by reducing the lithographic diameter of the dot to a certain size, it is possible to increase the single particle level spacing in the dot.

For the series of measured dots the conductance modulation at a constant temperature of 1.2 K increases rapidly as the dot size decreases, see Table 5.4. The conductance modulation increases up to 150 nm dot size and decreases in case of the 120 nm dot as expected from the theory thus indicating the optimal dot size.

Dot lithographic diameter (nm)	*Average conductance modulation Peak to valley ratio (e^2/h)*
350	0.003
250	0.04
200	0.07
150	0.19
120	0.15
100	0.11

Table 5.4: *Conductance modulation depending on the lithographic diameter of the quantum dot.*

Conductance modulation data presented in Table 5.4 has been averaged for each quantum dot at 1.2 K and at the same conductance value through the quantum dots (0.2 e^2/h), when the quantum point contacts demonstrated the same transport characteristics.

Spectroscopy measurements had been performed on two quantum dots of 150 nm nominal diameter giving very intriguing results. These results will be presented in Chapter 8.

5.7 Conclusions

Analytical calculations based on the pinned and frozen surface model, proved that the latter gives a better description of the characteristics of the nanostructures we measured during the course of the project. Using the frozen surface approximation we could determine the physical parameters of the quantum dot which would give the biggest energy level separation in the dot. The main aim of this chapter was to test the theoretical calculations and fabricate the optimal dot which was capable of functioning in the high temperature (above 1.2 K) regime. According to the frozen surface model, the optimal quantum dot size to achieve the biggest single particle level spacing inside the quantum dot is

$$a = d\sqrt{3} \tag{5.22}$$

where a is the nominal radius of the quantum dot and d is the depth of the 2DEG beneath the surface of the semiconductor. Taking d=35 nm in case of the shallow 2DEG gives an effective dot diameter of 120 nm. Several surface gated quantum dots have been fabricated and measured in the 350-100 nm nominal diameter range. It was found that the 150 nm diameter quantum dots had the biggest period of oscillations and peak to valley ratio, indicating the highest single particle level spacing as predicted by the frozen surface model. These results were checked using temperature dependence and DC source-bias measurements, which also showed that the potential well for electrons inside the dot is most optimal for the

150 nm dot size, see Equation 5.16. After this result has been established, in the later course of the project detailed studies have been carried out on 150 nm quantum dots. This studies also included spectroscopy measurements on 150 nm quantum dots in the few electron regime which are presented in Chapter 8.

References

1. D V Averin and K K Likharev, *Quantum Effects in Small Disordered Systems* edited by B Altshuler, P Lee and R Webb (Elsevier, Amsterdam,1990).

2. J H F Scott-Thomas, S B Field, M A Kastner, H I Smith and D A Antonadis, Phys. Rev. Lett. **62**, 583 (1989).

3. U Meirav, M A Kastner and S J Wind, Phys Lett. **65**, 771 (1990).

4. P L McEuen, E B Foxman, U Meirav, M A Kastner, Y Meir, N S Wingreen and S J Wind, Phys. Rev. Lett. **66**, 1926 (1991).

5. B J van Wees, L P Kouwenhoven, C J Harmans, J G Williamson, C E Timmering, M E Broekaart, C T Foxon and J J Harris, Phys. Rev. Lett. **62**, 2523 (1989).

6. N C van der Vaart, S F Godijn, Y V Nazarov, C J Harmans and J E Mooij, Phys. Rev. Lett. 64, 3452 (1990).

7. *Single Charge Tunnelling*, H Grabert, J M Martinis and M H Devoret. (Plenum, New York, 1991).

8. H T Imam, V V Ponomarenko, D V Averin, Phys. Rev. B, **50**, 18288, (1994).

9. Y V Nazarov and A V Khaetskii, Phys. Rev. B, **49**, 5077, (1994).

10. A Furusaki and K A Matveev, Phys. Rev. Lett. **75**, 709, (1995).

11. L P Kouwenhoven, Transport of Electron-Waves and Single-Charges in Semiconductor Nanostructures, Thesis, (1992).

12. B J van Wees, H van Houten, C W J Beenakker, J G Williamson, L P Kouwenhoven, D van der Marel and C T Foxon, Phys. Rev. Lett. **60**, 848 (1988).

13. D V Averin and Y V Nazarov, Phys. Rev. Lett. **65**, 2446 (1990).

14. J H Davies and I A Larkin, JAP, vol. 77, No. 9, 4504 (1995).

15. I A Larkin and J H Davies, Phys. Rev. B, **52**, 5535 (1995).

16. M J Berry, J A Katine, R M Westervelt, A C Gossard, Phys. Rev. B, **50**, 17721 (1994).

17. S Nakata, Phys. Rev. B, **47**, 1679 (1993).

18. Z Borsosfoldi, I A Larkin, M Rahman, J H Davies, M C Holland, J R Weaver, A R Long, J G Williamson, in *Proceedings of the 22nd Conference on the Physics of Semiconductors*, edited by D J Lockwood (World Scientific, Singapore, 1995) p. 1887.

19. L P Kouwenhoven, F W Hekking, B J van Wees, C J Harmans, Phys. Rev. Lett. **65**, 361 (1990).

20. J A Nixon, J H Davies, H U Baranger, Phys. Rev. B, **43**, 12638 (1991).

Chapter 6

Temperature Dependence Measurements in Quantum Dots

6.1 Introduction

The phenomenon of Coulomb blockade has been observed at temperatures up to 300 K and beyond in systems such as granular films and scanning probe tips,[1-3] however realisation of useful device structures using these technologies is difficult. On the other hand, structures such as metal-insulator-metal tunnel junction arrays,[4] or laterally patterned quantum dots,[5-7] are fully controllable but require much lower temperatures for operation, again limiting their utility. Tunnel junction structures generally show charging effects at millikelvin temperatures, and this requires junction sizes 30 nm^2 or less. Surface gated quantum dots, which are easier to fabricate than ultrasmall tunnel junctions, have so far only shown charging effects at temperatures of around 4 K.[8-10] Recent work[11] on a silicon single electron transistor demonstrated very strong Coulomb blockade oscillations at 4.2 K, probably strong enough for this transistor to work well above 4.2 K.

In this chapter we show that the range of operation of surface gated quantum dots can be enhanced beyond 4 K through the combined use of shallow heterostructure technology and high resolution electron-beam lithography. This enhanced range of operation of our devices means that the experiments can easily be performed without a dilution fridge and increases the potential usefulness of these devices.

6.2 Theory of Temperature Dependence

Two different theories have been developed for temperature regime depending on the relation between the energies characterising the quantum dot. There are three energy scales of importance in addition to kT: the charging energy E_C, the energy level separation in the quantum dot ΔE with a fixed number of electrons, and the width of the discrete energy levels in the quantum dot Γ. As kT is usually larger than Γ, there are two interesting temperature regimes[12]

$$E_C > kT > \Delta E \tag{6.1}$$

$$E_C > \Delta E > kT \tag{6.2}$$

Equation 6.1 shows the inequalities for the multilevel regime because there are more than one energy level within kT. As the energy level separation in the quantum dot is mainly determined by the size of the dot, this regime applies either to metallic artificial atoms or large semiconductor quantum dots. For sufficiently small semiconductor quantum dots we can reach the limit when the energy level separation is bigger than kT, see Equation 6.2. In this regime ΔE is sufficiently big that the properties of the single energy levels in the quantum dot are resolved.

To explain the quantum-mechanical effects in quantum dots, the constant-interaction model[13,14] was developed. This model assumes that the charging energy E_C in the quantum dot is constant, independent of the number of electrons added to it. In semiconductor quantum dots the energy level spacing is large enough so that at low temperature only one energy level determines the conductance. It was shown[15] that the constant-interaction model is too simplified because the charging energy E_C is not the same for every electron added to the dot, but this model works well for a limited number of electrons in the quantum dot.

The theory for the resonant tunnelling of nonicteracting particles is found to describe the behaviour of quantum dots reasonably accurately. At zero temperature:

$$G_S = p\frac{e^2}{h}\left(\frac{\Gamma_L\Gamma_R}{(E-E_0)^2+\Gamma^2}\right) \tag{6.3}$$

In Equation 6.3 $E=\mu$ is the chemical potential, E_0 is the value of the resonant energy level, Γ_L and Γ_R are the tunnelling rates (multiplied by h) through the left and right barriers respectively, $\Gamma=(\Gamma_L+\Gamma_R)/2$ and p is the level degeneracy of the resonant energy level in the quantum dot. At finite temperature the conductance is given by the convolution of $G(E)$ in Equation 6.3 with the negative derivative of the Fermi-Dirac distribution function, and thus the conductance can be written:[12]

$$G_S = p\frac{e^2}{h}\frac{\Gamma_L\Gamma_R}{\Gamma^2}\int\frac{dE}{kT}\left\{\frac{\Gamma^2}{(E-E_0)^2+\Gamma^2}\right\}sech^2\left[\frac{E-\mu}{2kT}\right] \tag{6.4}$$

The Lorentzian becomes a delta function in the limit $\Gamma\to 0$. Hence G_S for narrow resonances at high T is proportional to the derivative of the Fermi-Dirac function $\left(sech^2[(E-\mu)/2kT]/kT\right)$. In the experiments the chemical potential is varied by changing the voltage V_g on a gate electrode next to the quantum dot. If $\Gamma<<kT$ Equation 6.4 reduces to:

$$G_S = p\frac{e^2}{h}\pi\frac{\Gamma_L\Gamma_R}{\Gamma}\frac{kT}{2}sech^2\left[\frac{E_0-\alpha eV_g}{2kT}\right] \tag{6.5}$$

In Equation 6.5 αeV_g is the chemical potential. Experiments[5] have shown that Equation 6.4 is in excellent agreement with experimental shapes of conductance peaks.

In the multilevel regime the conductance through the dot is given by:[16]

$$G_M = \frac{e^2}{h}\frac{\rho}{4}\frac{\Gamma_L\Gamma_R}{\Gamma}\frac{\mu_C - \alpha e V_g}{kT}\operatorname{cosech}\left[\frac{\mu_C - \alpha e V_g}{kT}\right] \tag{6.6}$$

where ρ is the density of energy levels and μ_C is the chemical potential for which there is a charge degeneracy point for the quantum dot. So $\mu_C/\alpha e$ is the gate voltage at which the states with N and $N+1$ electrons have the same energy, which is the condition for a conductance peak. Equation 6.6 can be approximated in the form:

$$G_M = \frac{e^2}{h}\frac{\rho}{4}\frac{\Gamma_L\Gamma_R}{\Gamma}\operatorname{sech}^2\left[\frac{\mu_C - \alpha e V_g}{2.5kT}\right] \tag{6.7}$$

The shapes of the conductance peaks for the two different regimes are indistinguishable, but there is a significant difference in the temperature dependence. The peak height for the single level conductance is proportional to $1/T$, whereas for the multilevel conductance it is temperature independent. The other difference is that the full width at half maximum of the peak is 3.5 kT for the single level case and 4.35 kT for the multilevel case.

6.2.1 Line Shape of Coulomb Blockade Oscillations at and above 1.2 K

The line shape of Coulomb blockade oscillations can be fitted well by thermally broadened Lorentzians. We show that our temperature dependence data can be fitted to a thermally broadened Lorentzian[18], see Equation 6.8:

$$G = \frac{e^2}{h}\frac{A}{4kT}\int_{-\infty}^{\infty}\cosh^{-2}\left(\frac{E-\mu}{2kT}\right)\frac{(\Gamma/2)\pi}{(\Gamma/2)^2 + (E - E_0 - \mu)^2}dE \tag{6.8}$$

where A is a temperature-independent value, Γ is the Lorentzian full width at half-maximum. This integral can be evaluated in dimensionless units, see Equation 6.9:

$$GT \approx \int_{-\infty}^{\infty} \cosh^{-2}\left(\frac{\varepsilon}{2}\right) \frac{\gamma/2}{(\gamma/2)^2 + (\varepsilon - \varepsilon_0)^2} d\varepsilon \qquad (6.9)$$

where $\varepsilon = \left(\frac{E-\gamma}{kT}\right)$; $\varepsilon_0 = \frac{E_0}{kT}$; $\gamma = \frac{\Gamma}{kT}$.

The integral in Equation 6.9 is plotted as GT versus $\frac{E_0}{kT}$ for different values of $\frac{\Gamma}{2E_0}$ see Figure 6.1. The first four points on the graph between 0 and 3 $\frac{E_0}{kT}$ fits to the data on quantum dot Z2B (conductance valley M1, see Figure 6.4), within 50 % accuracy.

From Equation 6.9 and Figure 6.1 it can be observed that at a given E_0, for Γ=0, GT decreases to zero and for a finite Γ, G saturates at low T.

It is easily detectable from Figure 6.1 that the curve with $\frac{\Gamma}{2E_0}$=0.1 fits best the experimental data (indicated by M1) in Figure 6.6. This indicates a value of ΔE=0.65 meV obtained between 1.2 and 5.6 K.

6.3 Measurements

Temperature dependence measurements were performed on seven surface gated quantum dots to determine experimentally the temperature range of operation for our devices. The following subsections detail the main experimental temperature dependence features of our quantum dots with different nominal quantum dot diameters.

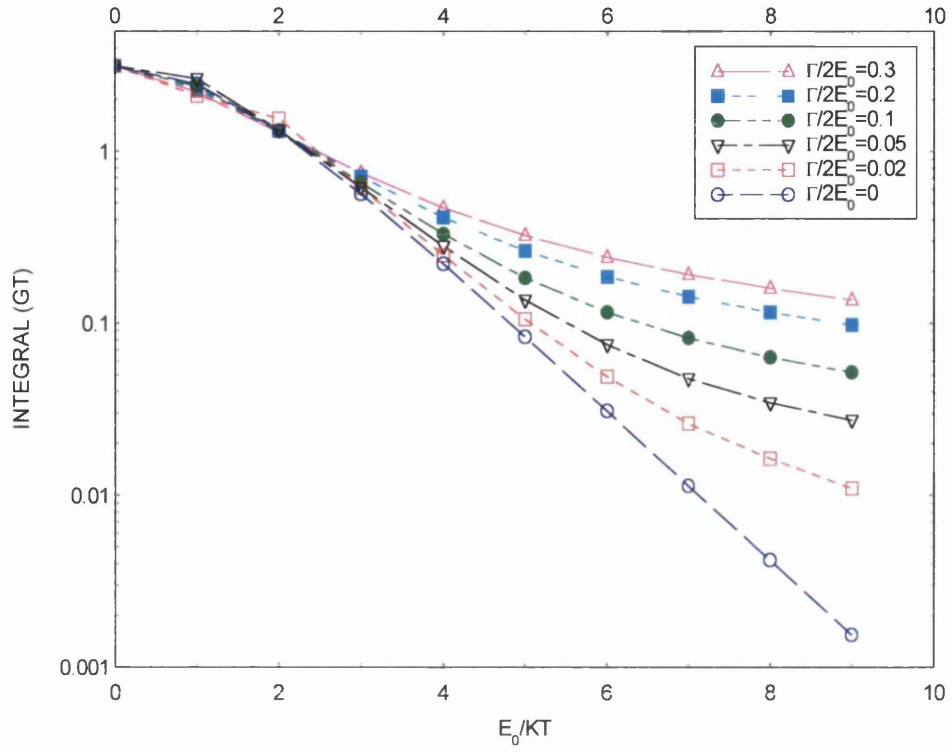

Figure 6.1 : *Plot of GT versus* $\frac{E_0}{kT}$.

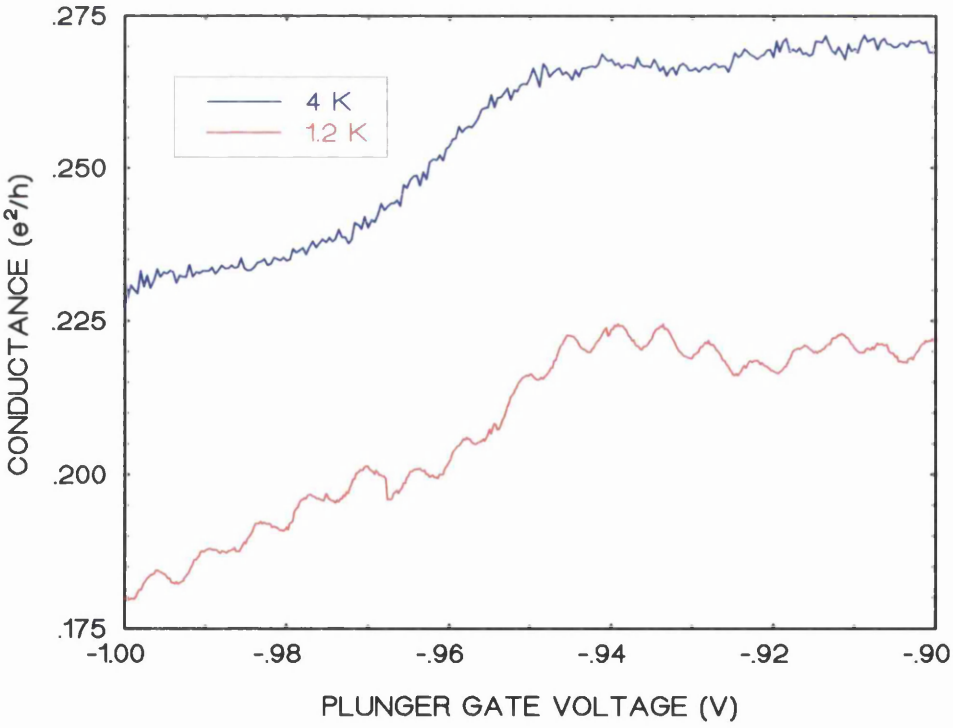

Figure 6.2: *Conductance oscillations in the 350 nm quantum dot Z19A at 1.2 and 4 K. The oscillations are thermally broadened and disappear just above 4 K.*

6.3.1 350 nm quantum dot Z19A

This four gated quantum dot with the largest diameter of 350 nm showed a few thermally broadened oscillations at 1.2 K. When swept independently, the entrance and exit point contacts exhibited quantization in their conductance although there were additional resonances superimposed. This additional structure may be attributed to quantum interference effects in the potential landscape surrounding the point contact, arising from the presence of the other gates.[6] Generally an isolated point contact on this shallow material exhibits quantization with little additional structure.

To achieve the Coulomb blockade regime in this dot high negative voltages, between -0.8 and -1.0 V were applied to the surrounding gates, see Figure 6.2.

The amplitude and the period of oscillations varied significantly in this sample, and the conductance of the dot decreased with more negative voltage on the plunger gate. At 4 K at around -0.91 V plunger gate voltage there are a few weak oscillations indicating a smearing temperature of about 4 K. The minimas of oscillations did not reach the value of zero conductance because of the high sample temperature of 1.2 K.

6.3.2 250 nm Quantum Dot Z20A

This quantum dot had the gate structure schematically illustrated in Chapter 3, Figure 3.4.b, with the plunger gate drawn into the centre of the dot which served the purpose of investigating the effect of the position of the plunger gate on the dot's behaviour. This quantum dot showed very clear, well resolved oscillations at 1.3 K, with increasing amplitude at higher negative voltages on the plunger gate. The gate voltages needed to reach the Coulomb blockade regime in this dot were more positive by 0.2 V than those in quantum dot Z19A, reflecting the difference in their geometries. The conductance oscillations start smearing at 1.6 K, but they are still strong at 2.9 K. The oscillations are just perceptible at 4.0 K and disappear at around 5.0 K. The overall conductance increases with

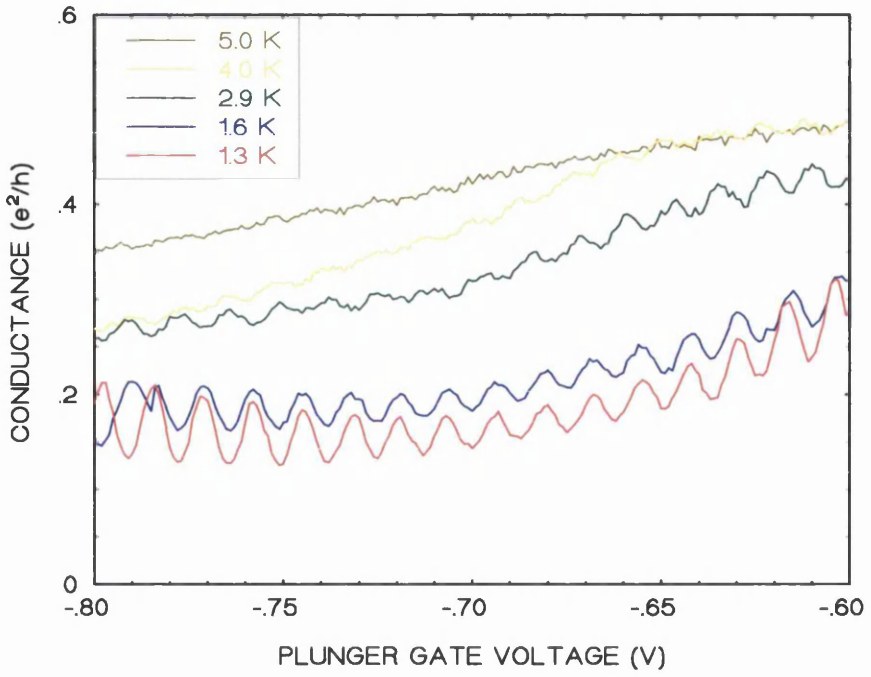

Figure 6.3: *Temperature dependence measurement in quantum dot Z20A. The conductance oscillations disappear at around 4 K as a result of thermal smearing. There are some oscillations still visible at 5 K between -0.76 and -0.8 V.*

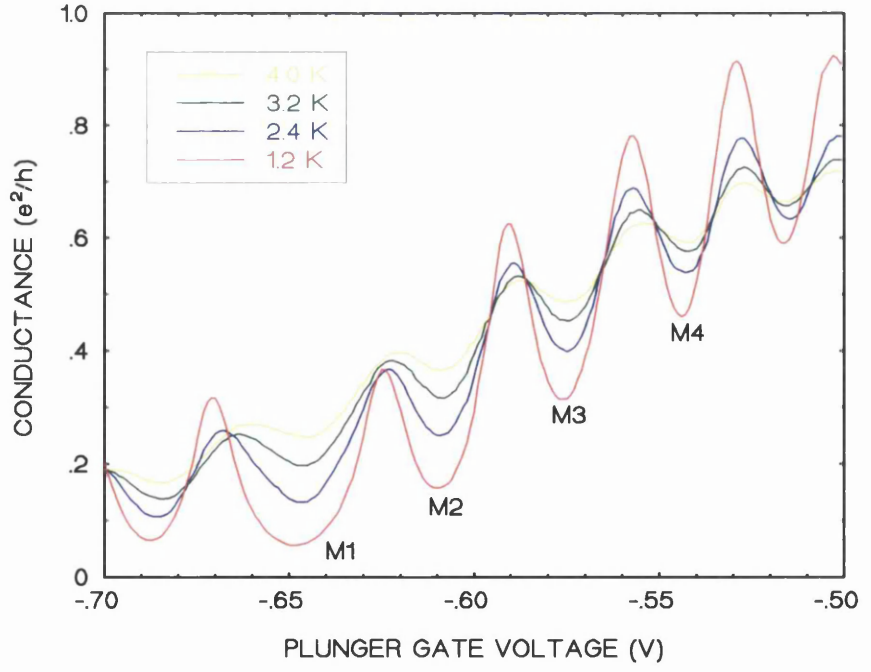

Figure 6.4: *Coulomb blockade oscillations in the 150 nm quantum dot Z2B. The period of oscillations changes at more negative gate voltages.*

increasing temperature, indicating the effect of thermal smearing, see Figure 6.3. The smearing temperature of around 4 K gives the energy level separation inside the dot of around 1.8 meV. As the temperature is increased only Coulomb oscillations at the most negative plunger voltages remain visible, when the number of electrons in the quantum dot is the smallest, thus the energy level separations are the biggest, which results in higher smearing temperature.

6.3.3 150 nm Quantum Dot Z2B

This quantum dot with its plunger gate withdrawn from the centre of the dot by about 20 nm compared to the position of the plunger of dot Z20A, showed conductance oscillations at the highest temperature reported so far in surface gated quantum dots.[17] The oscillations were well separated at 1.3 K, with varying period and maximas levelling out at more negative voltage on the plunger gate, see Figure 6.4.

The amplitude of oscillations starts to decrease gradually above 1.3 K but the oscillation peaks are still readily distinguishable at 4.0 K. The peaks of oscillations above 1.3 K start shifting in comparison to the peaks of oscillation at 1.3 K. As the temperature increases the amplitude of oscillations decreases and partially smears out at 7.7 K. There are still some well distinguishable oscillation peaks at 7.7 K, see Figure 6.5. The period of oscillations at 7.7 K slightly increases compared to those at 5.6 K and 6.8 K.

To find the energy level separation in the quantum dot which determines the smearing temperature of a certain conductance peak, we plot the $ln(GT)$ as a function of $1/T$, where G is the conductance of a particular oscillation minimum at different temperatures and T is the sample temperature. As an oscillation minima represents an energy gap between energy levels in the dot (when the number of electrons inside the quantum dot is necessarily fixed), by plotting the $ln(GT)$ versus $1/T$ curve for each oscillation minimum we can determine the energy level structure in the quantum dot in the measured gate voltage (chemical potential change) range, see Figure 6.6. Although the higher T points obey the

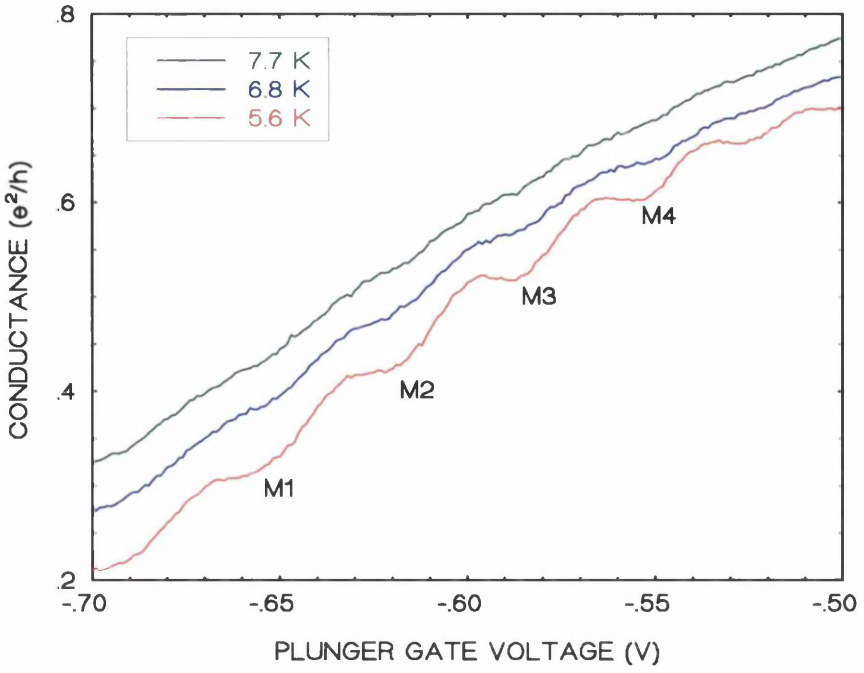

Figure 6.5: *Conductance oscillations in the 150 nm quantum dot Z2B at 5.6 K, 6.8 K and 7.7 K. The oscillations smears out above 7.7 K.*

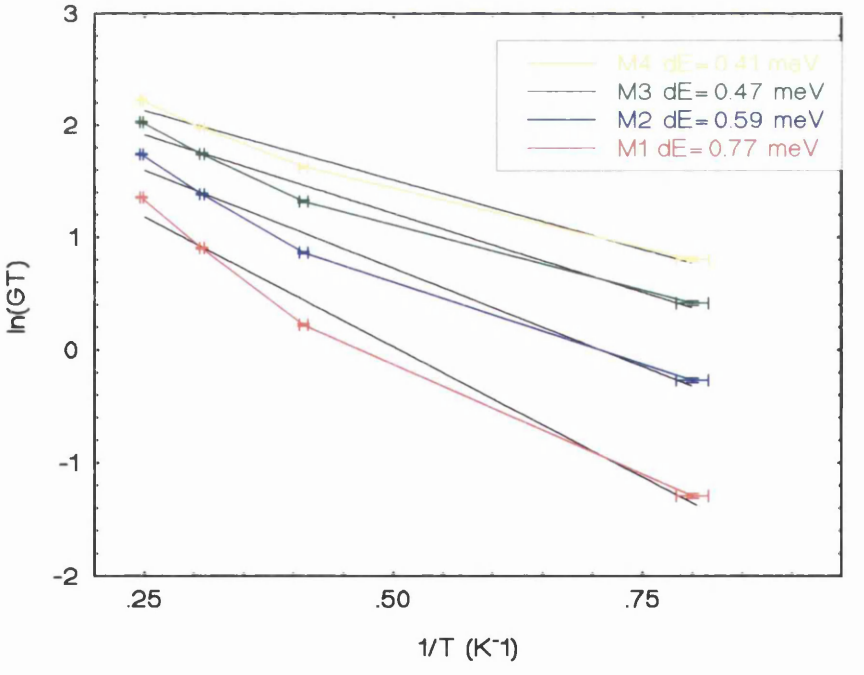

Figure 6.6: *Plot of ln(GT) as a function of reversed temperature 1/T for the three consecutive minimas M1, M2 and M3 (see Figure 6.4). The gradient of the fitted lines gives the energy level separation in the quantum dot at a particular conductance minimum.*

exponential relationships quite well, the lower T points show signs of saturation due to the finite Γ values.

From Figure 6.6 it is apparent that the energy gap significantly changes in the dot depending on the number of electrons in it. The gradient of the three lines determining the temperature dependence of three adjacent oscillations changes rather significantly, probably indicating that state of the many-electron system significantly changes every time an electron is removed from the quantum dot.

The conductance oscillations smear out when $kT>\Delta E$, where ΔE is the energy gap between the energy levels in the quantum dot. In our case it would mean that the oscillations should smear out at about 30 K. The smearing temperature is much lower than this in our quantum dots which could be explained with the electron temperature being significantly higher than the sample temperature.

6.3.4 150 nm Quantum Dot Z212B

This other 150 nm quantum dot had similar temperature dependence to that of Z2B, at significantly less negative gate voltages. The Coulomb blockade oscillations were persistent over a narrow gate voltage range, as in this sample gates *G1*, *G2*, *G3* and *G4* were interconnected. The strong oscillations were slightly shifted towards less negative gate voltages as the temperature increased, see Figure 6.7. There are strong, thermally broadened oscillations at 1.2 K which start smearing out at 1.5 K. The oscillations are still strong at 4 K but the amplitude of oscillations drop above 4 K and significantly decreases between 4 K and 6 K, see Figure 6.8. There are some weak Coulomb blockade oscillations detectable at 7.1 K, but they smear out above 7.1 K. The Coulomb oscillations are most persistent at 7.1 K in the gate voltage range -0.41– -0.44 V, where the amplitude of oscillations is the biggest at lower temperatures. The smearing temperatures are very similar in both 150 nm quantum dots indicating roughly similar energy gap values and energy level structure in them. The $ln(GT)$ versus $1/T$ dependence is shown in Figure 6.9, with the values of energy gaps indicated.

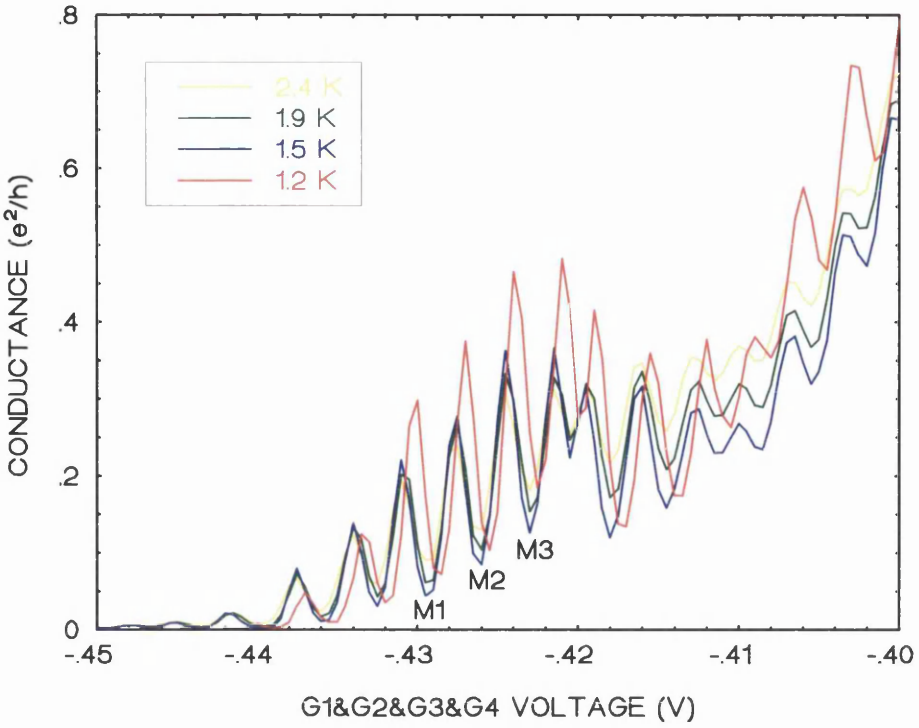

Figure 6.7: *Coulomb oscillations in quantum dot Z212B as a function of gate voltage (all gates interconnected) at different temperatures.*

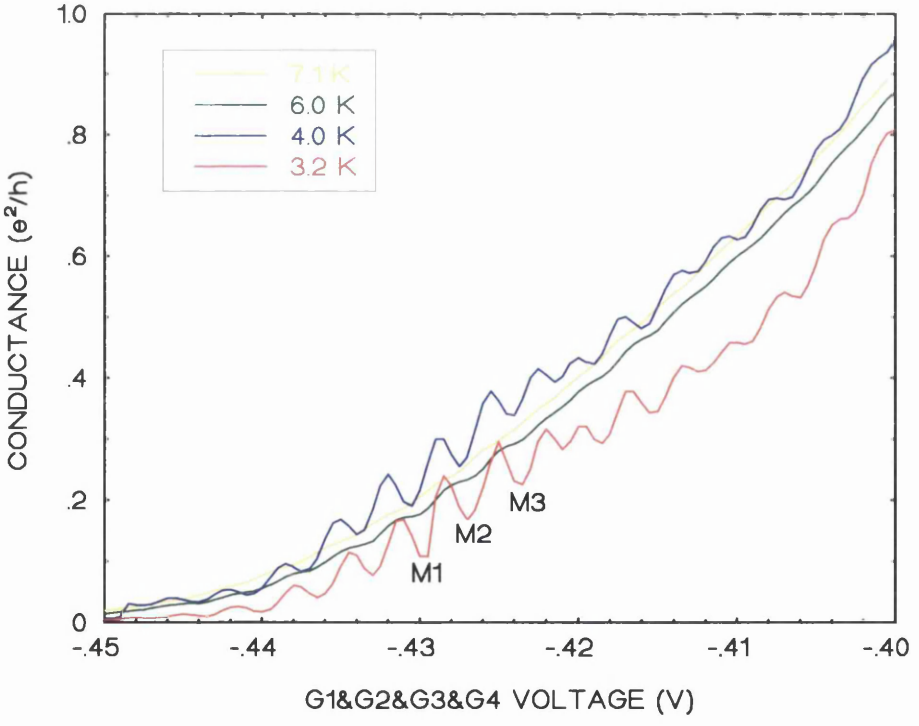

Figure 6.8: *Temperature dependence of Coulomb oscillations in dot Z212B at 3.2 K, 4 K, 6 K and 7.1 K.*

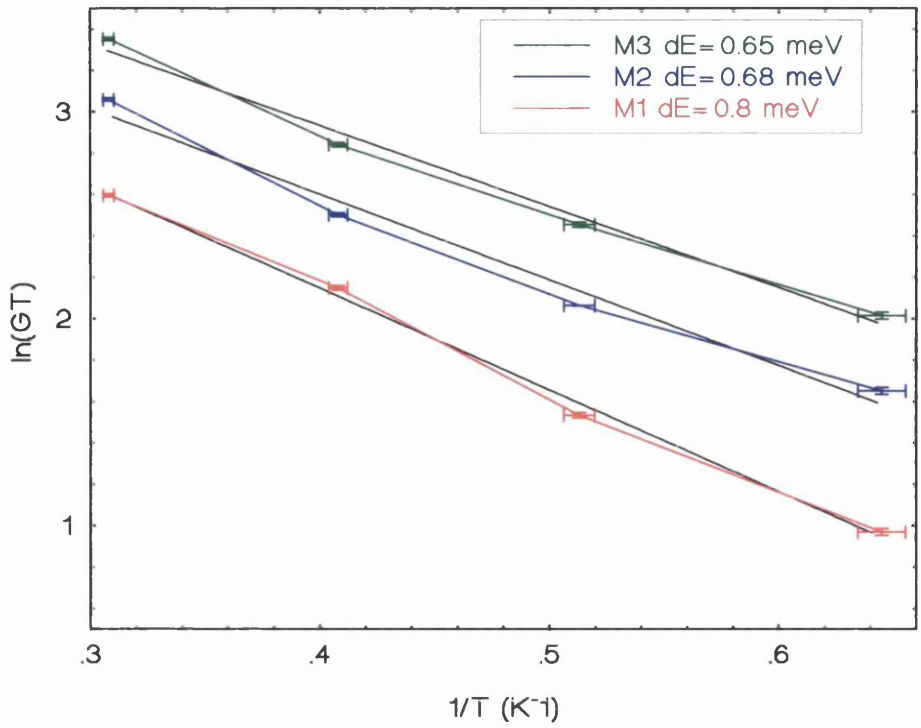

Figure 6.9: *Graph of ln(GT) as a function of 1/T for the three conductance minimas M1–M3 in Figure 6.8.*

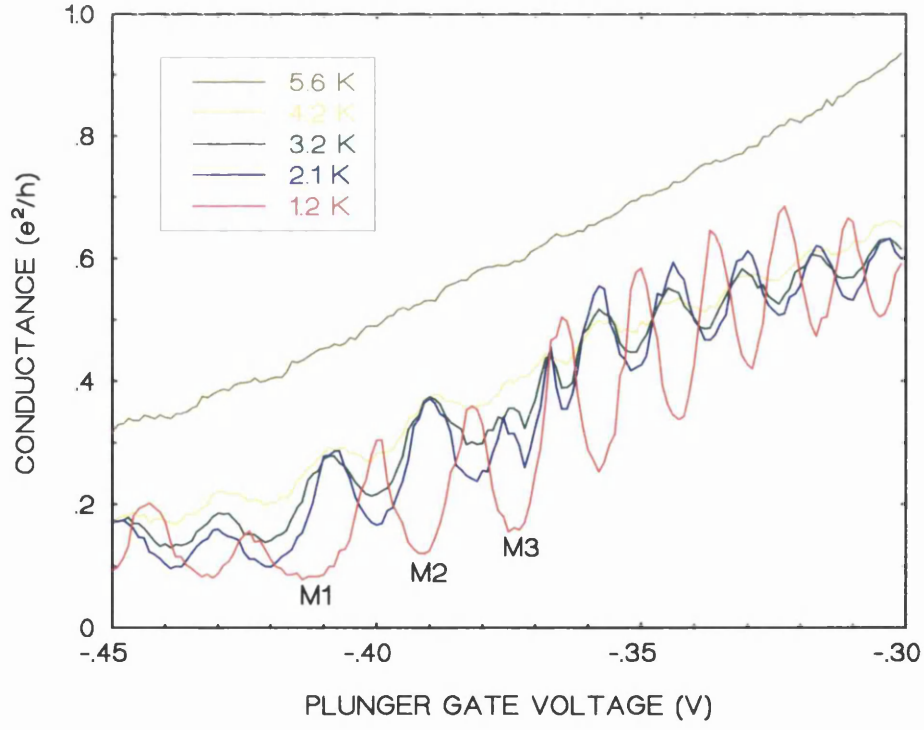

Figure 6.10: *Conductance oscillations in the 100 nm quantum dot Z27B.*

In Figure 6.9 the *ln(GT)* versus *1/T* dependence is shown for the three consecutive oscillation minimas starting at -0.43 V at 1.2 K, see Figure 6.8. As the dot size thus the number of electrons is reduced in the dot by applying increasingly more negative voltages to the gates, the energy gap, corresponding to a certain oscillation minimum increases. In quantum dot Z212B the energy gap between consecutive energy levels more than twofold increases between the oscillation minimas M1–M3, see Figure 6.8.

6.3.5 100 nm Quantum Dot Z27B

The smearing temperature in this quantum dot was lower than in the 150 nm dots, the Coulomb oscillations disappeared above 5.8 K. The curves taken at different temperatures were significantly shifting in conductance value as a result of a sample warm up, see Figure 6.10. The noise level of the oscillations increased with increasing sample temperature.

The *ln(GT)* dependence versus *1/T* for the first three conductance minimas M1–M3 is plotted in Figure 6.11. As expected from the blockade oscillations the energy gaps inside the dot changed rather randomly with the change of electron number in the quantum dot, indicating the presence of an unclear energy landscape.

The *ln(GT)* versus *1/T* plot for all three conductance minimas M1–M3 were curves, similar to those of quantum dot Z212B.

The period and amplitude of oscillations were relatively undefined, peaks became very uncertain between -0.36 and -0.39 V on the plunger gate, which were the smallest negative gate voltages used in measuring our quantum dots.

6.4 Conclusions

Temperature dependence measurements have been performed on seven quantum dots in a diameter range between 350 and 100 nm, showing Coulomb oscillations at higher temperature, up to 7.7 K. All devices were fabricated on

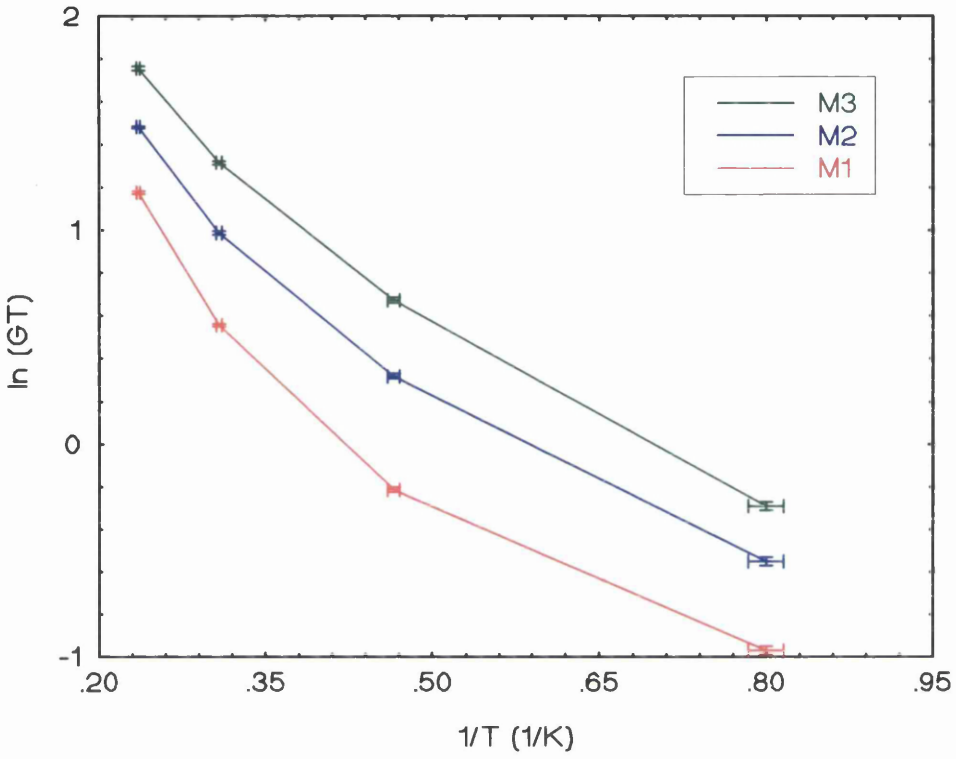

Figure 6.11: *Graph of ln(GT) versus 1/T in the 100 nm quantum dot Z27B.*

modulation doped heterostructures with the two dimensional electron gas at 28 nm below the surface with the structure depicted in Chapter 3, Figure 3.1.a. Considering the resolution limitation of the available electron-beam lithography, the minimal inner diameter for a surface gated quantum dot with the design shown in Figure 3.4.b is around 60 nm. Assuming a 50 nm depletion region between the gates and the electron pool in the dot as it has been discussed in Chapter 5, a quantum dot with a minimum of 100 nm diameter should be fabricated as a dot of this size can contain the fewest possible number of electrons. The metal gates forming these dots had a structure illustrated in Chapter 5, Figure 5.1.a. In most of the experiments the temperature dependence measurements were carried out by applying a constant negative gate bias to gates *G1*, *G3*, and *G4* at different temperatures and sweeping the central plunger gate *G2*. The plunger gate *G2* voltage allowed the size of the dot, and hence the number of electrons within it, to be varied electrostatically. The temperature range in which all the experiments were carried out was between 1.2 K and 9.6 K, using standard low frequency four-terminal lock-in techniques.

The energy gap between consecutive single particle energy levels were estimated in case of three quantum dots, see Table 6.1.

	Z2B (150 nm)		*Z212B (150 nm)*		*Z27B (100 nm)*	
	ΔE (meV)	T_{SM} (K)	ΔE (meV)	T_{SM} (K)	ΔE (meV)	T_{SM} (K)
M1	0.77	9	0.8	9.3	0.59	6.9
M2	0.59	6.9	0.68	7.9	0.58	6.7
M3	0.47	5.5	0.65	7.6	0.59	6.9
M4	0.41	4.8				

Table 6.1: *Energy gaps in three quantum dots with the corresponding estimated smearing temperatures.*

To estimate the smearing temperature in the measured quantum dots we used the expression $kT \geq \Delta E$ - when kT exceeds the energy level spacing, the conductance becomes constant and the Coulomb oscillation peaks smear out. The calculated smearing temperatures were in close agreement with the experimental values in all dots. In case of quantum dots Z2B and Z27B the single energy level spacing

was fluctuating and the smearing temperatures were within 15% of accuracy with the experimental values. In case of the 150 nm quantum dot Z212B all the gates surrounding the dot were swept together in the measurement. Thus the size of the dot was continuously reduced, showing stronger energy gap dependence as a function of gate voltage and temperature. As the negative voltage on the gates increases the energy level spacing and the smearing temperature in the dot increases. The agreement between the theoretical and measured values is worse than in the other two dots and it is within 20 % of accuracy. Thus the smearing temperature is the highest in quantum dots of small size when the energy gaps between consecutive energy levels are the biggest. It is difficult to calculate the energy gaps at higher temperatures because of the large background conductance.

Quantum dots fabricated on deep 2DEGs do not generally exhibit charging effects above 1 K. Dots fabricated by focused ion-beam (FIB) patterning, where the gating is in a plane, have shown Coulomb oscillations up to temperatures of 2-3 K. From our temperature dependence measurements it is clearly the lithographic dot size that affects the maximum temperature at which charging effects can be observed. This is as opposed to the electrostatic dot size, which has much less influence on the temperature dependence. Thus, for example, the oscillations from a dot with a lithographically small size survive to higher temperatures than those from a large dot squeezed electrostatically to a small size.

The increase in temperature at which charging effects smear can be understood in terms of "classical" capacitance effects. In general, for a given geometry of capacitor, the capacitance varies dimensionally with length. In our dots all dimensions are reduced compared to dots on deeper 2DEGs: the 2DEG is shallower, and the area of the dot is smaller. Thus we expect the capacitance to reduce, and hence the possible operating temperature to be enhanced. As the dot diameter is shrunk further from 350 nm down to 100 nm, the capacitance continues reducing and the charging energy and the single particle level spacing increases. Figure 6.12 shows the differences in the conductance of quantum dots of diameter 150 nm, 250 nm and 150 nm as a function of the plunger gate voltage

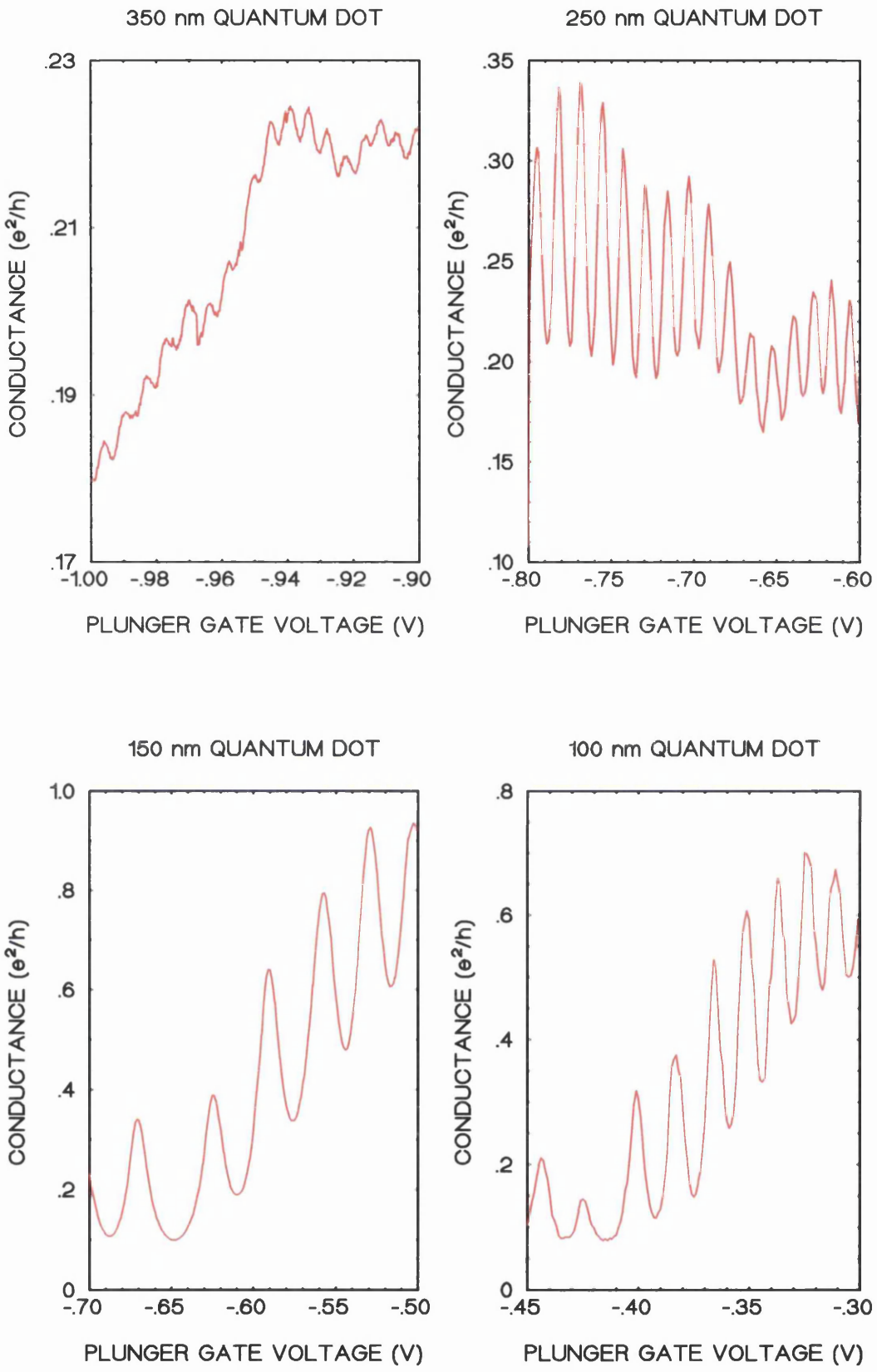

Figure 6.12: *Coulomb blockade oscillations for dots of nominal diameter 350 nm, 250 nm, 150 nm and 100 nm at a temperature of 1.2 K. The plunger gate voltage is varied, with all the other gates held at a fixed voltage.*

at 1.2 K. From Figure 6.11 it is clear that the Coulomb oscillations have the biggest amplitude and gate voltage period in case of the 150 nm quantum dot.

In the shallow 2DEG structures, the confinement potential forming the dot is much stronger than in deeper 2DEGs. Although this will lead to more widely spaced energy levels, analysis suggests that the classical charging energy accounts for most of the observed periodicity of the oscillations, with quantum corrections being small. Modelling showed that the electron pool at the centre of the dot may not be perfectly circular, but may have short protrusions into the areas between the gate fingers. This may contribute extra capacitance due to the accumulation of electric field lines at regions of higher curvature. For the 150 nm dot the potential is relatively smooth and the above effect has much less significance.

Thus in this chapter we showed that ultrasmall quantum dots fabricated on material where the 2DEG is less than 30 nm from the surface exhibit Coulomb oscillations at temperatures higher than is possible on standard depth 2DEGs. Dots with lithographic diameter of 150 nm show charging effects at temperatures up to 7.7 K. These higher temperatures are the result of the smaller size of dot that can be fabricated on the shallow material, and permit the study of single electron phenomena in semiconductor nanostructures without the need, for example, of a dilution fridge. This is also a step towards potential practical applications at relatively high temperatures.

References

1. P J van Bentum, R T Smokers, H van Kempen, Phys. Rev. Lett. **60**, 2543 (1988).

2. C Schöenberger, H van Houten, H C Donkersloot, Europhys. Lett. **20**, 249 (1992).

3. D J Paul, J R Cleaver, H Ahmed, T E Whall, Appl. Phys. Lett. **63**, 631 (1993).

4. L J Geerligs, V F Anderegg, P A Holweg, J E Mooij, H Pothier, D Esteve, C Urbina, M H Devoret, Phys. Rev. Lett, **65**, 771 (1990).

5. U Meirav, M A Kastner, S J Wind, Phys. Rev. Lett. **65**, 771 (1990).

6. J G Williamson, A A Staring, L P Kouwenhoven, H van Houten, C W Beenakker, C E Timmering, M Mabesoone, C T Foxon in *Proceedings, Nanostructures and Mesoscopic Systems,* edited by W P Kirk and M A Reed (Academic Press, San Diego, (1991).

7. A T Johnson, L P Kouwenhoven, W de Jong, N C van der Vaart, C J Harmans, C T Foxon, Phys. Rev. Lett. **69**, 1592 (1992).

8. Y Wang, S Y Chou, Appl. Phys. Lett. **63**, 2257 (1993).

9. T Fijisawa, Y Hirayama, S Tarucha, Appl. Phys. Lett. **64**, 2250 (1994).

10. S Nakata, Phys. Rev. B. **47**, 1679 (1993).

11. H Matsuoka, S Kimura, Appl. Phys. Lett. **66**, 613 (1995).

12. E B Foxman, U Meirav, P L McEuen, M A Kastner, O Klein, P A Belk, D M Abusch, S J Wind, Phys. Rev. B. **50**, 14 193 (1994).

13. Y Meir, N S Wingreen, P A Lee, Phys. Rev. Lett. **66**, 3048 (1991).

14. C W Beenakker, Phys. Rev. B **44**, 1646 (1991).

15. P L McEuen, E B Foxman, J Kinaret, U Meirav, M A Kastner, N S Wingreen, S J Wind, Phys. Rev. B **45**, 11419 (1992).

16. I O Kulik, R I Shekhter, Sov. Phys. JETP **41**, 308 (1975).

17. Z Borsosfoldi, M Rahman, I A Larkin, A R Long, J H Davies, J M Weaver, M C Holland, J G Williamson, Appl. Phys. Lett. **66**, 3666 (1995).

18. E B Foxman, P L McEuen, U Meirav, Ned S Wingreen, Yigal Meir, Paul A Belk, N R Belk, M A Kastner, S J Wind, Phys. Rev B 47, 10020 (1993).

Chapter 7

DC Source - Drain Bias Measurements

7.1 Introduction

DC source-drain bias measurements are used to identify the regimes of single-electron tunnelling and determine critical quantum dot parameters such as charging energy and single particle level separation. In addition to these parameters the DC source-drain bias measurement technique allows us to investigate the effects of the two tunnel barriers and the surface gates on the single-electron transport through the quantum dot.

Conductance studies have demonstrated that Coulomb interaction determines the behaviour of electron transport through mesoscopic electronic systems weakly coupled to two electron reservoirs. Early work[1,2] concentrated on revealing the excitation spectrum of the quantum dot and the effect of the coupling between the electron pool and the source/drain on the charging energy of the dot. Later work[3,4] showed how the excited states in the quantum dot provide additional transport channels and performed transport spectroscopy in a magnetic field to reveal that the magnetic field affects energy states not only in the dot but also in the gates surrounding the quantum dot by shifting their electronic states. Interesting results were presented in a recent work,[5] showing that spin selection rules strongly influence the electron transport in the quantum dot with a finite number of interacting electrons.

In this chapter we discuss the theory for transport spectroscopy and calculations for the Coulomb blockade boundary in surface-gated quantum dots. DC source-drain bias measurements on quantum dots with a diameter of 150 nm

are presented, with the aim of determining the energy level separations in them. As the quantum dots randomly changed states during the course of the source-drain bias measurements even when kept at constant 1.3 K, in most cases full characterisation of the quantum dots proved to be very difficult. In this section we present data on quantum dots which, at the time they were studied, had the biggest single particle energy level separations then reported.

7.2 Theory of the Coulomb Blockade Boundary

By coupling the quantum dot to two electron reservoirs with weak tunnel junctions allows the investigation of electron transport through the quantum dot. At low temperature, using low bias voltage between the source and drain reservoirs, the transport is normally suppressed due to lack of energy required to add an extra electron to the dot. The energy can be supplied by a metal gate capacitively coupled to the dot, thus allowing electrons to pass through the quantum dot. By varying the gate voltage and the source-drain bias voltage it is possible to perform transport spectroscopy on the quantum dot. In this regime the electrons pass through the quantum dot as the varied source-drain bias makes the excited states of the quantum dot accessible, providing additional transport channels. The equivalent capacitor circuit of the single quantum dot is depicted in Figure 7.1.

By sweeping the voltages, on the gates it is possible to change the number of electrons occupying the quantum dot. Plotting the maximas and minimas of the Coulomb blockade oscillations for different source-drain bias voltages as a function of the gate voltage, we get the so called "Coulomb diamond" which clearly shows the regions where the charge transfer through the dot is inhibited and the number of electrons in the dot is fixed. Using a theory[5] developed for one-dimensional tunnel structures, we find the free energy F of a system (quantum dot) arising from charge stored on various capacitors:

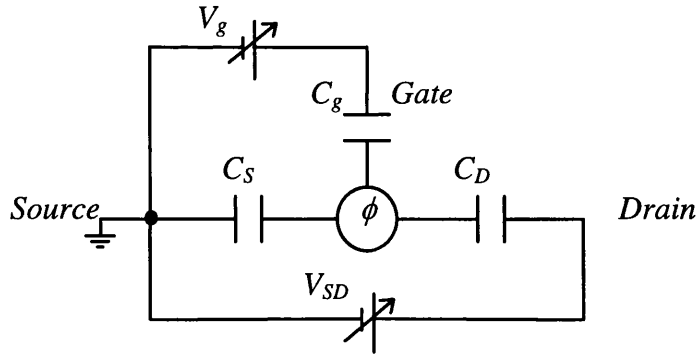

Figure 7.1 : *Schematic capacitor circuit of a single quantum dot indicating the capacitances of the dot to the source, drain and the gates (C_S, C_D, and C_g respectively). The electrostatic potential inside the dot is ϕ, and two voltage sources are used to vary the voltage both on the gates and between the source and drain. The tunnelling conductances onto the dot are assumed to have a small effect on the bias.*

$$F = \frac{C_S}{2}(V_S - \phi)^2 + \frac{C_D}{2}(V_D - \phi)^2 + \frac{C_g}{2}(V_g - \phi)^2 - V_D Q_D - V_S Q_S - V_g Q_g \quad (7.1)$$

where the charge on the drain, source and gate are

$$Q_D = C_D(V_D - \phi) + en_D$$

$$Q_S = C_S(V_S - \phi) + en_S \quad (7.2)$$

$$Q_g = C_g(V_g - \phi)$$

In Equation 7.2 n_D and n_S are the number of electrons which have passed from the drain to the dot and from the dot to the source respectively. The charge on the quantum dot can then be written:

$$Q = C_D(\phi - V_D) + C_S(\phi - V_S) + C_g(\phi - V_g) \quad (7.3)$$

In Equation 7.3 V_D, V_S and V_g are the voltages applied to the drain, source and the gates of the quantum dot respectively. The sum of the capacitances in the system is

$$C_\Sigma = C_S + C_D + C_g \tag{7.4}$$

Equation 7.3 may then be rewritten:

$$C_\Sigma \phi = Q + C_D V_D + C_S V_S + C_g V_g \tag{7.5}$$

Substituting Equations 7.2, 7.3 and 7.5 into Equation 7.1 we find the free energy difference in a system with N+1 and N electrons on the quantum dot, see Equation 7.6:

$$F_{N+1} - F_N = \frac{(2N+1)e^2}{2C_\Sigma} - \frac{e}{C_\Sigma}\left(V_D C_D + V_S C_S + V_g C_g\right) \tag{7.6}$$

similarly for the charge transition from N to N-1 electrons, see Equation 7.7:

$$F_N - F_{N-1} = \frac{(2N-1)e^2}{2C_\Sigma} - \frac{e}{C_\Sigma}\left(V_D C_D + V_S C_S + V_g C_g\right) \tag{7.7}$$

Two similar equations can be written for the source and drain transition[15]:

$$\begin{aligned} \left(N+\frac{1}{2}\right)e &= V_{gS} C_g + V_{DS} C_D \\ \left(N-\frac{1}{2}\right)e &= V_{gS} C_g - V_{DS}\left(C_\Sigma - C_D\right) \end{aligned} \tag{7.8}$$

From these two equations the Coulomb blockade boundary can easily be determined. The two slopes of the boundary in the V_{DS}/V_{gS} plane are given by Equation 7.9:

$$A = \frac{C_g}{C_\Sigma - C_D} \qquad \text{and} \qquad B = -\frac{C_g}{C_D} \tag{7.9}$$

The stability diagram of a quantum dot is shown in Figure 7.2. The quantum dot conducts only outside the rhombic shaped regions. Inside these regions the dot does not conduct, the number of electrons is fixed, all transitions are suppressed by a Coulomb blockade and no current flows through the quantum dot[6]. From Equation 7.9 it is apparent that mainly the ratio of C_S/C_D determines the gradients of the Coulomb blockade boundaries, depicted in Figure 7.2.

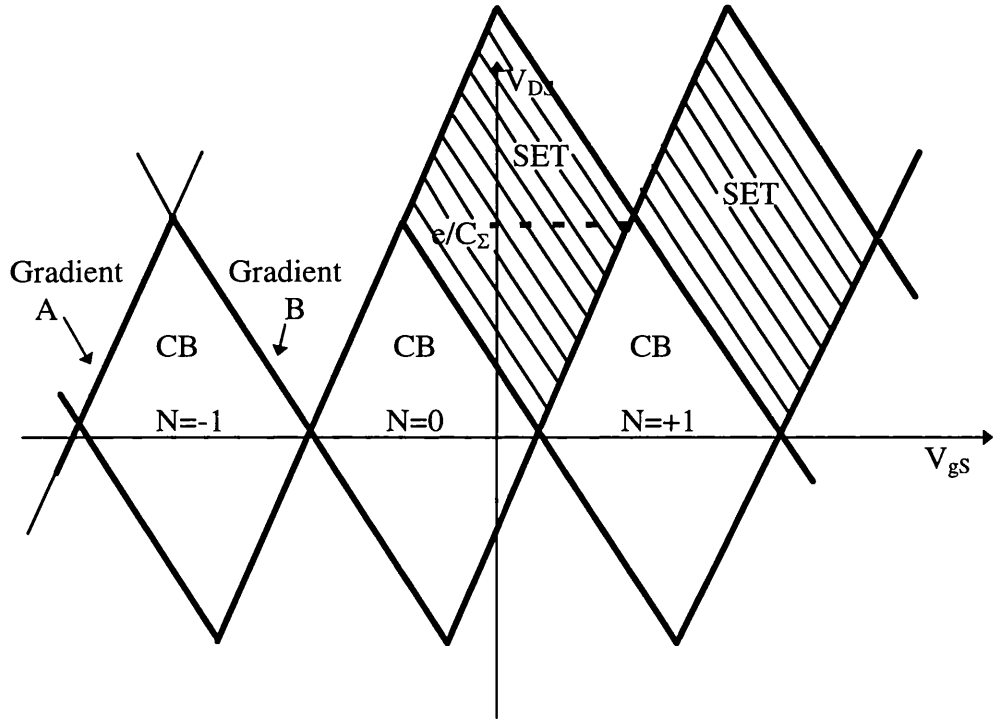

Figure 7.2 : *The stability diagram of a quantum dot system, when the dot is capacitatively coupled to the source, drain and the surrounding gates. The quantum dot conducts only outside the rhombic-shaped regions indicated by CB (Coulomb Blockade). Inside the regions the number of electrons in the dot is fixed, electron transport through the dot is blockaded. In the rhomboids indicated by SET (Single Electron Tunnelling) the electrons pass through the dot one by one.*

Using the maximum value of the rhomboids along the Y axis we can directly determine C_Σ and the energy level separation inside the quantum dot for specific number of electrons in it.

The boundaries of the Coulomb blockade for a specific quantum dot can be determined by plotting the minimas and maximas of the Coulomb blockade oscillations for a given DC source-drain bias voltage range (normally between -5 and +5 meV, which value is expected to exceed the energy level separation between consecutive energy levels inside the quantum dot) as a function of a gate voltage. Thus in the source-drain bias experiments the differential conductance versus V_{gS} is plotted at different V_{DS}. In these experiments, when at a given V_{DS} the differential conductance (vs. V_{gS}) crosses the boundaries of the rhomboids one gets a conductance peak, see Figure 7.2.

Because of the finite charging energy, the number of electrons in the quantum dot can change only by one at a time in the transport regime neighbouring the blockaded regime, see Figure 7.2. This is called the regime of single-electron tunnelling (SET). The quantum dot changes between the ground states of two electron systems (between an *N* and an *N+1* electron system). At finite source-drain bias voltage, excited states for both electron systems become accessible, providing new tunnelling channels through the quantum dot. Based on the number of barriers in the quantum dot we have two possibilities: a new channel opens at the source side or a new channel opens at the drain side. In the first case an excited state of the *N+1* electron system becomes accessible for placing the *N+1th* electron from the source to the n electron system in the quantum dot. In the second case, the quantum dot is left in an excited state of the n electron system as the *N+1th* electron leaves the quantum dot to an unoccupied state in the drain. Usually both kind of channels are visible in a DC source-drain bias plots as an additional structure within one SET regime.[3]

Generally in quantum dots the tunnelling barriers separating the dot from the source and drain have different tunnelling probabilities. In contrast to the more symmetric case, where the opening of new channels at both barriers has the same importance, in asymmetric quantum dots the conductance through the quantum dot is dominated by the thick barrier. If the thick barrier is at the source side, the quantum dot is preferably filled with *N-1* electrons and thus transitions

from the *N-1* to the *N* electron system dominate the transport regime. If the thick barrier is at the drain side the quantum dot spends most of its time filled up to *N+1* electrons. In this case transitions from the *N+1* to the *N* electron system dominate the electron transport through the quantum dot.

7.3 Measurements

Four quantum dots were measured, each with a nominal diameter of 150 nm. The measurements were performed repeatedly on each quantum dot when the device characteristics showed the most stable behaviour. The measurements in two devices containing very few electrons revealed striking characteristics, enabling us to carry out transport spectroscopy measurements. These two few electron quantum dots will be discussed in more detail in the following chapter.

7.3.1 150 nm Quantum Dot Z212B

This 150 nm quantum dot was measured in a wide range of positive and negative DC source-drain bias. The positive DC characteristics exhibit variation of the electrical potential during the characterisation see Figure 7.3.

At low positive DC bias at around -0.41 V gate bias the magnitude and position of the Coulomb blockade oscillations show random behaviour. At more positive DC bias and less than -0.44 V gate bias voltages the oscillations become more periodic. The conductance peaks in this measurement persisted even at 6 mV DC source-drain bias, indicating a large energy level separation in this quantum dot, see Figure 7.4.

The Coulomb oscillations tend to die out at more negative gate voltages than around -0.46 V, when the conductance of the quantum dot goes to zero. This quantum dot showed similar DC bias characteristics in the negative DC bias range, see Figure 7.5. The oscillation peaks also show changing behaviour in the

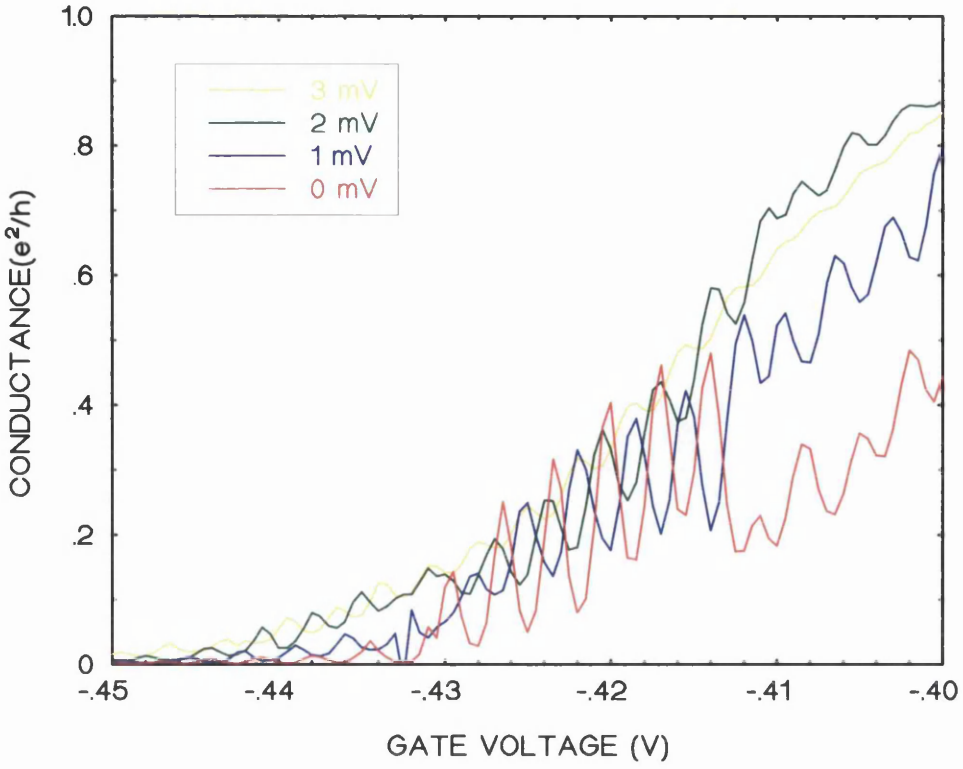

Figure 7.3 : *Conductance oscillations under different DC source-drain bias.*

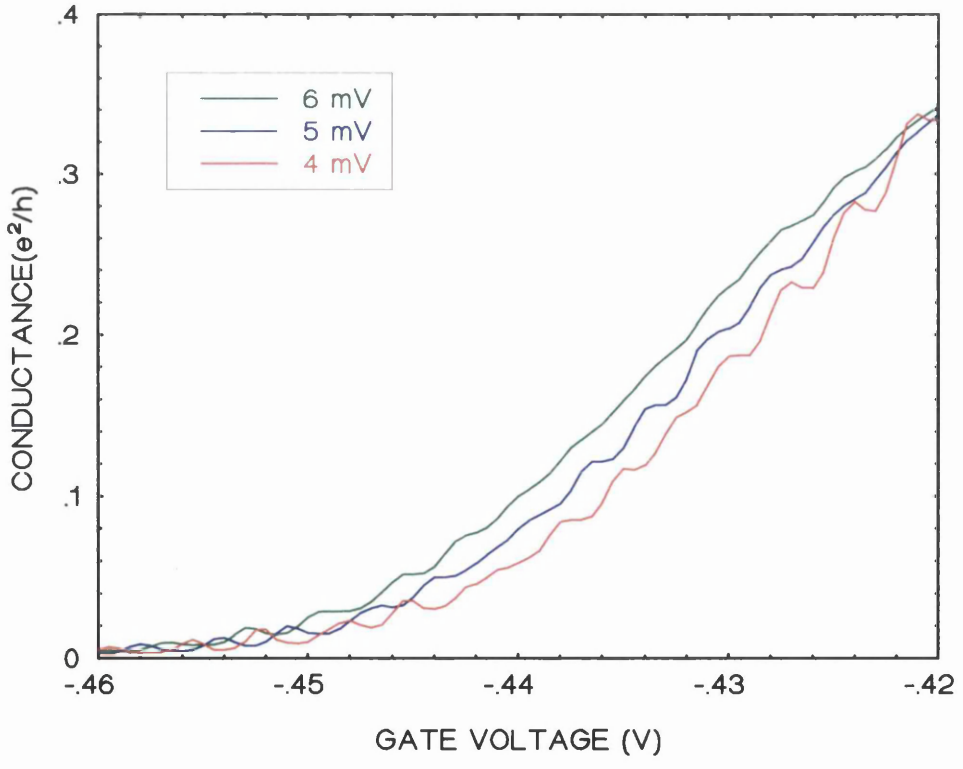

Figure 7.4 : *Coulomb oscillation peaks persist at 6 mV DC source-drain bias.*

same gate voltage range. The Coulomb blockade peaks persist at very high negative DC biases, see Figure 7.6. There is little change in the period and the amplitude of oscillations, but the oscillation peaks shift towards more negative gate voltages with increasing DC bias.

The electrical field distributions in small quantum dots fabricated on shallow 2DEG materials tend to change during the course of measurement and the dots generally change states during their operation, resulting from background charges. The above curves were recorded in a nominally similar state (State 2) of the dot. The DC source-drain bias characteristics in quantum dot Z212B in State 3 after a discontinuous change are shown in Figure 7.7. The shape and period of oscillations have changed and the curves shifted towards more negative gate voltages.

The DC bias oscillations below -1 mV DC bias and between -0.3 – -0.325 V gate voltage show rather different behaviour, exhibiting itself in the broadening of the conductance curves. This phenomenon is less apparent in the positive DC bias curves, probably due to altered bias conditions on either side of the quantum dot.

By plotting the maximas of the oscillations as a function of the gate voltage at different DC source-drain biases, the Coulomb-diamond of the single electron regime can be formed based on the single electron transport regime boundary conditions. Inside the Coulomb diamonds the electron transport regime is blocked by the Coulomb blockade, electrons can pass through the dot only outwidth the Coulomb diamond in the single electron tunnelling regime. As the four surface gates in quantum dot Z212B were interconnected the electron transport through the dot could not be controlled to properly balance the point contacts on either side of the dot, thus the Coulomb diamond was not formed, see Figure 7.8.

As expected from the rapidly changing oscillations the maxima plot results in straight lines revealing the shift of oscillation curves.

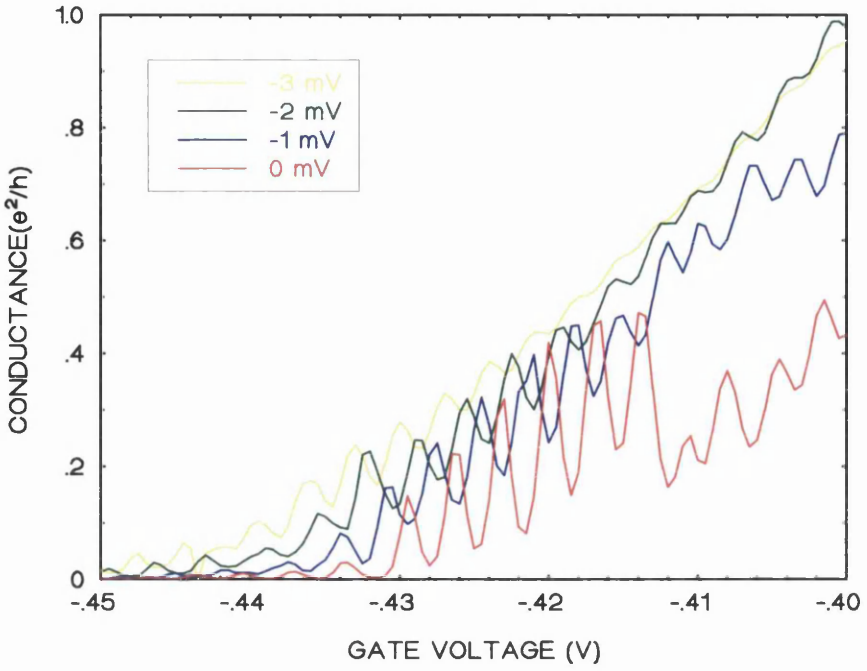

Figure 7.5 : *Quantum dot Z212B in 0 – -3 mV DC source-drain bias voltage range.*

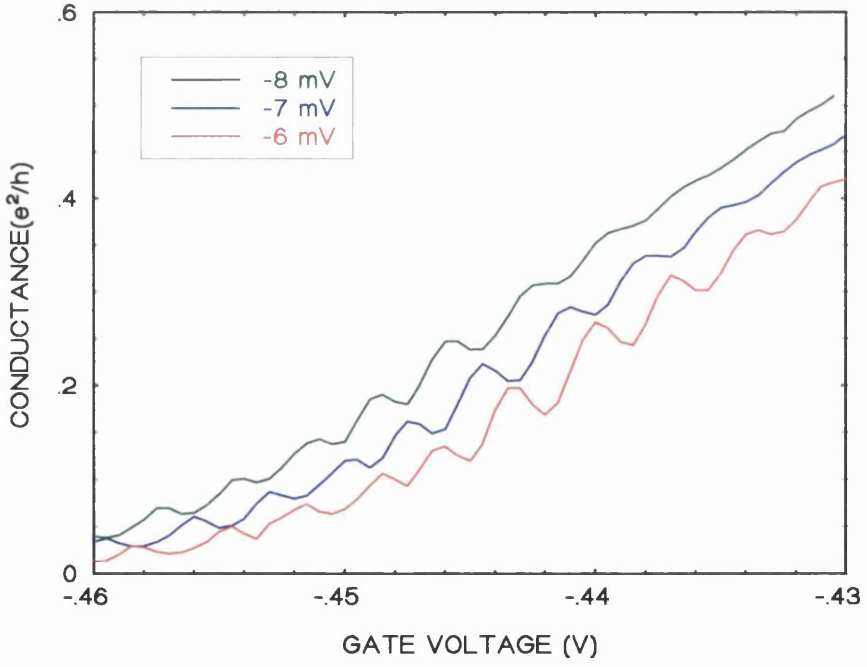

Figure 7.6 : *Oscillation peaks in the -6 – -8 mV DC bias voltage range. Note the shift of curves towards more negative gate voltage with increasing DC source-drain bias.*

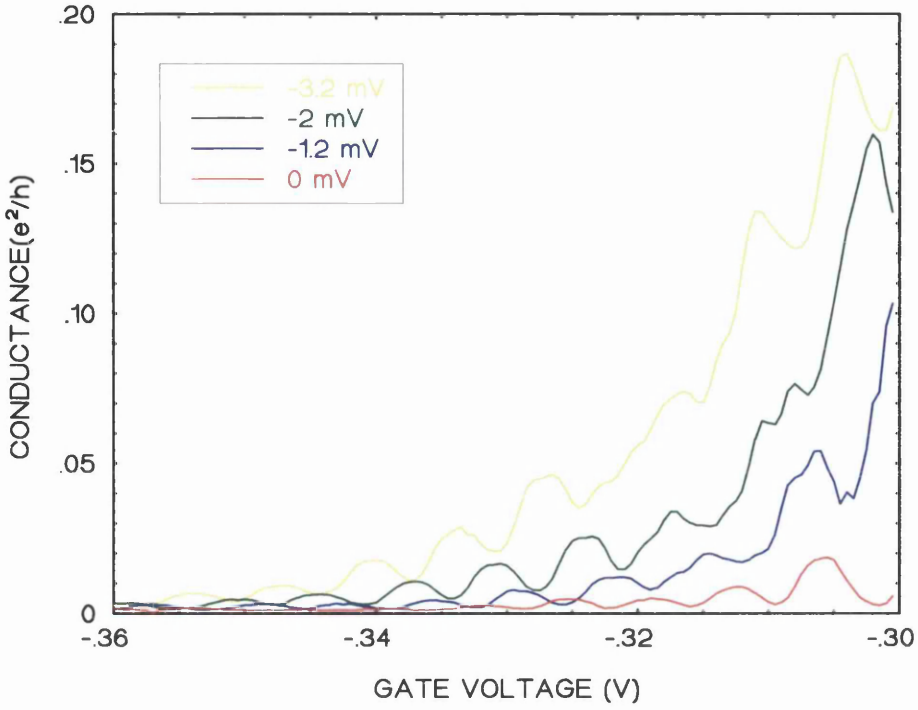

Figure 7.7 : *State 3 of quantum dot Z212B. Note the change in the amplitude and period of the oscillations.*

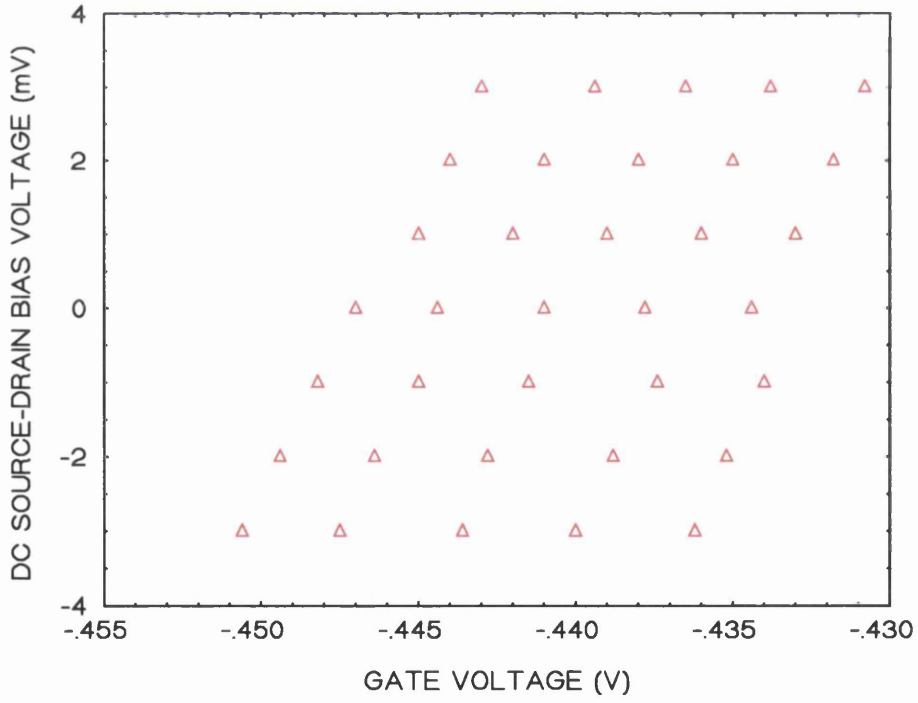

Figure 7.8 : *Plot of conductance maximas as a function of gate voltage at different DC source-drain bias.*

7.3.2 150 nm Quantum Dot SALSA

State 1

The change in the electrostatical landscape in and around this quantum dot during the course of measurements resulted in the change of DC source-drain characteristics. In State 1 the dot showed three Coulomb oscillations the conductance reaching near zero value at -0.6 V gate bias. The Coulomb diamond for the last two conductance peaks is shown in Figure 7.9. The two Coulomb diamond in the positive DC bias range show rapidly changing oscillation peak structure.

The two halves of the Coulomb diamonds in positive and negative DC are not aligned indicating that between the measurement series a change of charge configuration has taken place and the dot has reached a different state. The characteristic capacitance values for the quantum dot can be calculated from the gradients of the Coulomb diamond's boundaries. These values for the indicated boundaries from Figure 7.9 are :

$$C_{g0} = (2.37 \pm 0.19)\ 10^{-18}\ \mathrm{F}$$
$$C_{g} = (1.34 \pm 0.11)\ 10^{-17}\ \mathrm{F}$$
$$C_{S} = (2.28 \pm 0.18)\ 10^{-18}\ \mathrm{F}$$
$$C_{D} = (3.82 \pm 0.31)\ 10^{-17}\ \mathrm{F}$$
$$C_{\Sigma} = (5.36 \pm 0.43)\ 10^{-17}\ \mathrm{F}$$

where C_{g0} is the capacitance between the quantum dot and the swept gate, C_g is the capacitance between the dot and all the gates surrounding the dot and C_Σ is the capacitance between the quantum dot and its environment. The changes of gradients of the SET regime boundary in the positive DC bias indicate that the capacitative coupling of the quantum dot to its surroundings changes significantly while the central gate voltage is swept. This is likely due to the change of the shape of the electron pool inside the quantum dot.

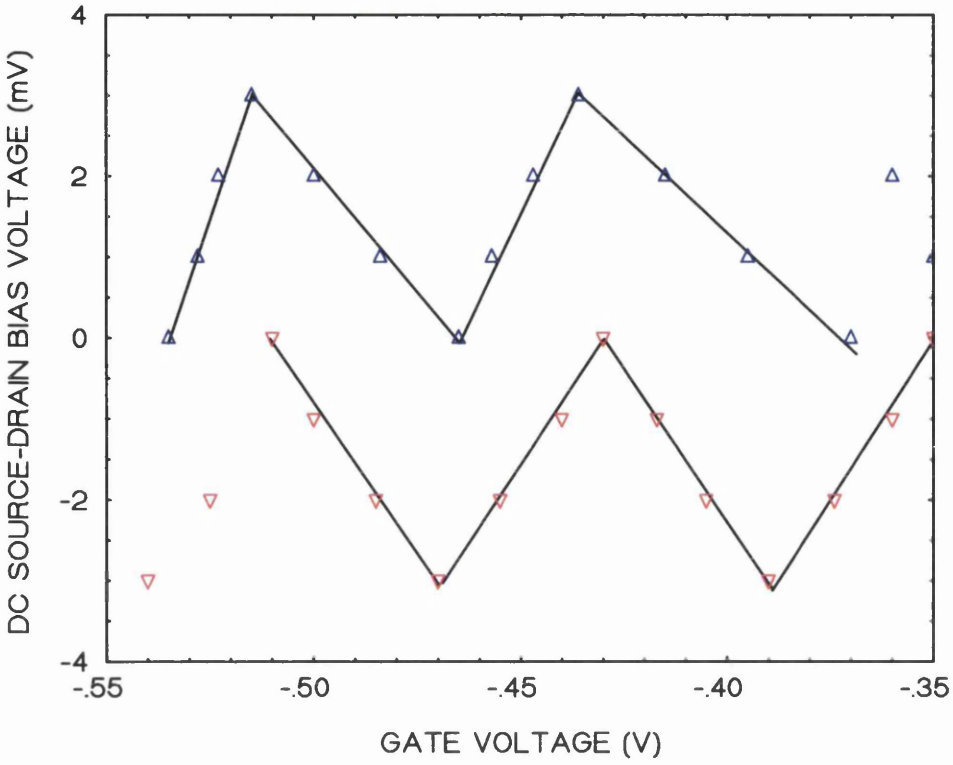

Figure 7.9 : *DC source-drain characteristics in quantum dot SALSA in State 1. (The lines on the graph are for indication only.)*

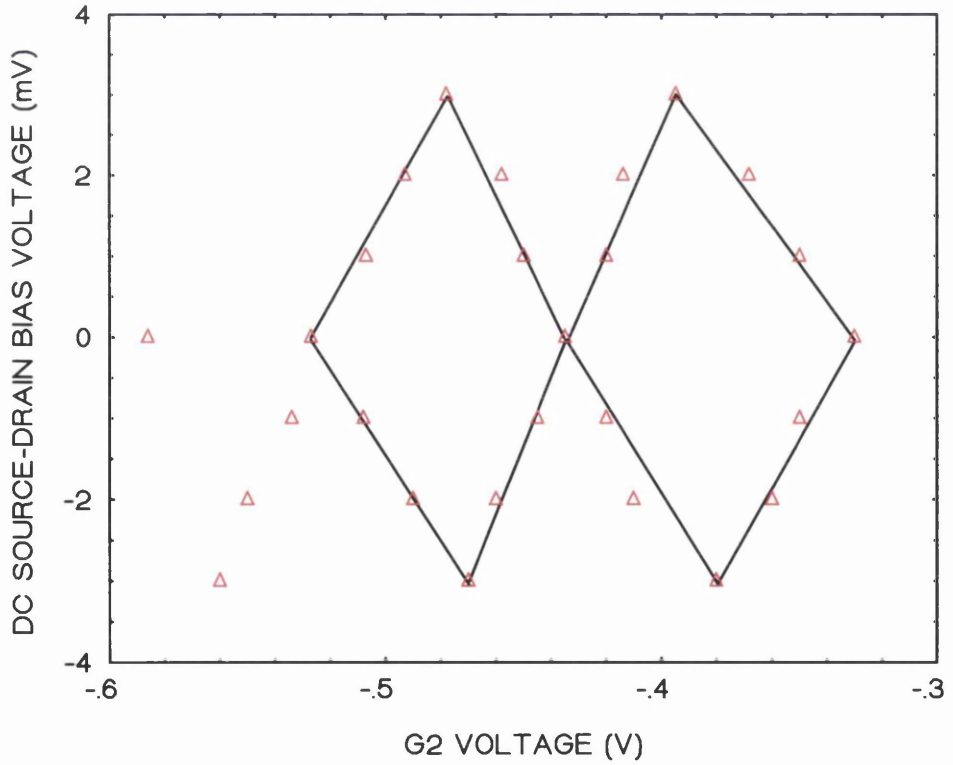

Figure 7.10 : *DC characteristics of dot SALSA in State 2.*

The significant difference between C_S and C_D indicates that the quantum dot is not equally balanced during the DC source-drain bias measurement although both sets of oscillation peaks are visible.

State 2

The DC source-drain characteristics of the quantum dot in State 2 showed more regular behaviour than in State 1. The positive and negative halves of the DC characteristics formed a relatively well balanced Coulomb diamond, see Figure 7.10. The maximum DC value of the diamond is 3 mV indicating similar single particle energy level separation but different energy level structure inside the quantum dot.

As the quantum dot in State 2 was more stable than the previous state and better balanced the capacitance values between the dot, source and drain show more symmetrical behaviour. The capacitance values in this dot were as follows:

$$C_{g0} = (1.74 \pm 0.14)\ 10^{-18}\ \text{F}$$
$$C_g = (1.78 \pm 0.14)\ 10^{-17}\ \text{F}$$
$$C_S = (1.06 \pm 0.09)\ 10^{-17}\ \text{F}$$
$$C_D = (2.49 \pm 0.2)\ 10^{-17}\ \text{F}$$
$$C_\Sigma = (5.33 \pm 0.43)\ 10^{-17}\ \text{F}$$

The comparable capacitance values between the quantum dot, source and drain indicates that the dot was symmetrically balanced during the course of the DC source-drain bias measurements.

State 3

The conductance oscillations in the quantum dot in State 3 show more irregular behaviour compared to that in State 1 and State 2, as at this point the device started to deteriorate, probably due to charge build-up and measurement stress. The conductance oscillations smear out at 2 mV in the positive DC source-

stress. The conductance oscillations smear out at 2 mV in the positive DC source-drain bias range while the same value is -3 mV in the negative DC bias range. This indicates that the quantum dot changed its behaviour during the measurement and then bounced back to the 'regular' state, see Figure 7.11.

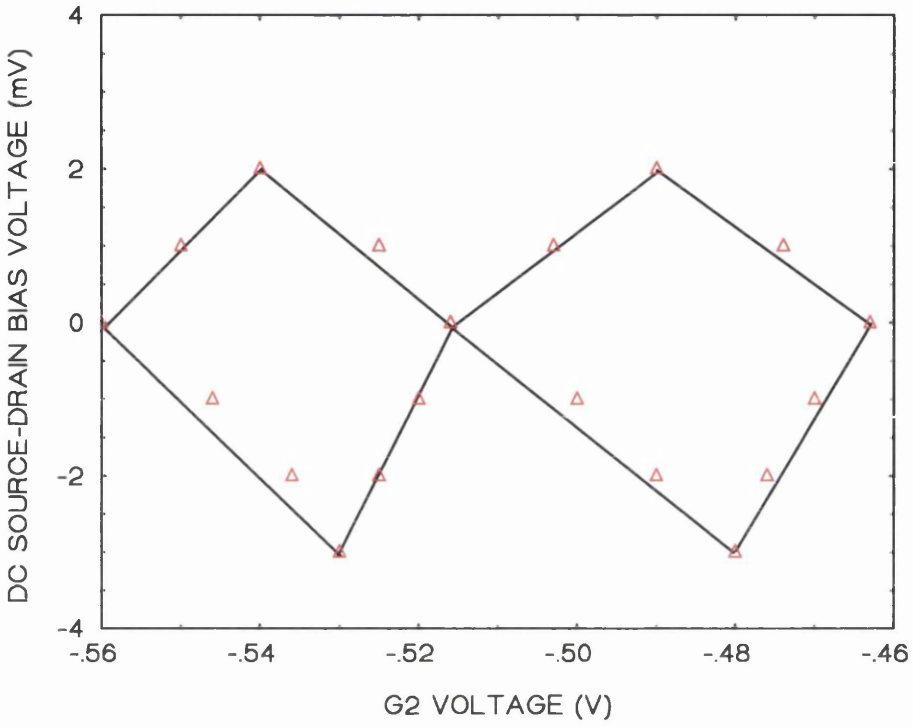

Figure 7.11 : *DC source-drain characteristics of quantum dot SALSA in State 3.*

In this state the two Coulomb diamonds are quite identical, the SET regime boundaries in the negative and positive DC regions have roughly similar gradients. The oscillation peaks in the positive and negative DC range do not shift significantly as the positive and negative halves of the two Coulomb diamonds are relatively well aligned. The capacitance values derived from the positive DC regime of the indicated Coulomb diamond are as follows :

$$C_{g0} = (3.56 \pm 0.29)\ 10^{-18}\ \text{F}$$

$$C_g = (2.67 \pm 0.21)\ 10^{-17}\ \text{F}$$

$$C_S = (0.91 \pm 0.07)\ 10^{-17}\ \text{F}$$

$$C_D = (4.45 \pm 0.36)\ 10^{-17}\ \text{F}$$

As in the previous states the source and drain capacitances are unbalanced, similarly to the capacitance values in State 1 and State 2. The peculiar feature of this DC source-drain data is the difference between the positive and negative maximum DC value of the Coulomb-diamond which may be due to the rearrangement of trapped charge on the surface of the semiconductor. A serious degradation in the device characteristics did not enable us to carry out further measurements on this quantum dot.

7.4 Conclusions

By applying a DC source-drain voltage to the AC excitation voltage, it is possible to determine the energy states of the quantum dot as they pass by the energy difference between the source and drain μ_S-μ_D. In addition to this the single particle energy level separation, one of the main characteristics of a quantum dot can be determined. By plotting the conductance maximas as a function of the gate voltage at different DC source-drain bias voltages the so called Coulomb diamond can be constructed. Each Coulomb diamond represent one electron in the quantum dot where the boundaries of the diamond separates the blockaded regime inside the dot, when the number of electrons inside the dot is constant, from the SET regime outside the diamond. In the SET regime single electrons pass through the dot one by one when the necessary energy for electron transport is supplied by means of the DC bias.

In all the measured quantum dots the period of oscillations varied during the course of the measurement when the dot was warmed up and subsequently cooled down. The period and phase of the oscillations changed somehow randomly from sample to sample, and for the same sample when the temperature was varied, which we ascribe to the change of position of charged defects and impurities in the sample. Some samples changed their state randomly at different times even at a constant 1.2 K. Several quantum dots exhibiting clear Coulomb diamond structures were measured. The maximum value of the single particle

energy level separation was 3 meV in all quantum dots except for quantum dot SALSA in State 3 with 2 meV.

The variations in the period of the oscillations is reflected in the change of the steepness of the SET regime boundaries which determine the level of capacitative coupling of the quantum dot to the source and drain. The level of capacitative coupling between the dot and its surrounding varies from conductance peak to conductance peak, indicating the likely presence of impurities in and around the quantum dot.

The above measurements indicate that in semiconductors with shallow 2DEGs, the closeness of the 2DEG to the surface of the semiconductor makes the electron transport very vulnerable to the effects of the proximity of the δ-doped layer to the channel. The presence of impurities and charged defects in the sample cause significant variation in the device's characteristics, making the DC source-drain measurements difficult to carry out in shallow 2DEG semiconductor structures.

References

1. J H Scott-Thomas, S B Field, M A Kastner, H I Smith, D A Antoniadis, Phys Rev. Lett, **62** 583 (1989).

2. E B Fav, N S Wingreenoxman, P L McEuen, U Meir, Y Meir, P A Belk, N R Belk, and M A Kastner, Phys. Rev. B **47**, 10020 (1993).

3. J Weis, R J Haug, K von Klitzing, K Ploog, Phys Rev Lett. **71**, 4019 (1993).

4. J Weis, R J Haug, K von Klitzing, K Ploog, Semicond. Sci. Technol. **9**, 1890, (1994).

5. N S Bakhalov, G S Kazacha, K K Likharev, S I Serdyukova, Sov. Phys. JETP **68**, 581 (1989).

6. Single Charge Tunnelling, Coulomb Blockade Phenomena in nanostructures edited by H Grabert and M H Devoret, Plenum Press, London (1992).

7. E Castano, G Kirczenow, Phys. Rev. B **45**, 1514 (1992).

8. H van Houten, C W J Beenakker , A A M Staring, Phys. Rev. B **45**, 9222 (1992).

9. Y Meir, N S Wingreen, Phys. Rev. Lett. **68**, 2512 (1992).

10. M I Ruzin, V Chandrasekhar, E I Levin, L I Glazman, Phys. Rev. B **45**, 13469 (1992).

11. K A Matveev, A I Larkin, Phys. Rev. B **46**, 15337 (1992).

12. S Hersfield, J H Davies, P Hyldgaard, C J Stanton, J W Wilkins, Phys. Rev. B **47**, 1967 (1993).

13. R C Ashoori, H L Stormer, J S Weiner, L N Pfeiffer, K W Baldwin, K W West, Phys. Rev. Lett. **71**, 613 (1993).

14. A L Efros, F G Pikus, V G Burnett, Phys. Rev. B **47**, 2233 (1993).

15. A R Long, (unpublished).

Chapter 8

Spectroscopy of Quantum Dots with Few Electrons

8.1 Introduction

Numerous experimental[1] and theoretical[2-4] studies have been carried out on spectroscopy of quantum dots with varying number of electrons. These zero-dimensional structures can be thought of as artificial atoms where the confining potential replaces the potential of the nucleus. The typical dot size is about 100 nm and contains between 2 and 200 electrons. Rapid advances in semiconductor technology have gradually made it possible to reduce the size of the quantum dots thus reduce the number of electrons in it. Most experimental work has been done on quantum dots containing at the lowest between 10-30 electrons mainly due to limitations in nanofabrication technology. The use of novel fabrication technologies in the past few years has enabled experimental physicists to fabricate easily controllable quantum dots containing fewer than ten electrons.[5] This has made it possible to test experimentally the theoretical calculations on electron distribution and critical quantum dot features in dots with very few electrons.

8.2 Electron Spectroscopy in Quantum Dots with Few Electrons

The electron distribution, energy level distribution and other characteristic features in quantum dots can be calculated using the artificial atom approach, when the charge of the quantum dots can be controlled at the single-electron level. The lateral confinement potential which binds the electrons to the quantum dot is created by spatially extended charge distributions. The single-electron spectroscopy can be done different ways, mainly using capacitance, optical or transport spectroscopy.

Quantum dots in semiconductor heterostructures exhibit a discrete energy level spectrum, easily observable at a very low temperature. Experiments on few-electron quantum dots exhibit only a sparse excitation spectrum with relatively large energy level spacings. In recent theoretical work[9] it has been shown that in quantum dots with few electrons the strong Coulomb interaction microscopically affects the period and structure of the conductance oscillations.

For semiconductor quantum dots, two idealistic models are spherical quantum dots in three-dimensional space with a rectangular potential and circular quantum disks in two-dimensional space with a parabolic potential. However, a realistic quantum dot usually deviates from spherical and circular ones while its confinement potential usually deviates from square and parabolic ones. A systematic investigation can reveal the dependence of confined electron states in zero dimensional quantum dots with asymmetry on the potential shape and quantum size.

The transport properties of a two-dimensional quantum dot coupled to two reservoirs by tunnelling barriers can be described with the conventional tunnelling Hamiltonian approach.[6,7]

The Hamiltonian of the system is the sum of the Hamiltonian of the dot H_D, the Hamiltonian of the reservoir H_R, and the tunnelling term H_T. The tunnelling Hamiltonian describes the electron transfer from the reservoir to the quantum dot where the Coulomb interactions are most important.

The energy level distribution inside the quantum dot with few electrons can be obtained from the numerical diagonalisation of the quantum dot Hamilton operator see Equation 8.1[9].

$$H_D = \sum_n \varepsilon_n d^\dagger_n d_n \quad + \sum_{n,m,n',m'} V_{nmn'm'} d^\dagger_n d^\dagger_m d_{n'} d_{m'} \tag{8.1}$$

where

$$\varepsilon_n = \hbar\Omega_+(N_+ + 1/2) + \hbar\Omega_-(N_- + 1/2) \tag{8.2}$$

are the single particle energies with

$$\Omega_\pm = (\sqrt{4\Omega_0^2 + \omega_c^2} \pm \omega_c)/2 \tag{8.3}$$

In Equation 8.3 Ω_0 characterises the confining potential and $\omega_c=eB/mc$ is the cyclotron frequency, in Equation 8.1 $V_{nmn'm'}$ are the interaction matrix elements for the usual $1/\varepsilon r$ Coulomb potential with the dielectric constant ε. Equation 8.1 describes a rigid harmonic potential influenced by occupation which is unlikely to be realised in practice.

Taking into consideration sequential tunnelling only, the current through the quantum dot is given by[6]

$$\begin{aligned} I = -e \sum_{\alpha\alpha'} \Gamma_{\alpha\alpha'} [P(N,\alpha)\alpha + P(N-1,\alpha')] \\ *[f(\Delta E_{\alpha\alpha'} - \mu_l) - f(\Delta E_{\alpha\alpha'} - \mu_r)] \end{aligned} \tag{8.4}$$

In Equation 8.4 $\Gamma_{\alpha\alpha'}$ is the tunnelling rate through the quantum dot, $P(N,\alpha)$ is the probability of finding the quantum dot in the N-particle state α. $\Delta E_{\alpha\alpha'}=E(N,\alpha)-E(N-1,\alpha')$ is the resonant energy indicating the energy difference between N-particle state α and $(N-1)$-particle state α'. The Fermi-Dirac distribution function f characterises the occupation of electron levels in the source and the drain (electrochemical potential μ_S and μ_D respectively).

The energy level separations and distribution depend strongly on the number of electrons in the quantum dot.[3] If the number of electrons in the quantum dot is between 1-10 the energy levels show an electron shell structure, between 30-40 electrons the energy levels are roughly equally separated, dominated by the charging energy. The shell structure can be explained by the degeneracy of the single electron energy level: when the first electron enters the dot it occupies the first energy level which is empty. The second electron also occupies this energy level with opposite spin, but the energy level will be pushed up by the Coulomb repulsion. The third electron is forced to occupy the next higher energy level. As the first two electrons occupy the same level the Coulomb repulsion between them is stronger than that between the third electron and the rest. As a result the gap between the second and third energy level is smaller than that between the first and second energy level.

As the number of electrons in the dot increases, the Coulomb interaction becomes increasingly dominant and the energy levels are more and more in balance self consistently, so the gaps between the energy levels decreases and the degeneracy of the single electron energy level is smeared out. This effect is observable in the conductance oscillations which exhibit a transition from relatively aperiodic to periodic oscillations as the number of electrons in the dot increases. The observed conductance oscillations are not perfectly periodic as there is a certain difference for a given electron occupation range which reflects the difference between the energy gaps inside the quantum dot.

Measurements in quantum dots containing up to 40 electrons[3] showed that a pair structure appears in the Coulomb oscillation peak heights reflecting the even- and odd occupation numbers and the double degeneracy of two spin freedoms. A pair structure can also be detected in the oscillation peak linewidths. An even occupation number gives a zero total spin when every state has two electrons and their wave functions completely overlap which state is similar to that of the closed shell atom or nucleus.

In quantum dots containing less than 10 electrons spectroscopy can be employed to investigate the behaviour of single electron transport and the change of single particle energy level spacing. As described in Chapter 5, the quantum dots can be approximated by a single circular electrode and using a specific

method[7] it can be determined that the curvature of the electrostatic potential in the centre of the dot at complete depletion is a maximum for a ratio of dot radius to electron depth of $\sqrt{3}$, assuming a frozen semiconductor surface. For our quantum dots this suggests a diameter of approximately 120 nm. Theoretical and experimental studies also show that surface gated quantum dots between 100 and 150 nm in nominal diameter have the biggest energy level spacing thus these dots work in the high temperature regime for the electron depth we use, see Chapter 5. Maximum single particle energy spacing and the highest achievable operational temperature were the main aim of our work thus most measurements and modelling were carried out on quantum dots containing few electrons.

Transport measurements through the quantum dots containing few electrons were made at 1.2 K and above, as the spacing of conductance peaks is adequate for them to be resolved at this temperature (when the dots are almost fully depleted). The differential conductance between either side of the quantum dot (source and drain) was studied for different gate voltage combinations, and for finite constant DC source-drain voltages. Measurement were also carried out in modest perpendicular magnetic fields (<3 T).

8.3 Measurements

The data on two quantum dots whose gate voltage characteristics revealed only a few peaks are given in Table 1. The gate voltage characteristics of quantum dot SALSA are shown in Figure 8.1. The electrostatic potential is swept by means of the centre gate *G2*, and the gate voltage characteristic is shifted in both samples by varying the voltages on the other three gates.

The characteristics of quantum dot SALSA show two broad conductance peaks with some indication of a third. Quantum dot Z212A fabricated on a different material was broadly similar in its behaviour, as described in Chapter 7. At more negative values of the centre gate voltage, little sign of any further peaks above the noise floor (around 10^{-4} e^2/h) was found for either of the two samples. The presence of further electrons remaining in the dot at large negative gate

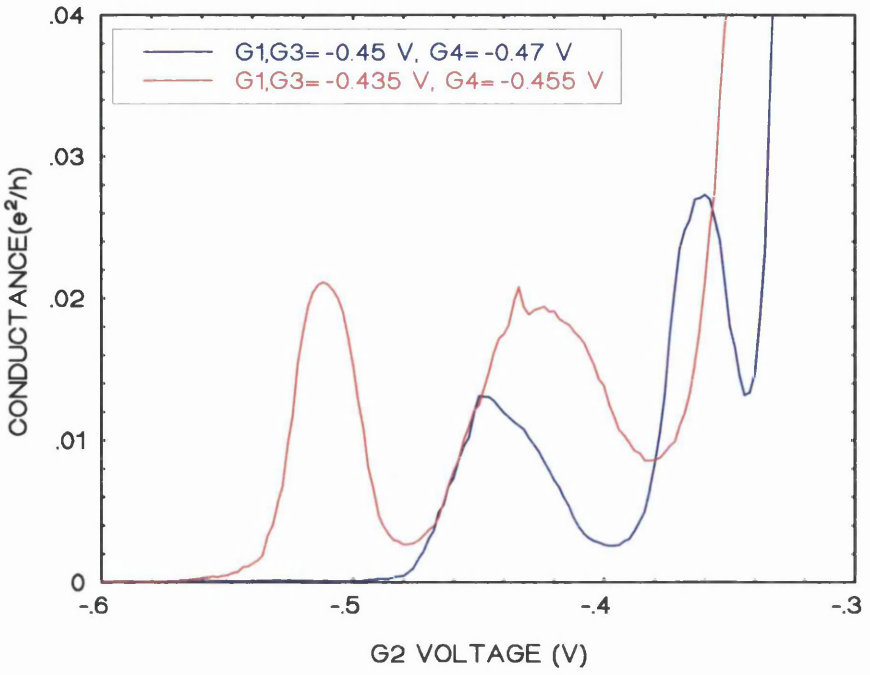

Figure 8.1: *Conductance of quantum dot SALSA as a function of G2 voltage, measured at 1.3 K. The parameters are the voltages applied to the other three gates G1, G3 and G4.*

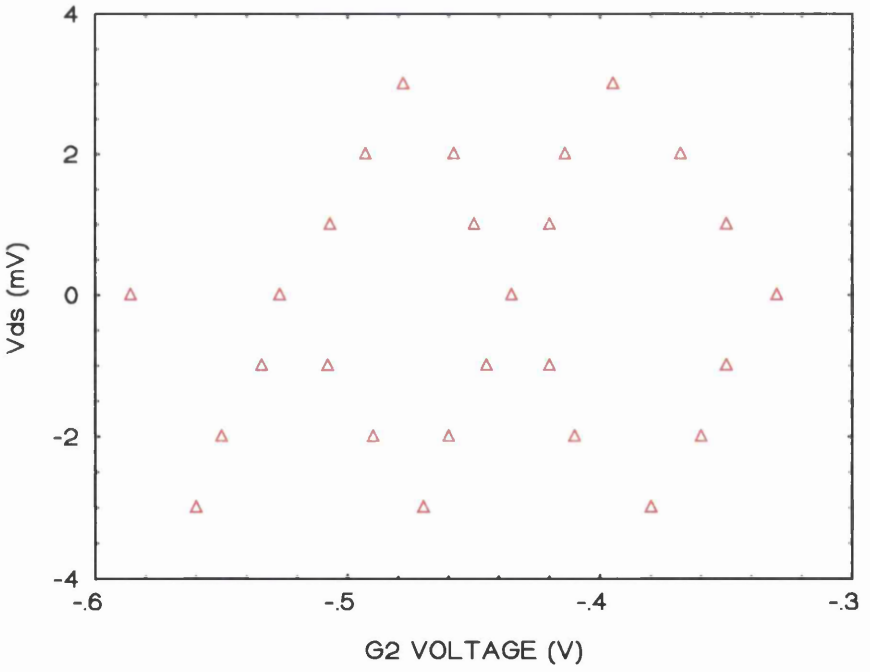

Figure 8.2: *The positions of the conductance peaks in dot SALSA as a function of DC source-drain bias, measured at 1.3 K.*

voltages cannot be excluded but they must be tightly bound and undetectable in the tunnel current.

From the voltage shift data, the voltage period between the major conductance peaks for applying bias to different combinations of gates can be determined. The ΔV_g values quoted in Table 1 are for varying bias applied to all gates in the dot simultaneously.

	Z212A	*Z212B*	*SALSA*
2/4 Gate	4	4	4
Material	A866	A866	A912
Carrier density $(10^{15}m^{-2})$	4.3	4.3	5.6
Diameter (nm)	150	150	150
ΔVg *(mV)*	12	3.5	16
Slope $s=dVg/dV_{SD}$	1.7	2.1	2.1/3.7
$\Delta E12$ *(meV)*	3.2	3.4	3.3/3.1
$\alpha=\Delta E/e\Delta V_g$	0.27	0.28	0.27

Table 8.1: *Parameters of 150 nm quantum dots Z212A and SALSA.*

The last row in Table 1 shows factor $\alpha=\Delta E/e\Delta Vg$ for all three quantum dots which relates a change in *Vg* to a shift in the charging energy of the dot. In a quantum dot with large number of electrons factor α can change from peak to peak in the Coulomb oscillations with varying charging energy and peak to peak separation. Factor α in case of the quantum dots in Table 1 with identical design, nominal diameter and with very few electrons when the dot is less strongly coupled to its source and drain does not exhibit this strong variation.

Further measurements were carried out to verify that these peaks arise from the Coulomb blockade. The energy parameters for the quantum dots were determined[20] by applying a variable DC bias between source and drain, and measuring the differential conductance characteristics, see Chapter 7. The DC

bias causes peak shifts which may be used to determine the energy differences ΔE between energy levels in the dot. In all this biased data, the peaks corresponding to the electron energy level in the dot passing through the Fermi level in the drain are dominant, and the slope marked *s* gives the rate of change of this peak voltage with V_{DS}. For quantum dot SALSA two values, s_1 and s_2 are given corresponding to the interchange of source and drain connections. Using these slopes and assuming the capacitance model for the response of the dot[19], see Chapter 7:

$$\Delta E = e\Delta V_g / (s_1 + s_2 - 1) \tag{8.5}$$

This gives the first ΔE value for SALSA quoted in Table 1. In the above two samples the separation of the energy levels in the dot is large enough that the weaker peaks associated with the coincidence of the energy level in the dot with the Fermi level in the source, can be seen at 1.3 K. The complete conductance diamond can be deduced and is shown for SALSA in Figure 8.2. The ΔE value obtained using Equation 8.5 is in good agreement with that derived by reversing source and drain.

The observation of the peak splittings under DC bias, and the internal consistency of the values deduced for peak energy separations, show unambiguously that Coulomb blockade dominates the conductance of these dots with large energy separations even at 1.3 K.

The final column in Table 1 is the ratio of energy level separation to gate period for the first two major conductance peaks at -0.52 and -0.43 V *G2* voltage. These values are similar for both samples and for all the other 150 nm quantum dots studied, as can be expected for dots of the same size near depletion.

A comparison of the data of Figure 8.1 with the lineshape expected for tunnelling through a single level shows that the observed lines are much wider than expected. This can be ascribed to a number of resonant levels lying under a particular peak. Lower temperature studies will be necessary to resolve this structure fully. The interesting feature of the substructure is that it varies with the voltages applied to the main gates *G1*, *G2* and *G4*. The most likely for this lies in the observation , deduced from our simulations, that the dot change shape when

the relative voltages on the gates are varied, becoming more or less elliptical. If the substructures are associated with excited states of the dot, then it is not surprising that their relative weights vary with the dot's shape.

The two 150 nm quantum dots presented here had particularly straightforward conductance peak structures with the largest energy level separations observed in surface gated quantum dots. In addition to the potential imposed by the gates, we expect for dots containing few electrons that the local potential fluctuations generated by remote ionised donors[8] will have a significant effect on the energy spectrum. Because the dots contain few electrons, these fluctuations will be unscreened and may in certain circumstances be of a similar magnitude to the potentials generated by the surface gates. We find that the exact energy spectra of these small dots depends critically on the local potential environment, and can change radically even during the course of a measurement in response to movement of trapped charge. These changes result in strikingly different transport characteristics in quantum dots with identical design and fabrication processes or even in the same quantum dot between different transport regimes what impedes full sample characterisation and sample reproducibility.

These quantum dots have been modelled self-consistently by solving numerically the three-dimensional Poisson equation and using the Thomas Fermi approximation for the density of the 2DEG in the channel. The calculations of the cut-off voltage and number of electrons in the dot are strongly dependent on the boundary condition on the free surface. The results for a frozen surface are in excellent agreement with experimental measurements of cut-off voltage and variation of numbers of electrons in a previous dot[5], see also Chapter 7. For quantum dot SALSA our calculated cut-off voltage is -0.55 V, some 10% higher than the value obtained in the experiment. This indicates that if there are additional electrons in the device beyond the first conductance peak, then there are very few. The calculations show that the shape of the dot is sensitive to the position of the centre gate; the confining potential is almost circular for this dot. Independent variation of the Fermi level inside the dot permits the total capacitance C and the Coulomb blockade energy e^2/C to be evaluated. For ten electrons in the dot the capacitance to the gates is around 15 aF, corresponding to an all gate period of 10 mV and e^2/C=2.8 meV. Both of these are in good

agreement with the values in Table 1, if one ignores the single electron contributions to the energy spacings.

8.4 Quantum Dots with Few Electrons in a Magnetic Field

A magnetic field has been extensively used to explore further the single electron transport properties of quantum dots mainly to map out the single-particle energy level spectrum of the dot as a function of the magnetic field. A great deal of experimental[10-12] and theoretical work[9,13,14] has been carried out on quantum dots in a magnetic field. Advancing nanostructure technologies have enabled experimentalists to achieve striking results in quantum dots in the few electron limit by the application of a magnetic field.[15-16] In this sub-chapter the magnetic field experimental data will be presented on transport spectroscopy in quantum dots in the few electron limit.

Semiconductor quantum dots containing few electrons can be regarded as artificial atoms. The charging energy needed to add an extra electron to the quantum dot is analogous to the electron affinity for a real atom. Filling up the dot with extra electrons is similar to that of placing an electron onto the atom's shell structure.[16] By applying a magnetic field perpendicular to the plane of the quantum dot, the filling of energy levels with electrons can easily be studied. The energy spectrum in a magnetic field can be easily solved analytically for a quantum dot with a two-dimensional radial confining potential[16] in the absence of electron-electron interactions. The energy E_{nl} of a state with a radial quantum number n (0, 1, 2, ..) and angular quantum number l (0, ±1, ±2, ..) in the absence of electron-electron interactions is given by Equation 8.6.

$$E_{nl} = \left[(2n+|l|+1)\hbar \left(\frac{\omega_c^2}{4} + \omega_0^2 \right)^{\frac{1}{2}} - \frac{l\hbar\omega_c}{2} \right] \tag{8.6}$$

Where $\hbar\omega_0$ is the electrostatic confinement energy and $\hbar\omega_c$ is the cyclotron energy. The values of E_{nl} are plotted for a typical value of $\hbar\omega_0$=3 meV, for a single electron picture, see Figure 8.3.

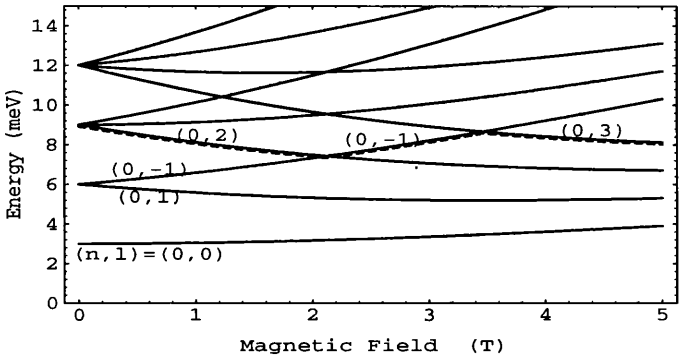

Figure 8.3: *Plot of E_{nl} versus the magnetic field for increasing electron number in the quantum dot at $\hbar\omega_0$=3 meV.*

The degeneracies at B=0.0 T are lifted in the presence of a magnetic field. A single particle state with a positive or negative angular momentum quantum number l shifts to lower or higher energy respectively as B is increased from 0 T. In Figure 8.3 the energy curve for the 7th and 8th electrons is marked with a dashed line to show that these electrons undergo transitions in their quantum numbers: (n,l) goes from (0,2) to (0,-1) at 1.3 T and then (0,3) at 2 T. As the magnetic field is increased the value of the energy level oscillates. The other electrons in the quantum dot follow the same pattern, and undergo similar energy level oscillations in varying magnetic field. The energy level oscillation for a given electron is reflected in oscillating conductance during single electron transport through the quantum dot. This energy level picture explains quite well the conductance oscillations in quantum dots in varying magnetic field[16].

8.5 Measurements

The two 150 nm quantum dots exhibited peculiar transport characteristics in a magnetic field in the few electron regime. In these experiments the magnetic field was kept constant while sweeping the voltage on the central gate *G2*. The tunnelling barriers on either side of the quantum dot were biased to achieve the pinch-off regime in which the quantum dots are close to depletion containing less than 6 electrons. All measurements were carried out at 1.3 K, which in some measurements could not provide the necessary resolution needed for more detailed analysis.

8.5.1 150 nm Quantum Dot Z212A in Magnetic Field

This 150 nm quantum dot was measured in constant magnetic field while the bias voltage on the centre gate was swept between 0 and -0.2 V. The Coulomb oscillations at 0 T at less negative gate voltages exhibit relatively sharp oscillations with big peak to valley ratio compared to the last oscillation at -0.135 V on the centre gate. At this gate voltage three superimposed peaks can be observed on the main, broad oscillation peak. The conductance of this quantum dot at more negative gate voltage approaches zero conductance without showing any additional Coulomb oscillation peaks and at around -0.18 V it reaches the noise floor. Repeating the same centre gate voltage sweep at 0.5 T the three superimposed conductance peaks become clearly visible at -0.115, -0.135 and -0.15 V. The position, height and period of the superimposed peaks also changes with the application of a changing perpendicular magnetic field, see Figure 8.4.

By further increasing the magnetic field to 1 Tesla the superimposed oscillation peaks become detectable on the second main oscillation peak at -0.075 V finger gate voltage. The main oscillation peak breaks up to three individual peaks with equal centre gate voltage period, see Figure 8.5.

The superimposed oscillation peaks exhibit oscillatory behaviour which is difficult to track. The interesting feature is that at certain magnetic field values the pronounced oscillation peaks tend to disappear and reappear. At high magnetic

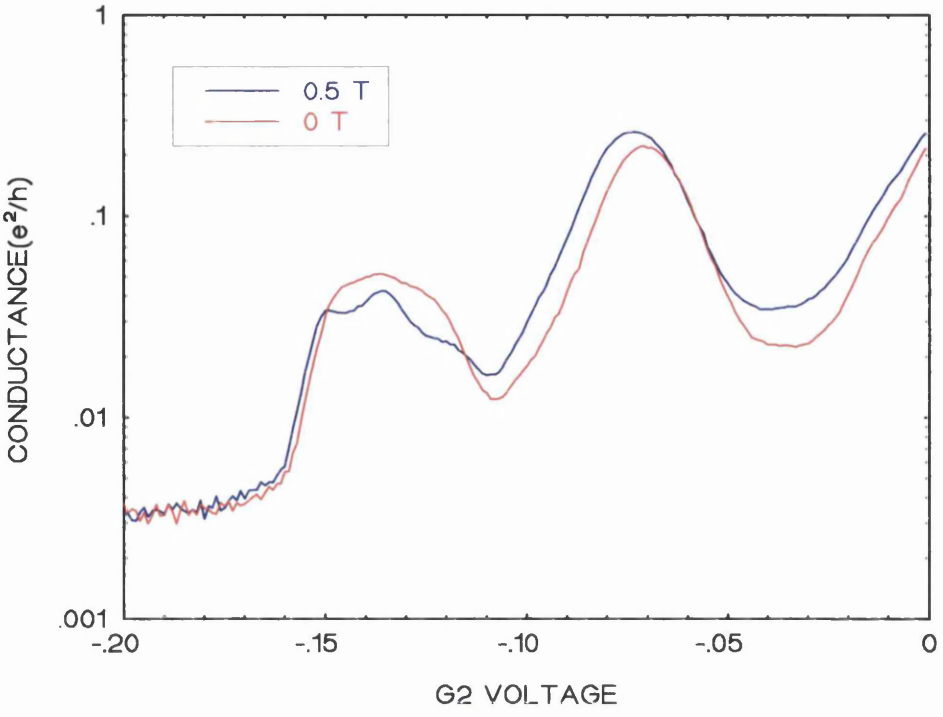

Figure 8.4: *Quantum dot Z212A in a magnetic field at 0 and 0.5 T.*

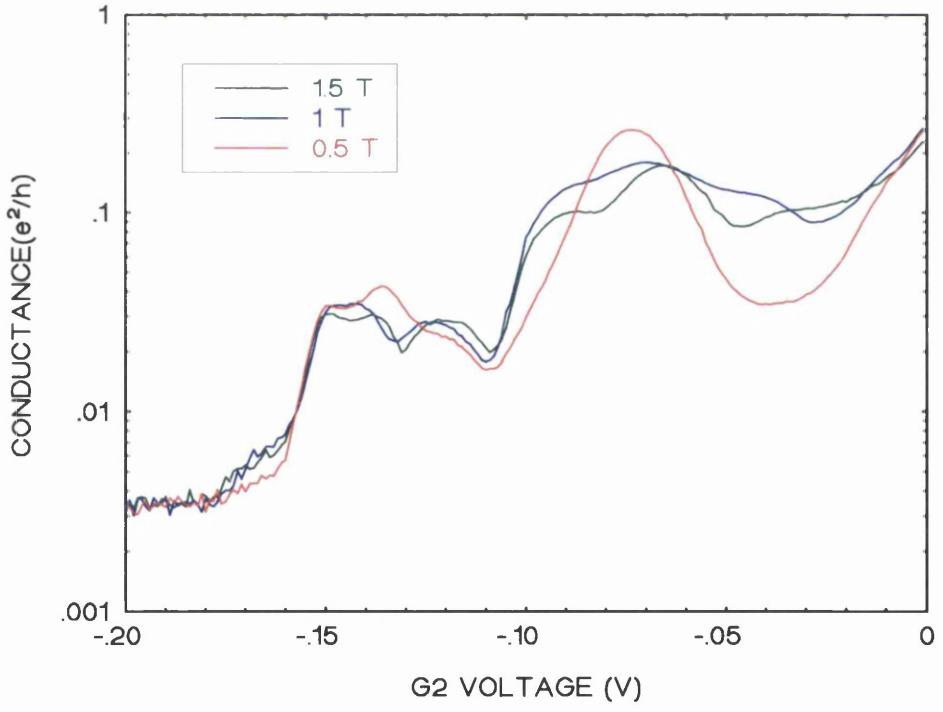

Figure 8.5: *150 nm quantum dot Z212A at 0.5, 1 and 1.5 T. The three superimposed oscillation peaks are clearly visible on both main oscillation peaks.*

field values between 2 and 3 T the second oscillation peak at around -0.75 V spreads out, the period of superimposed oscillations increases, while the period of the first oscillation peak at -0.14 V centre gate voltage decreases, see Figure 8.6. As the magnetic field is increased, the conductance through the quantum dot drops, indicating a less likely electron tunnelling event between the dot and the reservoirs. Due to the high measurement temperature of 1.3 K it was impossible to resolve further the main Coulomb oscillation peaks and the secondary superimposed oscillation peaks.

8.5.2 150 nm Quantum Dot SALSA in Magnetic Field

In general the oscillatory behaviour of this quantum dot is similar to that of quantum dot Z212A. This is mainly due to the similar quantum dot size of 150 nm, the most apparent difference being the different centre gate voltage range in which the two main Coulomb oscillation peaks appeared. In the whole centre gate voltage sweep range there were two main Coulomb oscillation peaks visible and the additional oscillation peaks were superimposed on them as the magnetic field was changing, see Figure 8.7.

Conductance through the quantum dot above -0.56 V on the centre gate drops close to zero conductance value. The superimposed oscillation peaks are already visible at 0 Tesla and getting more pronounced as the magnetic field is increased.

At higher magnetic fields above 1 Tesla the second main Coulomb oscillation peak at -0.4 V separates into two main oscillation peaks. This shows that by applying magnetic field to the sample the single electron transport characteristics under the influence of the magnetic field can become more resolved. At and above 1 Tesla all three oscillation peaks have similar peak to valley ratio and centre gate voltage period, see Figure 8.8.

In quantum dot SALSA the period of conductance oscillations become evenly spaced as the magnetic field is increased above 0.75 T. One possible hypothesis to explain our data is that the dot in zero magnetic field has an elliptical profile. The elliptical quantum dot can be compressed by the magnetic field to

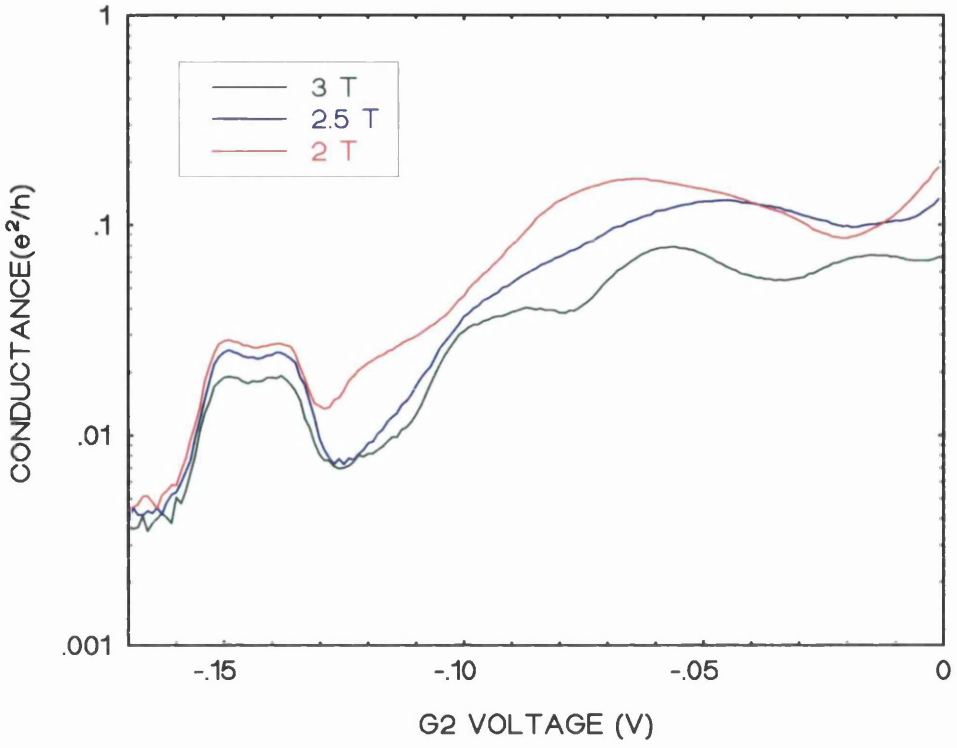

Figure 8.6: *Coulomb blockade oscillations in quantum dot Z212A, measured between 2 and 3 T.*

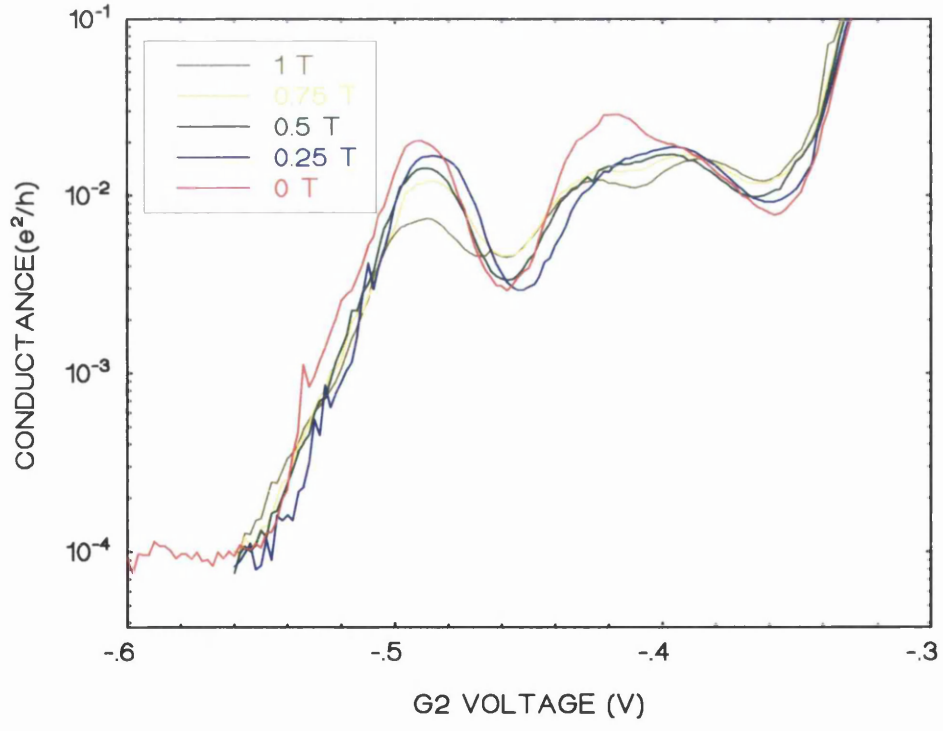

Figure 8.7: *Quantum dot SALSA in a magnetic field.*

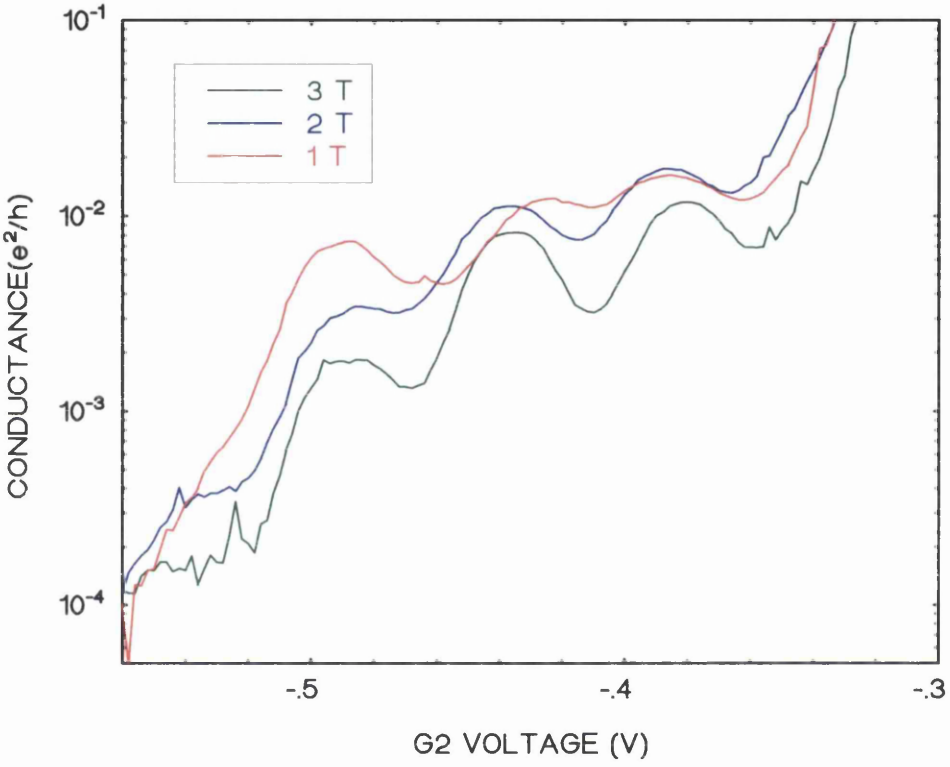

Figure 8.8: *Quantum dot SALSA in high magnetic fields. Note the separation of the superimposed conductance peaks into two main peaks.*

produce a much rounder dot with more evenly spaced energy levels.

Coulomb oscillations as a function of gate voltage in the quantum Hall effect regime were studied in surface gated quantum dots[18]. It was also found that the amplitude of oscillations was strongly enhanced compared to zero magnetic field but in that experiment the period of oscillations was not much affected. A possible explanation of these characteristics can be the virtual tunnelling process through the quantum dot which is strongly affected by high magnetic fields. Further experimental and theoretical work is needed to understand better the interesting effects of a magnetic field.

8.6 Conclusions

In this chapter we presented electron spectroscopy measurements on two 150 nm surface gated quantum dots which showed different electron transport characteristics compared to that of other 150 nm dots. One possible explanation is that these two dots were driven into a fully depleted regime when the surface gates could have a stronger effect on the shape of the confinement potential. In this case a slight change in the shape of the electron pool in the dot and charge configuration in the donor layer close to the dot result in stark change in the transport characteristics.

In small quantum dots there are two contributions to the energy spacings between the energy levels.[20] The Coulomb energy due to interactions with the surrounding electrodes controls large dots; very small quantum dots are dominated by the "single-particle" terms which depend on the size and shape of the quantum dot and the interaction between electrons within the dot. Most dots described in the literature are larger than the quantum dots described above, and the domination of the Coulomb contribution is expected. The conductance peaks, each resulting from the addition of a single electron, are then nearly equally spaced. The quantum dots we have described are small and optimised for maximum single-particle spacing. In our dots it is no longer clear that the Coulomb energies dominate.

Assume for simplicity that the dot is empty beyond the first visible peak. If Coulomb energies dominate, the first peak arises from the first electron, with substructure due to single-electron excited states. The second peak corresponds to the second electron entering the dot.

In contrast, if single-particle energies are dominant, the first peak involves two electrons of opposite spin entering the ground state, and its width reflects the Coulomb interactions. The gap between first and second peaks then reflects the energy spectrum of the dot. At present the experiment cannot distinguish unambiguously between these two limits. However, our semiclassical simulations suggest that that the Coulomb spacing between the levels for the first few electrons is greater than 2.8 meV for this size of dot, much larger than the width of the first peak. A rough estimate also shows that the single-particle energy levels should be about 1 meV apart. Thus the single-particle energies are not negligible, and may affect the position and shape of the observed peaks, but it is likely that Coulomb energies dominate even in these very small dots.

Recently published[21] quantum mechanical calculations on the energy spectra in small, few-electron quantum dots show how the change of the potential shape, the size and the shape of the quantum dots effect the energy level picture in quantum dots which can be applied to our quantum dots. However, further theoretical work is needed to investigate the effect of surrounding gates and bulk 2DEG. One should also note that all theoretical calculations refer to idealised circularly symmetric dots. In practice our dots are likely to have strong ellipticity which may profoundly affect their properties.

The electrons in the semiconductor material containing the shallow 2DEG in which the small quantum dots were fabricated are very close to the surface which greatly affects the reproducibility of quantum dots and in many cases makes the experimental results hard to interpret.

Clarification of the exact model to apply to dots of this size in the few electron limit is only likely when further spectroscopy studies with samples of different geometries are performed.

References

1. M. Kastner, Phys. Today **46**, No. 1, 24 (1993).

2. G. W. Bryant, Phys. Rev. Lett. **59**, 1140 (1987).

3. L Wang, J. K. Zhang, A. R. Bishop, Phys. Rev. Lett. **73**, 585 (1994).

4. H. Drexler, D Leonard, W Hansen, J P Kotthaus, P. M. Petroff, Phys. Rev. Lett. **73**, 2252 (1994).

5. Z Borsosfoldi, M Rahman, I A Larkin, A R Long, J H Davies,J M R Weaver, M C Holland, J G Williamson, Appl. Phys. Lett. **66**, 3666 (1995).

6. J M Kinaret *et al.,* Phys. Rev. B **46**, 4681 (1992).

7. J H Davies, I A Larkin, E V Sukorukhov, J Appl. Phys. **77**, 4504 (1995).

8. J A Nixon, J H Davies, H U Baranger, Phys. Rev. B **43** 12638 (1991).

9. D Pfannkuche, S E Ulloa, Phys. Rev. Lett. **74**, 1194 (1995).

10. P L McEuen, E B Foxman, U Meirav, M A Kastner, Yigal Meir, Ned S Wingreen, Phys. Rev. Lett. **66**, 1926 (1991).

11. P L McEuen, E B Foxman, Jari Kinaret, U Meirav, M A Kastner, Phys. Rev. B **45**, 11 419 (1992).

12. B W Alphenaar, A A M Staring, H van Houten M A A Mabesoone, O J A Buyk, C T Foxon, Phys. Rev. B **46**, 7236 (1992).

13. M Wagner, U Merkt, A V Chaplik, Phys. Rev. B **45,** 1951 (1992).

14. V Halonen, Solid State Communications Vol. **92**, 703 (1994).

15. N C van der Vaart, M P de Ruyter van Stevininck, L P Kouwenhoven, A T Johnson, Y V Nazarov, C J P M Harmans, Phys. Rev. Lett. **73**, 320 (1994).

16. S Tarucha, D G Austing, T Honda, R J van der Hage, L P Kouwenhoven, submitted to Phys. Rev Lett.

17. J G Williamson, A A M Staring, H van Houten, L P Kouwenhoven, C T Foxon, to be published.

18. E B Foxman et al, Phys. Rev. B **47** 10020 (1993).

19. N S Bakhalov et al, Sov. Phys. JETP, **68** 581 (1989).

20. Z Borsosfoldi, I A Larkin, A R Long, M Rahman, M C Holland, J M R Weaver, J H Davies, J G Williamson, Surf. Sci, **361/362**, 677 (1996).

21. J L Zhou, J Wu, R T Fu, H Chen, Y Kawazoe, Phys. Rev. B **55** 1673 (1997).

Chapter 9

Conclusions

9.1 Introduction

The main conclusions reached from the experimental data and theoretical calculations presented in this thesis are summarised in this chapter. Several quantum dots with different designs and physical parameters were fabricated on various shallow 2DEG heterostructures. All layers used to fabricate the gated quantum dots were of high quality: for surface gated quantum dots to be fully controllable all gates must function. In general the surface gated quantum dots were fabricated using the minimum number of gates to increase the probability of producing a functioning device.

9.2 Surface Gated Quantum Dots at and above 1.2 K

The main aim of this work was to fabricate and test surface gated quantum dots on shallow 2DEG material which would work in a high temperature regime (at and above 1.2 K). Quantum dots, working at and above this temperature at the beginning of our research would have been the significant first step towards quantum dots functioning at 77 K and at room temperature in the not too distant future. Our experiments showed that the necessary resolution (for all measurements apart from the transport spectroscopy) was achieved by studying the dots at and above 1.2 K. This meant that experiments could be carried out

cheaper and faster using the variable temperature insert than the dilution fridge, thus cutting down on cooling down time and saving helium.

In this work quantum dots with various surface gate patterns were fabricated on shallow 2DEG GaAs-AlGaAs material where the 2DEG was 28 nm below the surface of the heterostructure. The first quantum dot exhibiting weak Coulomb blockade oscillations was quantum dot Z19A. This quantum dot had a surface gate pattern which was not optimised for the depth of the 2DEG. The point contacts were too wide and the plunger gate emerged too far into the dot, which was liable to lead to breakup into separate electron pools and make the dot uncontrollable. The next generation of quantum dots had the theoretical and experimentally proved optimal 100 nm wide point contacts and a "smooth" gate pattern with which we were able to form a roughly circular quantum dot. With this design we could study the effect of the shape and physical size of the electron pool on quantum dot characteristics. We also fabricated single, double and quadruple quantum dots on the same sample to compare these configurations. The dots were made with a double gate structure which did not allowed us the necessary control over these devices. In general we measured several identical quantum dots from each batch and they showed similar main features, with differences probably due to surface effects, electrostatic variations in the dot's surroundings and sample non-uniformity. A batch of "semi back-gated" quantum dots has also been fabricated where the sample holder's base has been used to back-gate the quantum dots. The poor electrical contact and the large distance (some 400 μm) between the surface of the semiconductor and the sample holder's plane made the quantum dot's electrical excitation with a back gate extremely difficult and did not result in a discovery of any new electron transport effects.

In general the full characterisation of the measured surface gated quantum dots had been impeded by reduced device longevity as a result of gate breakages, and changes on the surface of the semiconductor critically affecting the dot's environment. The damage caused by electrostatic discharge effects was the main problem during sample handling and mounting. The gates of several well performing quantum dots were damaged by applied gate bias differences between two neighbouring gates.

Theoretical calculations showed that for a 28 nm electron depth, to achieve the maximum single particle energy level separation in the dot to ensure the operation of the quantum dot at the highest possible temperature, a quantum dot with a 150 nm nominal diameter was optimal. Measurements conducted on quantum dots with a diameter in a range between 100 and 350 nm confirmed the results of the theoretical calculations.

Two 150 nm quantum dots exhibited Coulomb blockade oscillations above 7.7 K. Other two 150 nm quantum dots measured in the course of this project have shown some unexpected features. On these 150 nm quantum dots we had done spectroscopy measurements in the few electron regime which exhibited interesting characteristics in DC source-drain bias measurements and in a magnetic field. We have shown in our experiments the effect of the shape of the electron pool on the quantum dot's characteristics containing only a few electrons. We have analysed and modelled these effects but further experimental and analytical work is needed to establish the more exact dependence of the quantum dot's behaviour on its physical parameters.

During the course of this project we showed that shallow 2DEG heterostructures can successfully be used for fabricating small quantum dots containing very few electrons which work in the high temperature regime, but these quantum devices have a short lifetime due to surface effects and sudden changes in the electrostatical surrounding of the dot. These characteristics of the shallow 2DEG materials in their present form make them inadequate for producing reliable nanoscale devices working at high temperatures.

Appendix

Developments in the field since the work described in this thesis was completed

Introduction

Since the experiments contained in this thesis were finished in summer 1995, a great deal of experimental and theoretical work has been carried out on surface gated quantum dots. In this appendix we summarise the new results and directions of research on quantum dots. We concentrate on results from the period 1995-1998 which are closely related to the work in this thesis.

Design and optimisation of large quantum dots

Earlier works[1,2] from this period concentrated on conductance oscillations in large surface gated quantum dots containing above 1000 electrons. The amplitude of oscillations was optimised as a function of the quantum dot size with varying gate voltage and also by applying moderate magnetic fields. The behaviour of double and triple quantum dots was analysed[3,4] in the absence of a magnetic field, concentrating on the dependence of the Coulomb blockade oscillation on the size of the dot. Research work was also concentrated[5] on developing optimised self-assembled quantum dots working at higher temperatures (up to 6 K) using epitaxial growth techniques. In an interesting study[6] the effect of the barrier thickness asymmetries on electron transport in quantum dots is discussed, with special emphasis on occupation probability of single energy levels as a function of barrier thickness asymmetry. A study on a

quantum dot[7] fabricated by focused laser beam-induced doping shows the effect of reduced dimensions in the form of large single particle energy level separation at relatively high temperature.

Quantum dots operating at high temperatures

A huge amount of work has been concentrated on increasing the operating temperature regime of quantum dots fabricated both on GaAs-AlGaAs heterostructures and on silicon. The goal for this work has been the fabrication of single-electron transistor circuits working at room-temperature.

An important study[8] on single-electron transistor aiming at higher operating temperature (above 4.2 K) was carried out using silicon technology and an ingenious gate structure. Research work was then concentrated on similar material structures using well developed fabrication processes. With the rapid development of submicron electron-beam lithography, these structures yielded single electron transistors working at room temperature[9-12]. The common feature of these devices was that the active device size was around 10 nm and fabricated from nanocrystalline silicon. The next step was the development of single electron logic and memory circuits[13-15] which opened up the road for potential applications. At the beginning these studies concentrated on simulating the single-electron transistor based circuit performance and raising the temperature of operation. Later work[15] demonstrated a silicon single-electron memory operating at room temperature. An interesting study[16] was carried out on a multiple-junction single-electron transistor with varying number of electrons inside the transistor. More research effort was concentrated on the fabrication and characterisation of room temperature silicon single electron memory[17] to open up a possibility of a mass application for these devices. The crucial issue of the necessity of generating voltage gain in SET based devices was tackled in another experiment[18] which set the possibility for fabricating a variety of SET based circuits[19]. The single-electron transistor fabricated and measured in this study featured a 12 nm nominal dot size and a 110 meV energy level separation which ensures the high operating temperature of this device.

Transport spectroscopy measurements

A large body of research work has been concentrated on electron transport spectroscopy measurements which can be used to analyse the energy structure of quantum dots and particularly to study the effect of electron-electron interactions in quantum dots.

A fundamental theory of electron spectroscopy was presented in a paper[20] which gave a detailed study on a strongly asymmetric quantum dot probed by single-electron spectroscopy. Theoretical calculations of the few-electron ground state energies are in very good agreement with the experimental data. In a theoretical work[21] the energy levels inside the quantum dot containing one or two electrons was described. The calculations in this work on the dependence of the Coulomb energy on the finite width of the quantum dot agree well with experimental results.

In a more recent study[22] theoretical calculations were concentrated on the effects of scattering centres on the energy spectrum of a quantum dot in the presence of a magnetic field. The single particle energy levels in a quantum dot are calculated for different distances of the scattering centres from the centre of the dot. This work shows the sensitivity of small quantum dots containing very few electrons to the electrostatical environment of the dot. In another paper[23] the spectra of electron and donor states in quantum dots with different confinement potentials were calculated. The effects of the potential shapes and donor positions were studied in detail.

A theoretical study[24] predicted the Kondo-effect in a single-electron transistor when the number of electrons in the SET is odd. By tuning the parameters of a SET, the authors were able to demonstrate the predicted effect on the Kondo temperature and the occupancy of the localised site in the SET.

An interesting experimental electron spectroscopy[25] was carried out on a quantum dot molecule comprising two coupled vertical quantum dots with a triple barrier structure. Although the physical size of the quantum molecule was 250 nm, this can be reduced by applied bias to 75 nm making the quantum molecule particularly suitable for electron-spectroscopy measurements. The

authors compare the above double dot molecule with an effective, ionised artificial hydrogen molecule which can be detuned by the applied bias voltage.

A theoretical and experimental study[26] of electronic structures in quantum dots with different physical shapes containing one or a few electrons was carried out by Ezaki *et al.* This work shows that the addition energy of an electron in a quantum dot with few electrons reveals the existence of a clear shell structure.

A recent experimental study[27] on small quantum dots containing very few electrons showed results very similar to ours, obtained in electron-spectroscopy measurements. Coulomb oscillations exhibited irregular behaviour in period, reflecting a shell structure as the number of electrons in the dot approaches zero. The authors observed kink structures in the Coulomb oscillation peak period versus magnetic field which can be explained with the transition in spin and angular momentum states.

Electron-spectroscopy measurements in a magnetic field

Magnetic field has been used extensively in numerous electron-spectroscopy studies to fully explore the fine single particle energy level structure in quantum dots containing only a few electrons. In an interesting paper[28] the magnetic field is used to reveal significant differences between the theoretical calculations and measurements both for smaller ($n<5$) and larger ($n>35$) quantum dots. The authors show a significant increase of the amplitude of Coulomb blockade oscillations for quantum dots containing more than 30 electrons with the application of a magnetic field.

In another study[29] the effect of gates on the electron-electron interaction in the quantum dot in an applied magnetic field was studied. The authors describe the screening effect of the charges induced on the gate electrodes
on the physical properties of the dot. It is shown that, as a result of the screening, the transitions of the total angular momentum and spin of the ground state are shifted to higher magnetic fields.

Thorough electron-spectroscopy measurements were performed on a ground and excited states of a single quantum dot[30] by studying the linear and nonlinear transport. Electron-spectroscopy measurements in a double quantum dot

system consisting of two quantum dots of different sizes were also performed These measurements showed the effect of the charging energies of the individual dots and coupling between them on the conductance of the system.

A recent study[31] shows a good agreement with the experiments on quantum dots in an arbitrarily oriented magnetic field. This work shows shell effects and hence shape changes of quantum dots in a magnetic field. This work is complemented[32] by exact calculations of the energy level ordering of a quantum dot containing just two electrons for a magnetic field of arbitrary strength.

A theoretical study[33] used a current-density-functional approach to analyse a quantum dot with a disk shape containing some 200 electrons. The ground state of this quantum dot exhibited strong electron-electron interaction effects as a function of both a weak and strong magnetic field.

In the above subsections we presented the latest results of the research work which have been carried out on quantum dots. The above appendix far from complete, it comprises only the most important works on quantum dots and single electron transistors. Considering the pace of technological improvement and the increase of computational power some significant developments are expected in the coming years in the field of quantum dots.

References

1. M Persson, P E Lindelof, B von Sydow, J Petterson, A Kristensen, J of Phys. **7**, No.19, 3733 (1995).

2. D G Austing, T Honda, S Tarucha, Solid-State Electronics **40**, 237 (1996).

3. F R Waugh, M J Berry, D J Mar, R M Westervelt, K L Campman, A C Gossard, Phys. Rev. Lett. **75**, 705 (1995).

4. C Livermore, C H Crouch, R M Westervelt, K L Campman, A C Gossard, Superlattices and Microstructures **20**, 633 (1996).

5. M Dilger, R J Haug, K Eberl, K von Klitzing, Sem. Sci. and Tech. **11**, 1493 (1996).

6. T Schmidt, R J Haug, K von Klitzing, A Forster, H Luth, Phys. Rev. B **55**, 2230 (1997).

7. P Baumgartner, W Wegscheider, M Bichler, G Schedelbeck, R Neumann, G Abstreiter, Appl. Phys. Lett. **70**, 2135 (1997).

8. H Matsuoka, S Kimura, Appl. Phys. Lett. 66, 613 (1995).

9. K Matsumoto, Physica B **227**, 92 (1996).

10. K Kurihara, H Namatsu, M Nagase, T Makino, Mic. Eng. **35**, 261 (1997).

11. L J Guo, E Leobandung, S Y Chou, Appl. Phys. Lett. **70**, 850 (1997).

12. M Otobe, H Yajima, S Oda, Appl. Phys. Lett. **72**, 1089 (1998).

13. R H Chen, A N Korolkov, K K Likharev, Appl. Phys. Lett. 68, 1954 (1996).

14. E S Soldatov, V V Khanin, A S Trifonov, D E Presnov, S A Yakovenko, G B Khomutov, C P Gubin, V V Kolesov, JETP Lett. **64**, 556 (1996).

15. A Nakajima, T Futatsugi, K Kosemura, T Fukano, N Yokoyama. Appl. Phys. Lett. **70**, 1742 (1997).

16. R H Chen, K K Likharev, Appl. Phys. Lett. **72**, 61 (1998).

17. L J Guo, E Leobandung, L Zhuang, S Y Chou, J. of Vac. Sci. and Techn. B 15, 2840 (1997).

18. R A Smith, H Ahmed, Appl. Phys. Lett. **71**, 3838 (1997).

19. L Zhuang, L J Guo, S Y Chou, Appl. Phys. Lett. **72**, 1205 (1998).

20. T Schmidt, M Tewordt, R H Blick, R J Haug, D Pfannkuche, K von Klitzing, A Forster, H Luth, Phys. Rev. B **51**, 5570 (1995).

21. F M Peeters, V A Schweigert, Phys. Rev. B **53**, 1468 (1996).

22. V Halonen, P Hyvonen, P Pietilainen, T Chakraborty, Phys. Rev. B **53**, 6971 (1996).

23. J L Zhu, J Wu, R T Fu, H Chen, Y Kawazoe, Phys. Rev. B 55, 1673 (1997).

24. D Goldhaber-Gordon, H Shtrikman, D Mahalu, D Abusch-Magder, U Meirav, M A Kastner, Nature 391, 156 (1998).

25. T Schmidt, R J Haug, K von Klitzing, A Forster, H Luth, Phys. Rev. Lett. **78**, 1544 (1997).

26. T Ezaki, N Mori, C Hamaguchi, Phys. Rev. B **56**, 6428 (1997).

27. Y Tokura, L P Kouwenhoven, D G Austing, S Tarucha, Physica B 246, 83 (1998).

28. T Schmidt, M Tewordt, R H Blick, R J Haug, D Pfannkuche, K von Klitzing, A Forster, H Luth, Phys. Rev. B **51**, 5570 (1995).

29. L D Hallam, J Weis, P A Maksym, Phys. Rev. B **53**, 1452 (1996).

30. R J Haug, J Weis, R H Blick, K von Klitzing, K Eberl, K Ploog, Nanotechnology **7**, 381 (1996).

31. W D Heiss, R G Nazmitdinov, Phys. Rev. B **55**, 16310 (1997).

32. M ElSaid, Superlattices and microstructures **23**, 1237 (1998).

33. M Pi, M Barranco, A Emperador, E Lipparini, L Serra, Phys. Rev. B **57**, 14783 (1998).